United States
Consumer Product Safety Commission

May 29, 2024

CPSC[1] Staff Statement on: Exposure Assessment of Carbon Nanotubes (CNTs) in CNT Enhanced Fibers and Textiles in Children's Products

1. Background

The 2015 report titled, "Exposure Assessment of Carbon Nanotubes (CNTs) in CNT Enhanced Fibers and Textiles in Children's Products" describes studies performed by the National Institute of Standards and Technology (NIST). The study was supported by interagency agreement CPSC-I-13-0015 between the Consumer Product Safety Commission (CPSC) and NIST.

NIST, as a research group under the US Department of Commerce, conducts measurement science research, provides technical expertise to the development of standards, and performs fundamental and applied research to assure the quality of measurement results.

2. Introduction

Carbon nanotubes (CNT) are used in some children's products (e.g., school backpacks) that are marketed as offering personal protection from small firearms. Nanoparticles, including CNTs, could pose health risks to consumer product users, especially via inhalational exposure, if released from products.

Nanoparticles are of concern because their nanoscale size enables the particles to penetrate into the lung deeply when inhaled, to potentially move across lung cell walls, and to become systemically distributed in the body. Published literature from *in vivo* animal studies has shown that CNTs and carbon nanofibers (CNFs) can cause persistent pulmonary inflammation, granulomatosis, and fibrosis. In addition, immunosuppression, neuroinflammation, and cardiovascular effects, such as endothelial dysfunction, may occur from systemic inflammation in laboratory animals following inhalation exposure to CNTs. While these health effects have been observed in animal studies, epidemiological studies in CNT/CNF workplaces have not shown consistent patterns in the health effects assessed.

As the use of nanomaterials in consumer products continues to rise, it is important to develop reliable sampling and analytical methods to collect information regarding the release of nanoparticles that can be used to assess potential exposure and possible health risks. Multiple CNTs constitute multi-walled carbon nanotubes (MWCNTs) in a concentric cylinder form. MWCNTs

[1] This statement was prepared by the CPSC staff, and the attached report was prepared by NIST for CPSC staff. The statement and reports have not been reviewed or approved by, and do not necessarily represent the views of, the Commission.

are used in some textile applications, such as children's anti-ballistic backpacks, as well as in some sports equipment[2].

3. Objectives

NIST, the US Army Engineer Research and Development Center (ERDC) of the Department of Army, and CPSC collaboratively developed a comprehensive testing plan to detect and quantify nanoparticles released from ballistic school backpacks. The purpose of the attached 2015 NIST study was to develop methods for detecting MWCNTs in a textile panel used for the ballistic backpacks and ballistic inserts used in ordinary backpacks and to assess MWCNT release from these products during mechanical wear conditions. Work performed by ERDC evaluated the potential release of MWCNTs from a ballistic panel and ballistic inserts used in school backpacks, due to environmental aging (e.g., UV exposure, heat), handling (e.g., washing) or from liquid exposures (e.g., simulated beverages)[3].

4. Experimental Design and Methods

The study focused on a ballistic panel, which is used for making a commercially available ballistic backpack, and two types of ballistic inserts, which can be separately purchased and inserted into ordinary backpacks. The three products contain MWCNTs intended to promote anti-ballistic function. For this cover sheet, the ballistic panel is referred to as Sample 1, and the two ballistic inserts are referred to as Sample 2 and Sample 3. Chemical analyses of MWCNTs from the product samples were carried out using Raman spectroscopy, optical microscopy, scanning electron microscopy (SEM), and transmission electron microscopy (TEM).

Among several product use scenarios, NIST determined that the MWCNT particles possibly can be released during direct mechanical stressing of the samples if the outer cases of backpacks are compromised due to prolonged use, accidental tear, or misuse of the products. Because the materials (i.e., ballistic panel and inserts) containing MWCNT particles were encased in a sealed water-resistant casing, the release of MWCNTs is not likely unless the outer casings are compromised accidentally or through misuse by strong mechanical stressing. Therefore, the 2015 NIST research focused on developing analytical methods to detect and analyze release of nanoparticles using direct mechanical abrasion as the worst-case scenario.

For direct mechanical stress evaluation, NIST conducted both a wipe test and an abrasion test using a Taber Linear Abraser Model 5750 abrader with T-slot universal table.

For the wipe testing, a crockmeter tip was attached to the Taber abrader. The attachment performs a repeated rubbing motion over a test sample using a weighted tip covered with a ‘crocking’ cloth that is designed to collect released material. Particles from the wipe cloths were collected using either 12 mm aluminum stub or 25 mm silicon (Si) wafers. Particle samples from the 12 mm aluminum stub and the 25 mm Si wafers are referred to as SEM stub samples and Si wafer dust

[2] NIST 2012 and 2015 CNT Baseball Bat Studies and Staff Statement (October 20, 2023) https://cpsc.gov/content/NIST-2012-and-2015-CNT-Baseball-Bat-Studies-and-Staff-Statement
[3] ERDC 2016 Studies on Carbon Nanotubes used in Ballistic Backpacks and CPSC Staff Statement (November 23, 2023) https://cpsc.gov/content/CPSC-Nanotechnology-Program-Project-Report-Backpacks

samples, respectively. Automated SEM imaging and particle analysis were used to investigate large regions on individual SEM stub and Si wafer samples.

For the abrasion testing, NIST used the Taber abrader and a micro-orifice uniform deposit impactor (MOUDI) to collect particles according to sizes stored in different stages of the MOUDI. This method was used to mitigate the low sampling efficiency problem due to transport loss of the particles during the sampling.

5. Results

Raman spectroscopy identified the presence of MWCNTs in the structures of all three samples.

SEM images were taken on Focus Ion Beam (FIB) prepared cross sections of the samples. The structure of Sample 1 is fully dense, but those of Samples 2 and 3 are not as dense as Sample 1. SEM imaging also identified that the MWCNT sheets used in the samples can be readily delaminated by external force (e.g., incidental folds) to expose their interior.

Similar to SEM, TEM analysis identified a dense structure, containing MWCNTs dispersed throughout the material of Sample 1, indicating a relatively high concentration of MWCNTs. The TEM analysis also presented dark round regions and white holes during initial imaging and energy dispersive x-ray spectrometry (EDS) analysis, respectively, that indicate carbon contamination of samples. Compared to Sample 1, Samples 2 and 3 contained less matrix material embedded with MWCNTs.

ASTM method D4157-10, Standard Test Method for Abrasion Resistance of Textile Fabrics, was adopted for the Taber wipe test to evaluate the integrity of the outer casing material of Sample 1. The integrity of the casing appeared to be unaffected by the ASTM test, indicating that the outer nylon casing is unlikely to wear out during the normal use of the product. Because the materials (i.e., ballistic panel and inserts) containing MWCNT particles were encased in this sealed water-resistant casing, the release of MWCNTs is not likely unless the outer casings are compromised accidentally or through misuse by strong mechanical stressing. Therefore, the wipe and abrasion tests were conducted on the MWCNT containing layers of the ballistic panel and inserts.

SEM analysis of Sample 1 from the wipe test revealed that numerous micrometer-sized and nanometer-sized particles were found in the survey scan (aka low-resolution) and the high-resolution images. Compared to Sample 1, there were many large fibrous particles from SEM stub samples of Sample 2. A closer examination of the wipe test samples from Samples 2 and 3 reported the presence of many nanoscale fibers and presented a similar particle morphology. However, by a comparative analysis between the control sample and test samples, most nanoscale fibers detected on the SEM stub samples were probably from the wipe cloths used for particle collection.

According to automated SEM imaging analysis on the Si wafer dust samples, most particles from the wipe test samples were less than 700 nm in diameter. Automated high-resolution image analysis revealed that most particles appear to be agglomerated particles which do not contain MWCNTs. However, from manual high-resolution scanning, several MWCNT-like particles and MWCNT particles agglomerate with small polymer flakes were observed in Sample 3.

Previous NIST studies have shown that sampling efficiency of particles can be a challenging problem for abrasion experiments. It has not been clear whether the poor sampling efficiency is due

to the lack of aerosols generated or the loss of particles that occurred through various mechanisms (e.g., electrostatic or transport loss) during the abrasion process. NIST used a micro-orifice uniform deposit impactor (MOUDI) to collect size selected samples at high flow rates to mitigate the low sampling efficiency problem due to transport loss. MOUDI particle size distribution testing did not exhibit an expected pattern; instead of one major peak, there was a bimodal distribution. This pattern also differed from the passive collection sample. Most particles found in the MOUDI were a few hundred nanometers or less in diameter. Sample 1 presented round shaped particles that did not appear to be single or agglomerated MWCNTs. Samples 2 and 3 generated fractal-like particles to which nano-sized particles were agglomerated to form chain or sponge-like particles. Numerous protruding nanofibers attached to large particles were also found. Compared to the MOUDI sampling, passive sampling of Sample 2 contained numerous agglomerates, as well as fractal- and rod-like particles. Rod-like particles appeared to be MWCNTs. SEM-STEM and TEM analyses revealed there were many fractal-like agglomerates that formed long chains. High magnification TEM images revealed layered MWCNT-like structures throughout the particles.

6. Summary

This NIST study confirms the presence of MWCNTs in all three evaluated product samples.

From the wipe testing on SEM stub samples, the detection of MWCNTs was not successful from the ballistic materials used for backpacks due to a confounding factor (e.g., contaminants) and a technical challenge (e.g., imaging artifacts). The same contamination problem caused challenges in the image analysis of particles from the Si wafer dust samples. The particle size distribution from the automated images and data analysis presented a similar trend for the three samples. However, it was theoretically expected that a different pattern would be generated in the particle size distribution among the samples because there was a significant difference in MWCNT incorporation methods between Sample 1 and Samples 2 and 3. The fact that this structural difference did not cause the samples to produce a different pattern in particle size distribution can lead to an interpretation that the true distribution was disturbed by confounding factors and/or technical challenges in imaging analysis.

Similarly, the abrasion testing did not generate the expected particle size distribution. The MOUDI system did not collect particle samples as it was designed. NIST indicated that further examination is needed to better understand the MOUDI sampling process of particles. NIST reported that neither isolated nor agglomerated MWCNTs were identified from Sample 1 after abrasion. From the image analyses of Samples 2 and 3, NIST found many micrometer-sized particles that contain protruding MWCNT-like nanoscale fibers, individual MWCNTs, and MWCNT agglomerates. Because the automated imaging was not effective for particle analysis, most MWCNT particles were identified by a manual search. Carbon contamination of the specimen surface, which is a common SEM imaging artifact, can be a significant confounding factor for the imaging of a nano-scale features.

NIST found that fully embedded MWCNTs in a flexible matrix, as seen in Sample 1, are less likely to be released as individual or agglomerated MWCNTs, when compared to the coated MWCNT bundles seen in Samples 2 and 3. NIST stated that the 2015 imaging technology can generate high resolution images to confirm the presence of MWCNTs, but the imaging analyses over a large sample area in a quantitative manner is a technical challenge. NIST indicated that the 2015 study

approach requires significant manual intervention by analysts although they have made progress in experimental design for particle sampling process and automated imaging analyses.

Exposure Assessment of Carbon Nanotubes (CNTs) in CNT Enhanced Fibers and Textiles in Children's Products

Report to the U.S. Consumer Product Safety Commission Interagency Agreement # CPSC-I-13-0015

Final Report Date: August 17, 2015

Performed by:
Keana Scott
Frederick Meisenkothen

Submitted by:
Keana Scott
Microanalysis Research Group
National Institute of Standards and Technology 100
Bureau Drive, MS-8372
Gaithersburg, MD 20877
(301) 975-4579
keana.scott@nist.gov

Disclaimer: Certain commercial equipment, instruments, or materials are identified in this talk to foster understanding. Such identification does not imply recommendation or endorsement by NIST, nor does it imply that the materials or equipment identified are necessarily the best available for the purpose.

1 Table of Contents

2 EXECUTIVE SUMMARY

Three commercially available, multi-walled carbon nanotube (MWCNT) containing ballistic inserts were used as test systems for developing analytical methods for detecting MWCNTs in consumer products. In addition, methods were developed for detecting, characterizing, and quantifying particles released from these products during mechanical wear simulations. All three types of inserts had a similar construction, in which a stack of ballistic textile sheets (including one or more MWCNT reinforced sheets) were encased in sealed water resistant outer sleeve. However, the manufacturers employed two different strategies for incorporating MWCNTs into the ballistic insert materials. One company chose to use a MWCNT impregnated coating on the constituent woven [redacted] sheets. The other two insert products each contained a single matted sheet of coated MWCNT bundles.

The outer sleeve materials did not show evidence of significant wear after being subjected to repeated rubbing tests, indicating that the outer sleeve may provide the consumer with adequate protection against direct exposure to the MWCNT reinforced sheets under normal use. However, if the outer sleeves are compromised through an accident or misuse, the MWCNT reinforced sheets in the ballistic inserts could become exposed and thus prone to direct mechanical wear. Wipe tests and abrasion tests were performed on the MWCNT reinforced sheets from the ballistic panels to simulate an accident/misuse scenario. The results from the wipe tests indicated that the MWCNT impregnated coating on the [redacted] released fewer particles than the matted MWCNT sheets. Of the particles collected and imaged from the MWCNT coating, none were bare MWCNTs or agglomerates of MWCNTs. However, when same wipe test was performed on the MWCNT sheet materials a small number of individual MWCNTs and MWCNT agglomerates were found. The abrasion test results showed similar results. No release particles from the MWCNT impregnated coating on [redacted] were identified as bare MWCNTs or agglomerates of MWCNTs. However, bare MWCNTs and nanoscale MWCNT agglomerates, as well as a number of large (several micrometers in diameter) particles with many MWCNT-like nanofibers protruding from them, were identified in the release particle samples from the MWCNT sheets.

Cascade-impactor-based particle sampling was used to size separate release particles and to mitigate analysis problems that often arise from having highly polydisperse samples. However, the MWCNT reinforced sheets produced relatively few release particles and the particles were much smaller on average compared to those produced from solid nanocomposites, such as epoxy MWCNT composites. We found that the passive sampling of the release particles was more effective than impactor sampling. The particle size distribution results from different impactor stages were inconsistent and did not effectively size separate the release particles.
We suspect that there was a significant loss of particles during transport (including the inlet efficiency) and so the resulting sampling efficiency of the impactor was quite poor.

The use of automated imaging and image analysis procedures enabled us to survey large areas of the samples that contained the release particles in a consistent and reproducible manner. However, this method was not effective in providing a quantitative measure of the MWCNT release rate from the product samples, or in determining the overall release particle size distributions. These shortcomings were mainly due to the inherent subjectivity in some of the image analysis operations and also due to the limitations in current automated imaging technology. Although the current instrument technology can image individual MWCNTs with relative ease, performing this type of task in an automated manner requires robust and sophisticated adjustment routines capable of correcting the imaging conditions on the fly. While technically possible, a thorough analysis of sufficiently large sample areas, at an image resolution necessary to reliably detect individual MWCNTs, would require an enormous investment in both instrument time and manual data reviewing effort. Such an effort is not practical.

We found that the method used to incorporate the MWCNTs into the ballistic material dictates the rate of release from the product. The fully embedded MWCNTs present in the flexible coating that was applied to the woven [redacted] are less likely to be released, as either bare MWCNTs or as nanoscale agglomerates of MWCNTs, than the MWCNTs contained within the open structure of the matted MWCNT sheet materials. We have made some progress in designing a robust wear particle sampling process and automated imaging pipeline. However, we believe aerosol sampling of the wear particles, especially at the scale of 10 nm to 20 nm MWCNTs, require additional aerosol conditioning steps and better understanding of the fluid dynamics within the sampling chamber. Imaging technology to analyze the release particles does exist, but the current approach requires significant manual intervention, thereby making the consistent analysis of statistically relevant amounts data impractical. The accurate quantitative assessment of MWCNT release rates from commercial ballistic products will require the following developments: an improved aerosol sampling system, an interactive and rule-driven automation technology, and a better understanding of the nanoscale aerosol transport behavior through novel visualization methods that can probe MWCNT release dynamics.

3 INTRODUCTION

Nanomaterials are defined as purposefully produced materials that range in size from 1 nm to 100 nm in at least one dimension [1]. Although the constituent components in nanomaterials are often commonly used materials, these materials may demonstrate different physical and chemical properties when reduced to the nano-scale in size. Until recently, the technologies required for the industrial scale production of engineered nanomaterials did not exist, and the ways in which engineered nanomaterials interact with the environment and within the human

body had not been the subject of much research. Therefore, the potential health effects that may be associated with exposure to different quantities and types of nanomaterials are largely unknown. As the use of performance enhancing engineered nanomaterials in consumer products continues to rise, it is crucial to gather information on the types of nanoparticles that can be shed from these products as a result of use, foreseeable misuse, and post-consumer disposal. Likewise, it is imperative to develop robust and reliable sampling and analytical methods to collect information regarding the nanoparticle release mechanisms that are active in different products under different use conditions and to assess the nanoparticle release rate associated with a given mechanism.

Multi-walled carbon nanotubes (MWCNTs) are commonly used as nanomaterial filler in many different types of polymer composite materials to lend favorable mechanical and electrical properties. These MWCNT nanocomposites are increasingly utilized in aerospace, automotive, and consumer goods industries as high performance base materials. Currently, carbon nanotubes (CNTs) account for more than a quarter of the market share of overall nanomaterials demand [2]. Based on a recent market analysis report, the current global CNT production capacity is in the range of 10,000 metric tons and the majority of CNTs produced are MWCNTs rather than single walled carbon nanotubes (SWCNTs). Within the consumer goods industry, MWCNTs have been widely used in the manufacture of sporting goods such as baseball bats, golf clubs, bicycle frames, and safety helmets. Recently, MWCNTs have also found service in textile applications, such as heated clothing and children's anti-ballistic backpacks.

The purposes of this research were to develop methods for detecting MWCNTs in textile based children's products and to assess MWCNT release from these products during mechanical wear conditions. The initial focus was on three types of soft armor inserts used in children's anti-ballistics backpacks. The analytical techniques and experimental platforms that were developed for analyzing MWCNT epoxy nanocomposites, under the interagency agreements CPSC-I-12-0009 and CPSC-I-08-0008-Mod3, were adapted here for use in evaluating and analyzing textile products that contain MWCNTs. The earlier epoxy nanocomposite work included topics such as: the development of safe handling procedures for sample processing, the evaluation of various analytical techniques for the detection and the analysis of MWCNTs in sporting goods, and the development of methods to assess release of MWCNTs in specific use- case scenarios. Current efforts were focused on the adaptation, refinement, and optimization of the existing epoxy nanocomposite abrasion, sampling, and analysis methods/techniques for use in MWCNT textile analysis.

4 APPROACH SUMMARY

Currently there are several commercially available ballistic products that are either marketed for children's use or likely to be used by children. Many of them are ballistic inserts that can be used inside backpacks or shoulder bags. There are also ballistic jackets and blankets. For this work, we focused on the products that, based on the manufacturer's labeling, contained MWCNTs - one ballistic backpack and two types of ballistic inserts marketed for backpacks.

Specifically, our work was aimed at:

1. developing sample collection and preparation methods for the scanning electron microscopy (SEM) analysis of MWCNT-containing fiber and textile products,
2. developing an experimental platform for generating and collecting wear particles from textile products, and
3. refining and optimizing the SEM methods for the detection and analysis of the MWCNTs in the ballistic products and for assessing the release of MWNCTs from these products during normal use and foreseeable misuse scenarios.

A detailed analysis of the construction of the ballistic products was performed to identify and confirm the presence of MWCNTs in the product samples. These analyses were carried out using Raman spectroscopy, optical microscopy, scanning electron microscopy (SEM) and transmission electron microscopy (TEM). Once the MWCNT containing components were identified, several release scenarios were considered based on the design of the product and the durability of the materials used. The evaluation of the MWCNT release was performed using a custom-built abrasion test apparatus. Several different types of particle sampling approaches were used and the analysis of the collected particles was performed using SEM and TEM. This work significantly leveraged the various methods and facilities previously developed at NIST for the analysis of MWCNT nanocomposites in consumer products. However, differences in sample geometry, MWCNT incorporation methods, and use scenarios of the textile products required that the existing tools and methods be adapted for use with these materials.

5 METHODS AND RESULTS

5.1 Product Analysis

5.1.1 Product Sample Description

Three different commercially available MWCNT containing ballistic product samples were used to develop practical sample preparation, testing, and analysis methods for detecting MWCNTs in the products and for assessing the release of MWCNTs from these products. These products

were selected based on the manufacturers' claims that the products contain MWCNTs. They were:

- [redacted] Youth Backpack
- [redacted] ballistic insert
- [redacted] ballistic insert

5.1.1.1 [redacted] *Youth Ballistic Backpacks*

Three (3) youth ballistic backpacks were purchased from [redacted] as test samples. According to the manufacturer's website, MWCNTs are incorporated into a new type of armor called [redacted] which is "*much lighter, stronger, more flexible, thinner and has much less back-face deformation*" than traditional armor. See Appendix I for the manufacturer's description of [redacted].

Figure 1: [redacted] Youth Ballistic Backpack photos showing the overall shape and the main compartment of the backpacks. Ballistic panels were sewn into the back of the two red and black backpacks but the ballistic panel for the gray and black backpack was placed inside the laptop sleeve (f).

Figure 1 shows the photos of the three youth ballistic backpacks (backpacks from here on in) that were examined. Two of the backpacks had the ballistic panels sewn into the backside of the backpack (Figures 1a, b, d, e) and the third backpack had the ballistic panel placed in the laptop sleeve of the backpack (Figures 1c, f). Figure 2 shows the schematics of the two different backpack configurations.

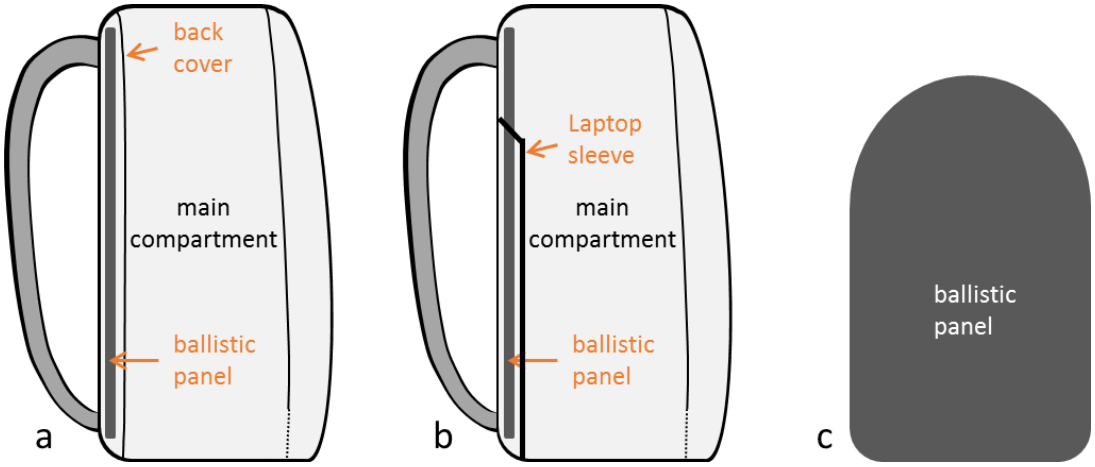

Figure 2: Schematics of two different types of [redacted] backpacks showing the locations of the ballistic panels. In the red and black backpacks, the ballistic panel was sewn into the back of the backpack (a). In the gray and black backpack, the ballistic panel was placed in the laptop sleeve of the backpack. c) shows the general shape of the ballistic panel in both types of backpacks.

The backside lining of the sewn-in configuration was an add-on cover stitched on to the back of the backpack and easily detached (white arrow on Figure 3b). Once the backside lining was loosened, the ballistic panel could be removed from the backpack.

Figure 3: Photo of the sewn-in type [redacted] backpack showing a) the backside lining of the backpack, b) stitching of the liner, and c) the exposed ballistic insert after the backside lining was removed.

The ballistic panels from all three backpacks had the same shape, size and structure. Each ballistic panel was encased in a water-resistant sealed nylon outer sleeve with a label containing the ballistic protection level[1] of the ballistic panel and the basic use and care instructions. The label side of the ballistic panel also indicated that it is the side that should face the body. Figure 4a shows the heat-sealed edge of the sleeve. Inside the sleeve was a stack of ballistic textile sheets that were sewn together (Figure 4b & c).

[1] *NIJ Standard–0101.06, "Ballistic Resistance of Body Armor," is a minimum performance standard developed in collaboration with the Office of Law Enforcement Standards (OLES) of the National Institute of Standards and Technology (NIST).*

Figure 4: Photos of an [redacted] ballistic panel showing a) the ballistic panel in its outer casing, b) the ballistic panel with its outer casing removed, and c) the individual layers of the ballistic panel.

There were 20 sheets of ballistic material in each panel, arranged in the following order: 4 black sheets, 13 white sheets, 3 black sheets (Figure 5). The white layers were stamped with the [redacted] trademark. [redacted] is a type of ultra-high molecular weight polyethylene (UHMWPE) commonly used in ballistic panels. Each black sheet consisted of a light inner layer with a thick, slightly tacky black coating applied on both sides (Figure 6).

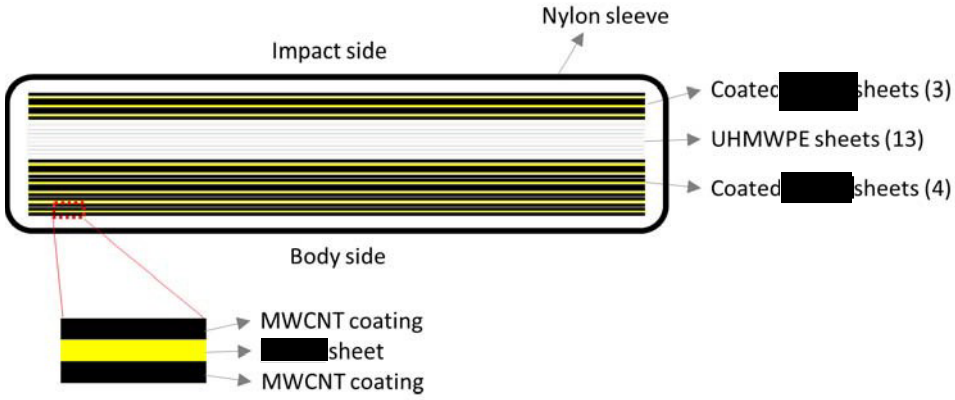

Figure 5: Schematic diagram of the [redacted] backpack ballistic panel showing the layered construction.

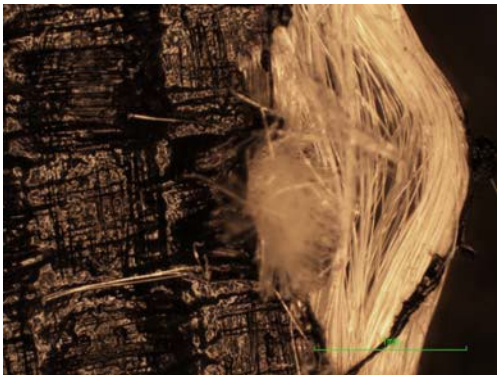

Figure 6: Cross section of a black sheet from the [redacted] ballistic panel showing that the sheet contains woven [redacted] fabric coated with black 'tacky' material on both sides.

5.1.1.2 [redacted] *Ballistic Insert*

Three (3) rectangular ballistic inserts were purchased from [redacted]. These inserts were 6" by 8" in size and came in heat sealed water resistant polyester sleeves. According to the manufacturer's website, the ballistic panel is made with a composite containing [redacted] blend, CNT, and EIP foam (see Appendix 2 for the product information). EIP foam presumably refers to ethylene interpolymer (or copolymer) foam that is often used in ballistic applications as a shock absorbing material.

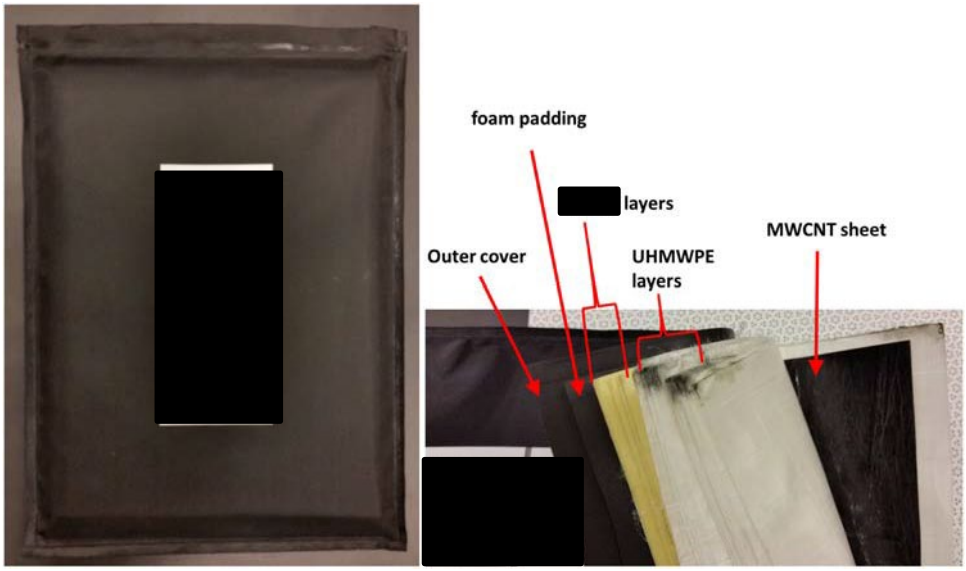

Figure 7: Photos of an [redacted] ballistic insert showing the ballistic panel in the sealed sleeve (left) and the multiple layer structure of the ballistic panel showing the foam padding, [redacted], UHMWPE, and MWCNT sheets.

Figure 7 shows an [redacted] ballistic insert. The polyester outer sleeve can be removed relatively easily using a pair of scissors. Each ballistic panel consisted of two (2) plies of foam padding, six (6) sheets of [redacted], twenty-two (22) sheets of UHMWPE, with a single MWCNT sheet sandwiched between the last two UHWMPE sheets (Figure 8). As with the [redacted] backpack ballistic panels, the [redacted] ballistic panels also had labels on one side describing the ballistic protection level of the panel and the use and care instructions.

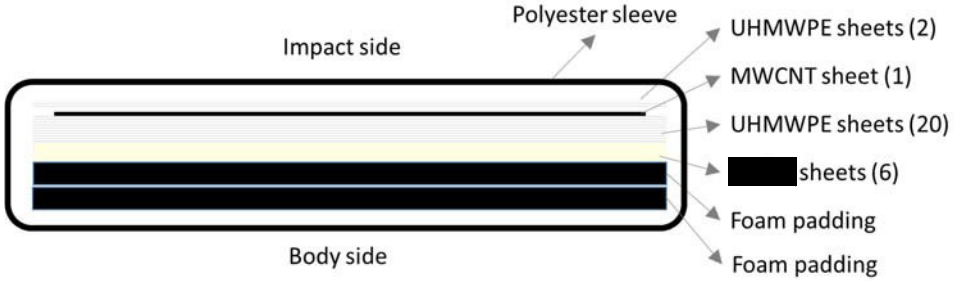

Figure 8: Schematic diagram of the [redacted] ballistic insert showing the layered construction.

5.1.1.3 [redacted] *Ballistic Insert*

One (1) rectangular ballistic insert was purchased from [redacted]. The insert was sold as a backpack insert. The insert was 11" by 14" in size and came in a heat-sealed polyester sleeve. According to the manufacturer's website, the ballistic panel is a carbon nanotube reinforced ballistic soft panel with non-Newtonian back face (see Appendix 3 for the product information) where non-Newtonian presumably indicates the shear-thickening property of ethylene interpolymer (or copolymer) foam that is often used as a shock absorber.

Overall construction of the [redacted] ballistic insert was the same as the [redacted] ballistic inserts (Figures 9 & 10).

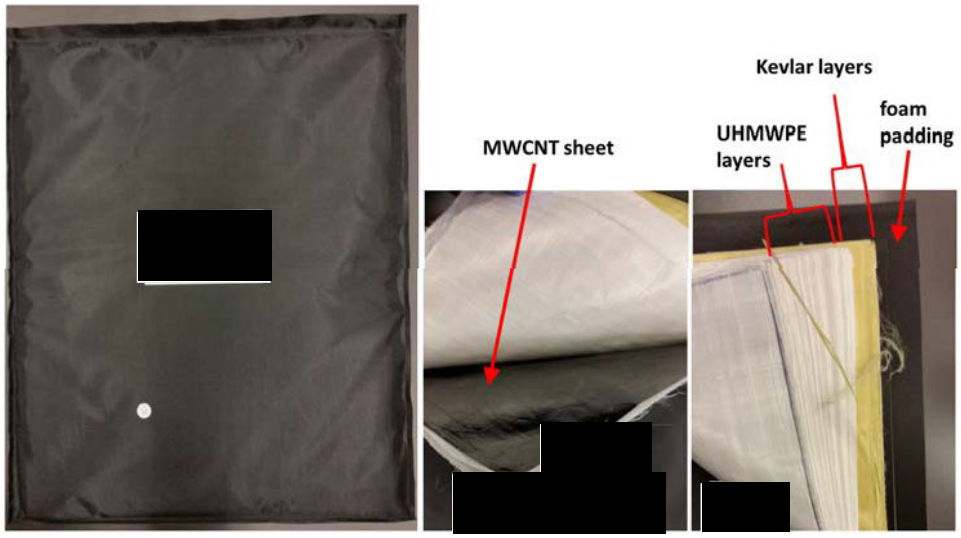

Figure 9: Photos of an [redacted] ballistic insert showing the ballistic panel in the sealed polyester sleeve (left) and the multiple layer structure of the ballistic panel showing the foam padding, [redacted], UHMWPE, and MWCNT sheets.

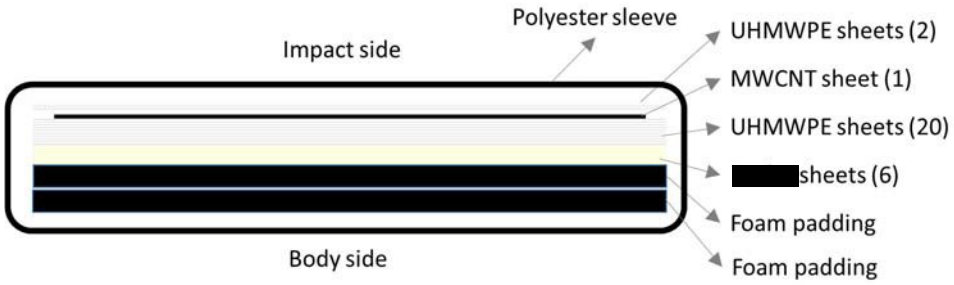

Figure 10: Schematic diagram of the [redacted] ballistic insert showing the layered construction. The layer structure and the ordering of the ballistic layers are the same as the [redacted] ballistic inserts.

5.1.2 MWCNTs in Ballistic Material Samples

Raman spectroscopy and electron microscopy were used to confirm the presence of MWCNTs in the ballistic products. Raman spectroscopy was performed using a scanning Raman microscope constructed in-house and based on an upright microscope with multiple fiber- coupled laser sources. Electron microscopy (SEM) was performed using an FEI Helios 650 focused ion beam scanning electron microscope (FIB/SEM), a Hitachi S5500 SEM in scanning transmission electron microscopy (STEM) mode, and an FEI Titan 80-300 scanning transmission electron microscope (S/TEM).

5.1.2.1 Raman Spectroscopy

Raman spectroscopy was used to analyze small pieces (approx. 5mm x 5mm) of the CNT containing materials found in the soft armor inserts, i.e. the black layer from the [redacted] backpack ballistic panel, and the MWCNT sheets from the [redacted] and [redacted] ballistic inserts. Because of the variations in the tube diameter, number of walls, and overall quality of the tubes in most batches of MWCNTs, the Raman peaks of MWCNTs are quite broad compared to single wall CNTs and slight shifts in peak positions are common depending on the conditions and properties of the MWCNTs. However, the presence of the D band at ~1300 cm^{-1} representing the defects in graphene lattice, the G band at ~1600 cm^{-1} representing the graphitic material, and the 2D band at ~2600 cm^{-1} are the signature peaks that indicate the presence of MWCNTs in the structure [3].

Figure 11 shows Raman maps and spectra from the MWCNT containing layers of the three different ballistic panel materials. These measurements were taken with an excitation wavelength of 532 nm and 0.5 mW power through a 0.95 NA air objective. Images were acquired using an avalanche photodiode (APD) with a bandpass filter with a FWHM (full width at half maximum) of 300cm^{-1} centered on the G band (1555 cm^{-1}). The Raman map of the [redacted] material shows a strong spatial dependency in the measured Raman intensity, indicating that the MWCNTs are not uniformly dispersed in the sample. The Raman maps of the [redacted] and the [redacted] samples exhibited clear, uniform level of MWCNT signals (peaks) over the entire imaging area with little spatial variation in intensity except at a few small hot spots. The Raman spectra were dominated by the features that correspond to MWCNTs, including very well defined 2D (G') peaks at ~2560 cm^{-1}. Raman spectra were also collected from the non-MWCNT containing materials in the [redacted] insert. A fiber pulled from the woven interior of one of the black sheets in the [redacted] material yielded a Raman spectrum that was consistent with [redacted]. The Raman spectrum of the white [redacted] branded sheet was found to be consistent with polyethylene, as expected.

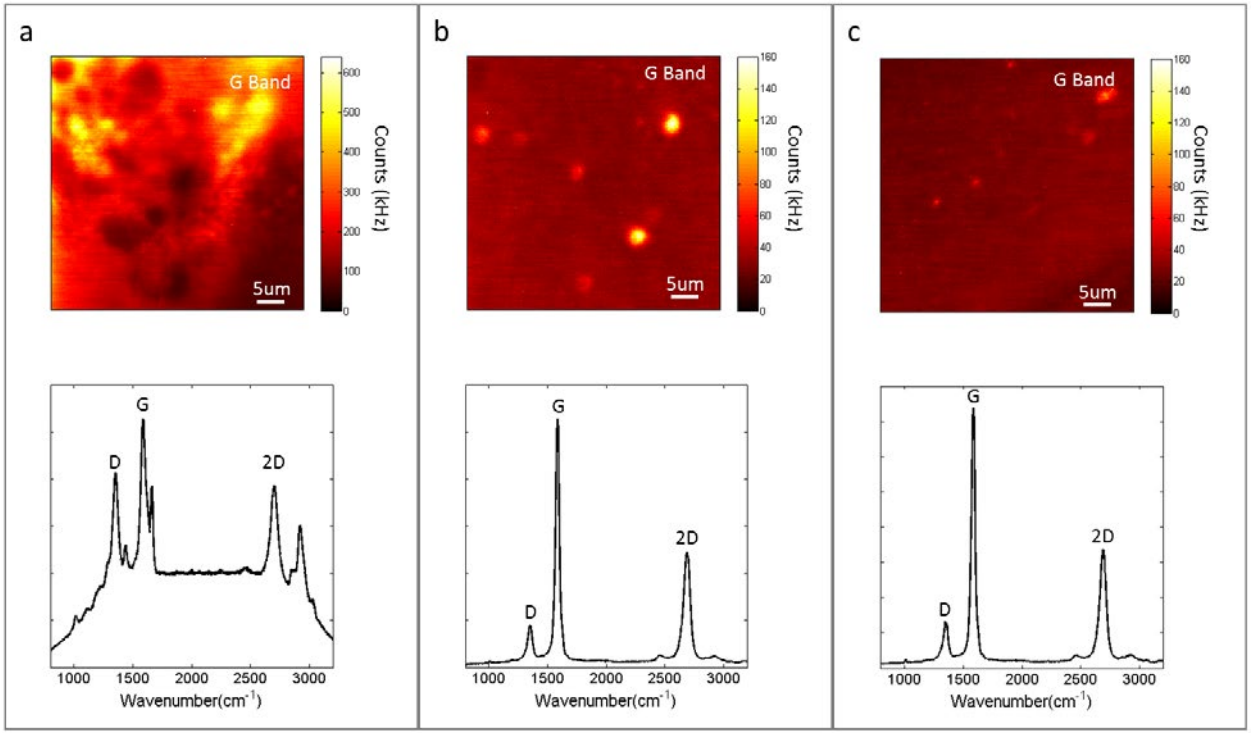

Figure 11: Raman maps and single spot spectra of the a) [redacted] black coating, b) [redacted] MWCNT sheet, and c) [redacted] MWCNT sheet samples showing clear MWCNT signatures.

5.1.2.2 Electron Microscopy

5.1.2.2.1 Sample Preparation for Electron Microscopy

The soft armor inserts were constructed in a layered fashion, as discussed above. [redacted] shears were used to cut a small piece from each of the parent inserts for study. The layer containing the MWCNTs was then isolated and mounted on an aluminum SEM stub using conductive carbon tape or silver paint. No conductive coating was applied to the specimens prior to imaging. All SEM images were acquired with secondary electron (SEs), unless otherwise noted, or if the instrument was operating in a transmission mode. SEM images were collected in a FEI Helios 650 FIB/SEM instrument.

The SEM specimens were also used in the preparation of TEM samples by conventional site-specific *in-situ* lift-out technique in an FEI Helios 650 FIB/SEM instrument equipped with an Omniprobe Autoprobe 200 micromanipulator system. The lift-out sites were shielded from direct exposure to the ion beam by the electron beam induced deposition (EBID) of a platinum (Pt) cap. Two lift-out samples were extracted from each MWCNT containing material. The lift- out specimens were transferred to 3-post copper Omniprobe grids and affixed with EBID Pt before milling to final thickness.

Generally, the lift-out samples were not rigid enough to survive the process of being ion milled to electron transparency across their full dimensions. Additional support was provided by

surrounding the area to be thinned with an EBID Pt frame (e.g. Figure 12a) and/or by leaving some regions of the sample un-thinned (e.g. Figure 12b). However, even with these reinforcement techniques in place, the mid-region of the thin section can bow out, resulting in a loss of specimen area during subsequent milling (Figure 12a).

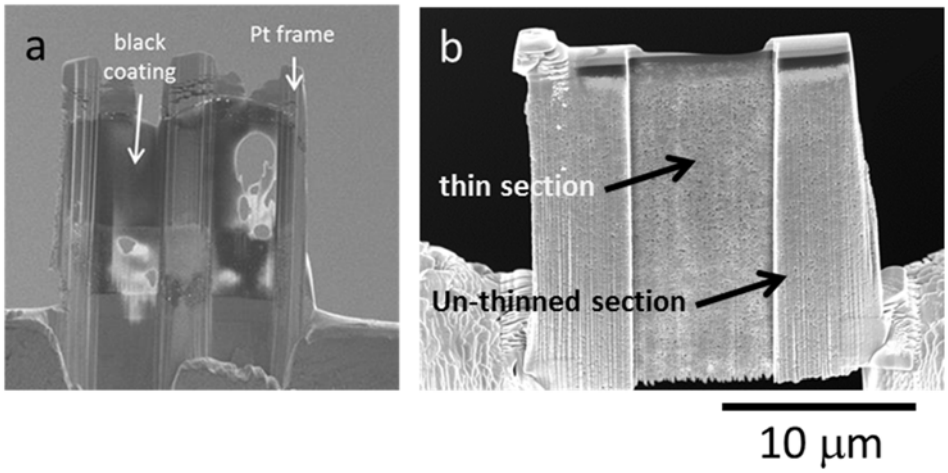

Figure 12: The reinforcement of TEM lift-out samples during thinning. (a) [redacted] sample reinforced by a Pt frame and central pillar. Although the thinned region is not very uniform, there is a sufficient amount of electron transparent material for S/TEM analysis. (b) [redacted] sample reinforced by leaving some material un-thinned.

The empty trenches left behind in the SEM samples by the TEM lift-out process provided an opportunity to collect images of the MWCNT containing materials in cross section. At 0° stage tilt, the ion beam was used to mill an inclined surface into the sidewall of the empty lift-out trench (Figure 13). Since the angle between the electron beam and the ion beam is 52°, a 38° stage tilt can then be used to position the newly exposed surface perpendicular to the electron beam for SEM imaging.

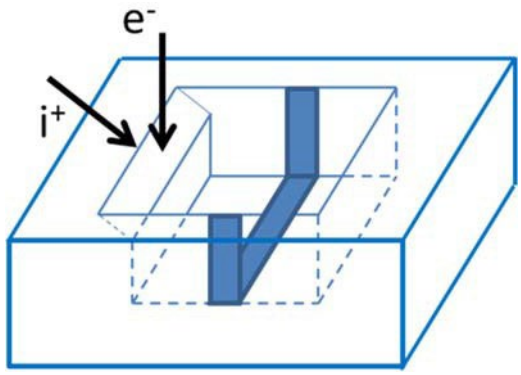

Figure 13: Schematic diagram of the site left behind in an SEM sample after extraction of a TEM lift-out sample. The site formerly occupied by the lift-out sample is shown in blue fill. A stage tilt of 0° is used during the milling

of the new surface. Therefore, a stage tilt of 38° will position the newly exposed surface perpendicular to the electron beam for SEM imaging (the angle between the ion beam and the electron beam is 52°).

5.1.2.2.2 SEM Imaging of FIB Prepared Cross Sections

The empty trenches left behind in the SEM samples by the TEM lift-out process provided an opportunity to collect images of the MWCNT containing materials in cross section. Figure 14 and Figure 15 contain SE images of FIB prepared cross sections from the [redacted] and the [redacted] materials. The microstructure observed in these two materials appears to be quite similar. Both materials have a polymer film, of about 1 μm in thickness, on the outer surfaces of the MWCNT sheet. The film is visible near the top of the images in Figure 14. Also, neither the [redacted] nor the [redacted] material is fully dense, as indicated by the images of the interior of the CNT sheet that are provided in Figure 15. The [redacted] MWCNT containing material, on the other hand, is nearly fully dense in cross section (Figure 16).

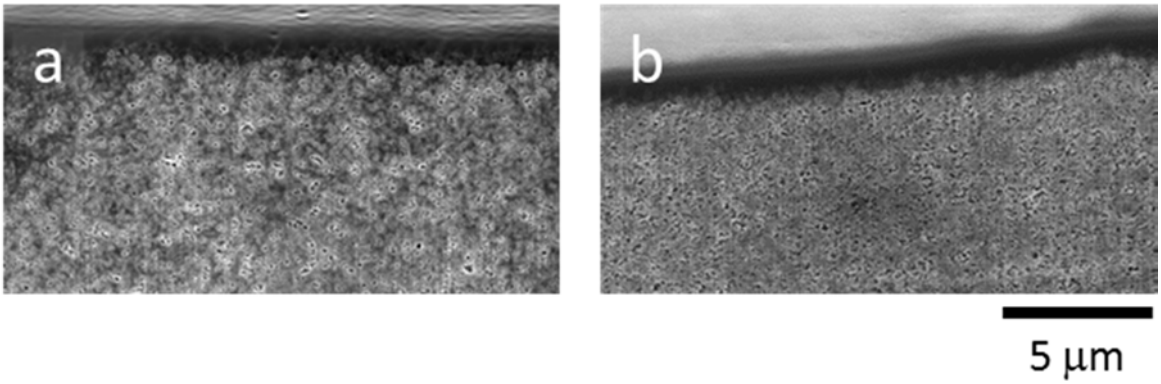

Figure 14: SE images of FIB prepared cross sections of the (a) [redacted] and (b) [redacted] MWCNT sheets. A polymer film on the outer surface of the sheet material is visible at the top of both images.

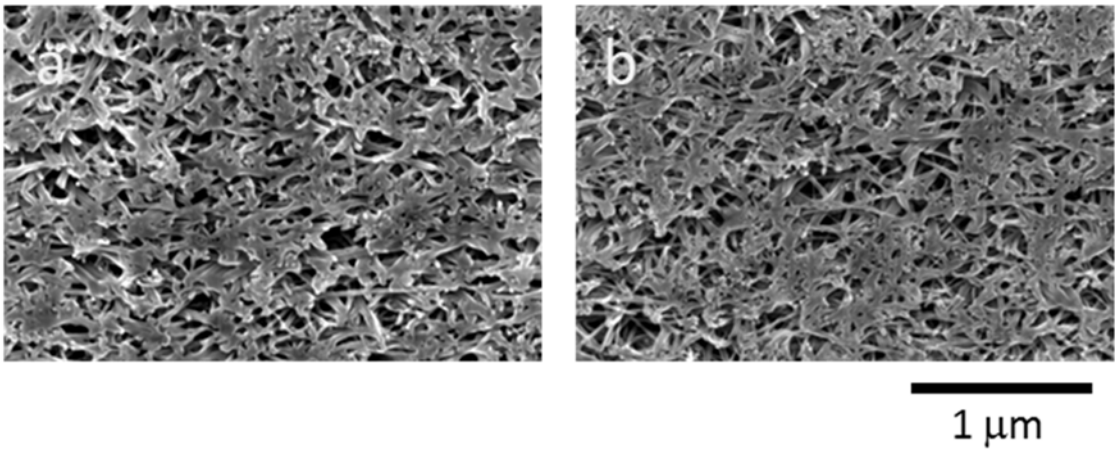

Figure 15: SE images of FIB prepared cross sections showing the interior of the (a) [redacted] and (b) [redacted] MWCNT sheets.

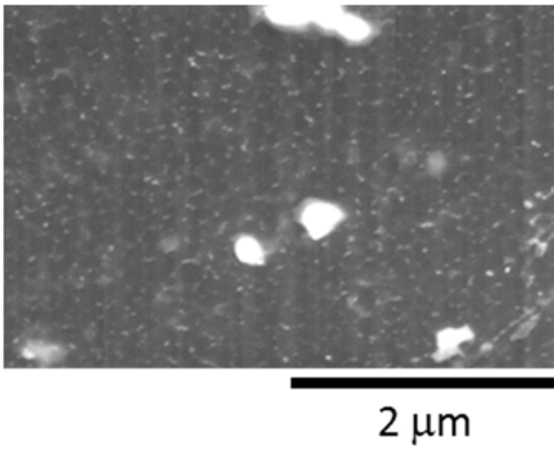

Figure 16: SE image of a FIB prepared cross section of the [redacted] MWCNT containing material. The structure is almost fully dense.

5.1.2.2.3 SEM Imaging of Delaminated MWCNT Sheet Structure

During routine handling of the [redacted] and [redacted] MWCNT sheet samples, incidental folds were sometimes formed near the edges of the samples. Figure 17 shows one such fold on a sample of the [redacted] MWCNT sheet. Here the material has been bent upward, i.e. out of the plane of the page, toward the reader. The fold caused the MWCNT sheet to delaminate into 3 separate plies. Delamination was also induced by the cutting action of the [redacted] shears or the knife blade that was used to size the samples. Figure 18 shows one example of this type of delamination. The passage of the cutting tool tends to smear the structure on the cut edge, thereby masking the true nature of the structure. The FIB was used to clear the smeared material from the edge of the sheet to reveal the delamination event shown in Figure 18.

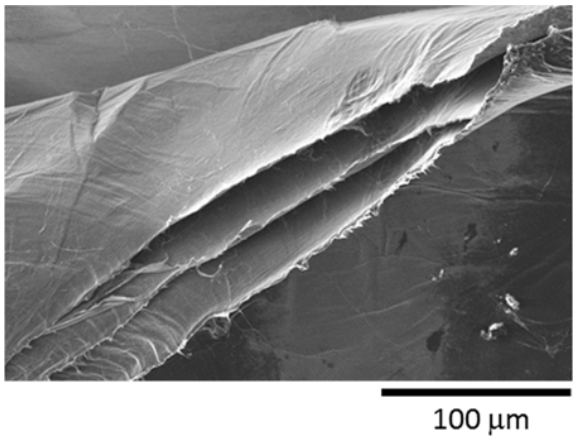

Figure 17: SE image showing delamination of an [redacted] MWCNT sheet as a result of an incidental upward fold that occurred near the edge of the sample. The single sheet has separated into three plies as a result of the fold.

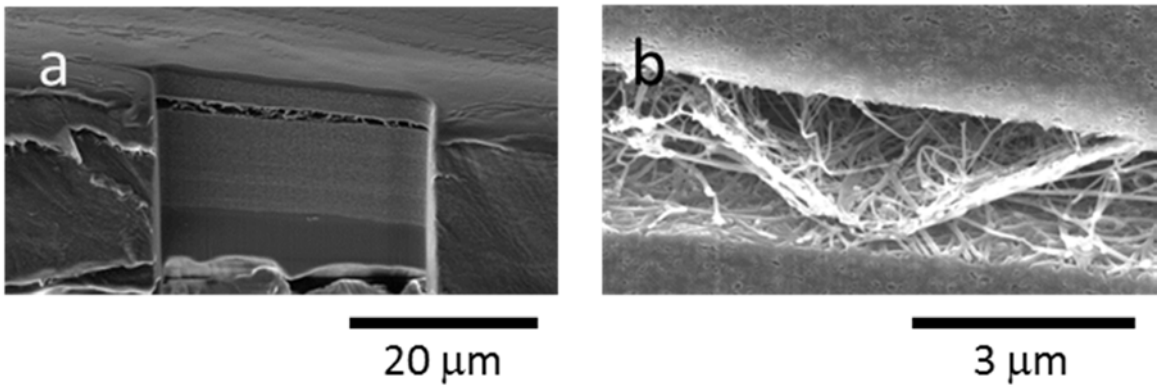

Figure 18: SE images showing incidental delamination in an [redacted] MWCNT sheet. (a) FIB cross section prepared on the edge of the sheet to reveal the delamination. (b) The interior structure of the delaminated region of the MWCNT sheet in (a).

The implication here is that the MWCNT sheet material can be readily delaminated to expose its interior without causing a significant disruption of the native structure. Therefore, the interior structure observed in a peeled MWCNT sheet could be used to validate the comparable structure observed in a FIB prepared cross section. In an effort to qualify the microstructure that was observed in the FIB prepared cross sections of the [redacted] MWCNT sheet material (Figure 15b), a sample of the material was delaminated using forceps under an optical microscope. Figure 19 shows the interior structure of the peeled [redacted] MWCNT sheet. Comparing the left-hand side of Figure 19a to the right-hand side indicated a densification/compression of the structure on the right-hand side of the image. The right-hand side of Figure 19a contains the edge of the sample that had been cut during the sizing of the sample and is a demonstration of how the cutting of the specimen can locally alter the native structure. As observed in the FIB prepared cross section, the interior structure of the sheet is not fully dense and is made up of an entanglement of filaments. As will be discussed further in the section on S/TEM, it is believed that each filament consists of bundled MWCNTs. At present, it is not clear how the MWCNTs are bound together in these bundles, though it is possible that the MWCNTs are coated with a polymer. Figure 19c and Figure 19d show evidence that smaller filaments can split apart and branch out from larger filaments.

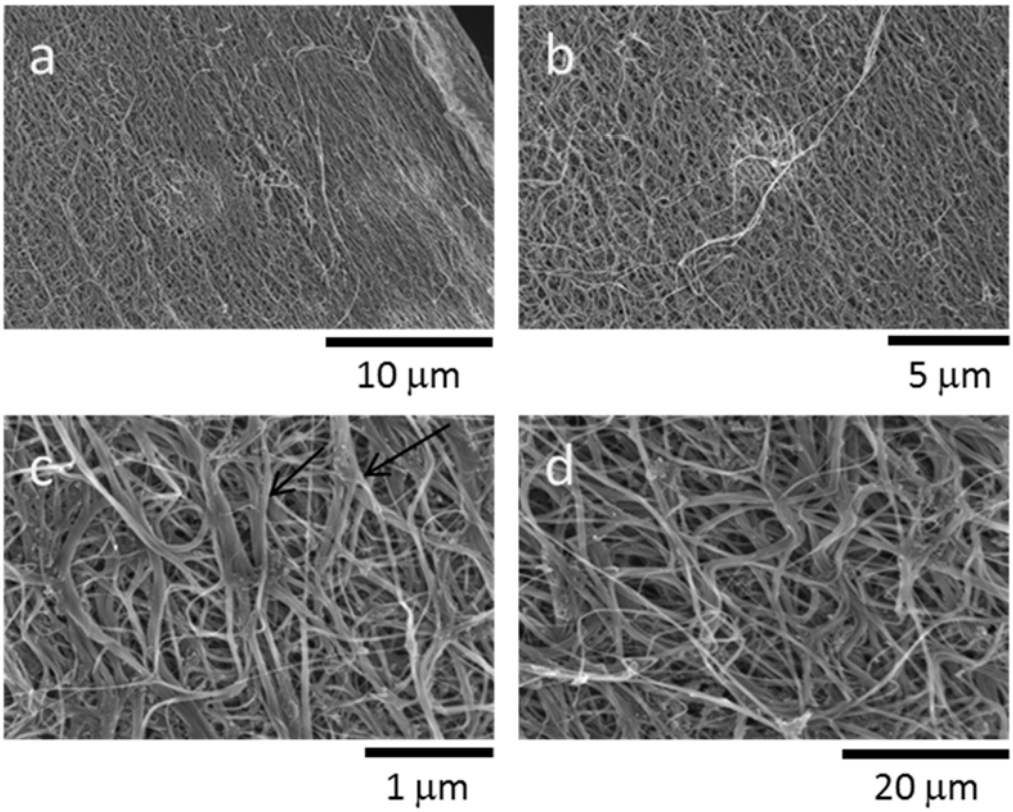

Figure 19: SE images of the interior of a sample of the [redacted] MWCNT sheet. Note how the open structure observed on the left side of (a) and in (b) is compressed near the sample edge on the right-hand side of (a). The bundles of tubes are observed to split apart and branch out in both (c) and (d), as indicated by the black arrows in (c).

5.1.2.2.4 SEM Imaging of MWCNT Surface Structure

As mentioned earlier, the outer surfaces of the [redacted] and the [redacted] MWCNT sheet materials have a polymer capping film that is nominally 1 µm in thickness. The film is visible near the top of the cross-section images in Figure 14. However, SEM imaging revealed ridges, or wrinkles, on the surface of the MWCNT sheets (Figure 20a and Figure 20c) where the capping film was absent. Therefore, as shown in Figure 20b and Figure 20d, the ridges constitute exposed material from the interior of the MWCNT sheet. This also may explain the occasional hot spots (small areas of higher MWCNT signal intensity) that were observed in the Raman maps of the [redacted] and the [redacted] MWCNT sheets.

For the sake of completeness, a SE image of the surface of the [redacted] MWCNT material has been included as Figure 21. The image shows sub-surface embedded MWCNTs in the near surface region of the specimen.

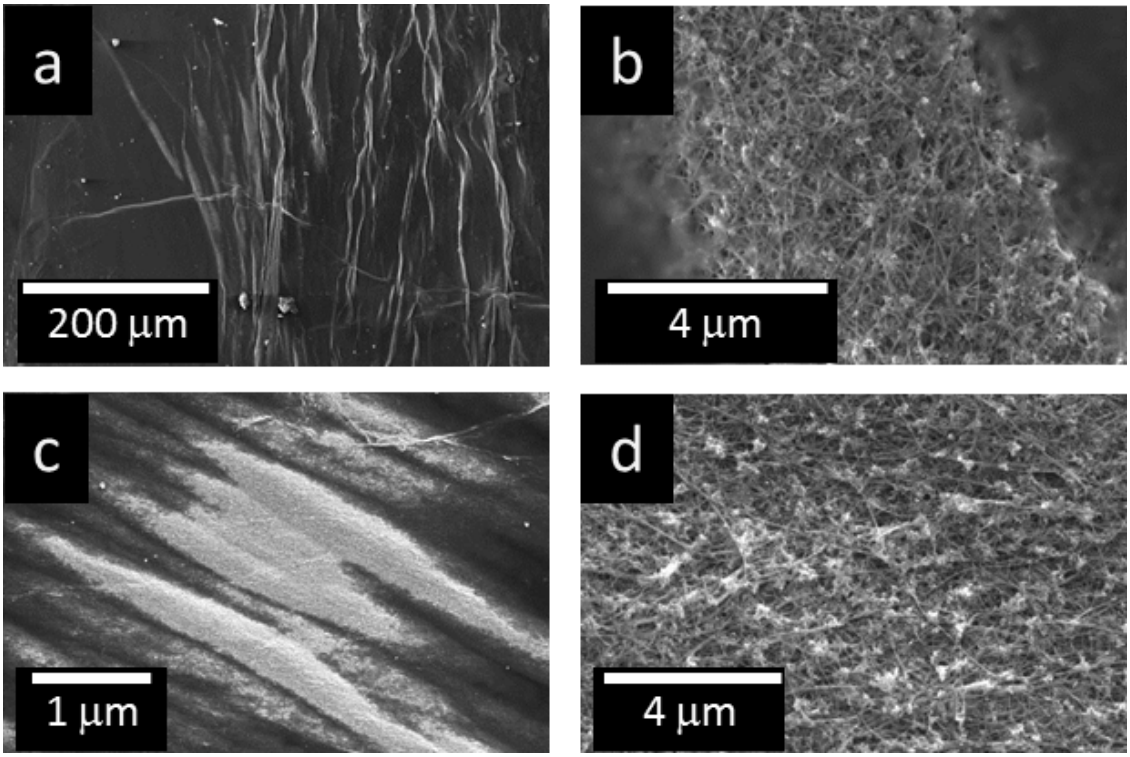

Figure 20: SE images of exposed MWCNT materials on the surfaces both the (a - b) [redacted] and (c - d) [redacted] r MWCNT sheet materials. The polymer surface film does not fully cover the wrinkles in the underlying MWCNT material.

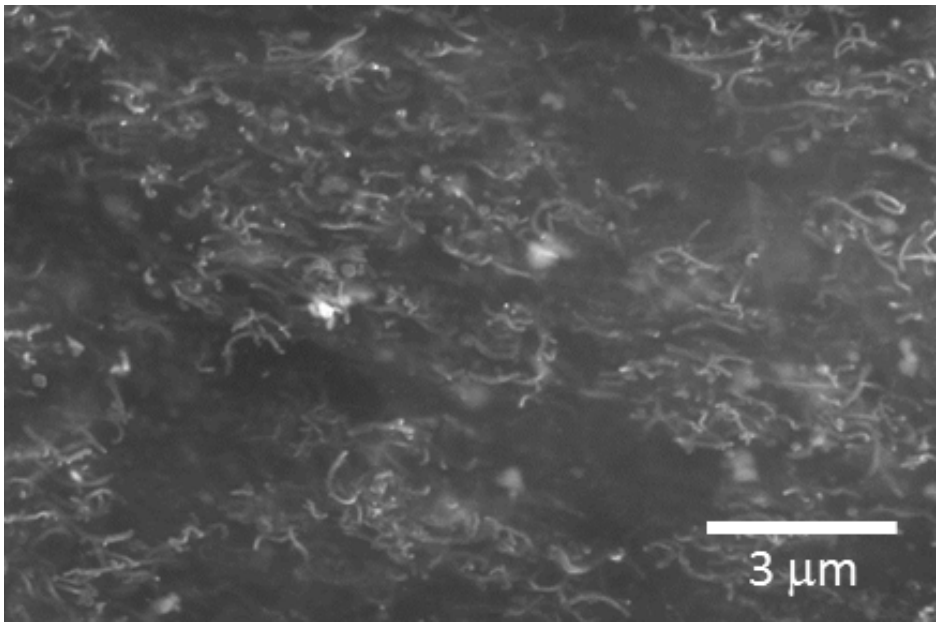

Figure 21: SE image showing the presence of embedded MWCNTs just beneath the surface of the [redacted] material (20kV).

5.1.2.2.5 TEM/STEM Imaging and Qualitative Chemical Analysis

With the exception of a few SEM-STEM images collected on the [redacted] material, all TEM and STEM work was completed on an FEI Titan 80-300 S/TEM equipped with an EDAX r-TEM EDS (energy dispersive x-ray spectrometer) Si(Li) detector.

[redacted]

Thin sections of the [redacted] MWCNT material were analyzed using STEM in a Hitachi S5500 SEM. Although not as powerful as the conventional S/TEM instrument, SEM-STEM imaging provides higher resolution images of thin section samples than traditional SEM imaging. Figure 22 shows a couple of the STEM images collected from the black coating material (Figure 6). Although the individual walls are not clearly defined, the overall structure of the MWCNTs (red arrows in Figure 22a) was easily distinguishable. There were many MWCNT segments dispersed throughout the thin section, indicating a relatively high concentration of MWCNTs in the coating material.

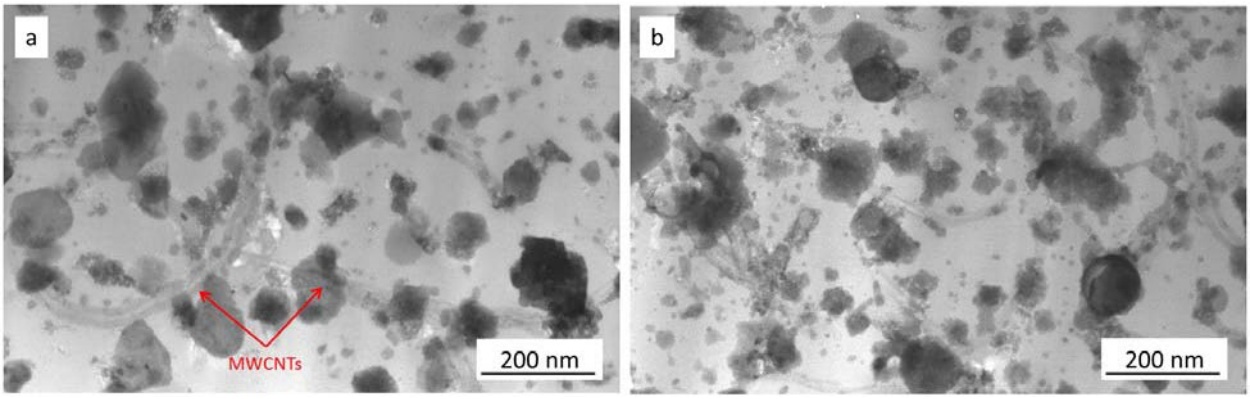

Figure 22: STEM images of the [redacted] thin section showing segments of MWCNTs dispersed throughout.

Figure 23 shows higher magnification STEM images of the MWCNTs. Here, we can almost see the multi-walled structure of the tubes. The MWCNT shown in Figure 23a has a 35 nm outer diameter and a 13 nm inner diameter. In general, the MWCNT outer diameters ranged from less than 30 nm to about 60 nm. Some of the MWCNTs contained metal nanoparticles, which are probably catalyst particles, as shown in Figure 23b.

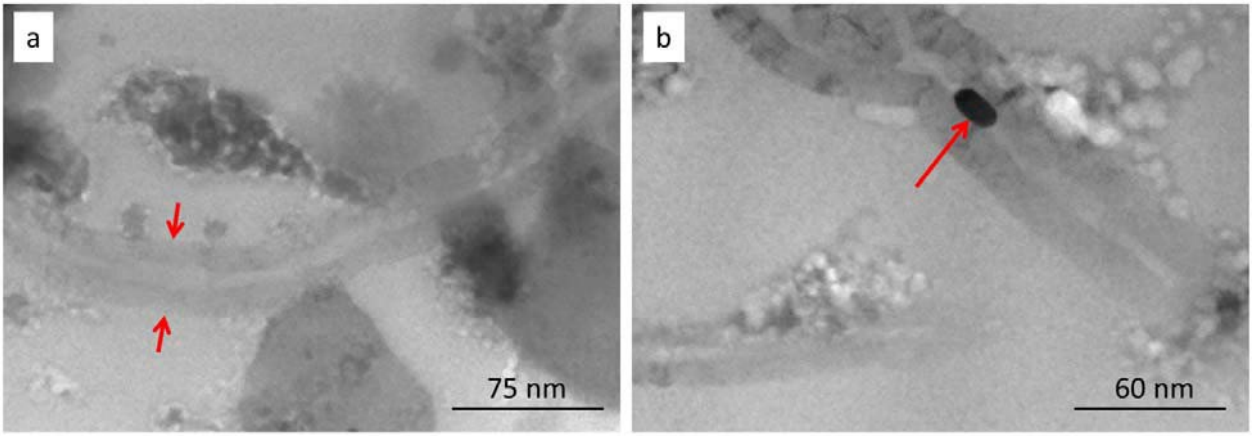

Figure 23: Higher magnification STEM image of the MWCNTs in the black coating material of the [redacted] sample showing (a) a MWCNT with a 35 nm outer diameter and (b) a MWCNT with metal (possibly catalyst) particle inside.

A conventional TEM-BF (bright field) image of the [redacted] material is shown in Figure 24a. MWCNTs and other inclusions are seen distributed throughout the polymer matrix as shown in the earlier SEM-STEM images. Dark round regions in Figure 24a and corresponding holes in Figures 24b and c are from the carbon contamination during initial imaging and the electron beam damage sustained during the EDS analysis. The black arrow in Figure 24b points to one of the MWCNTs in the image.

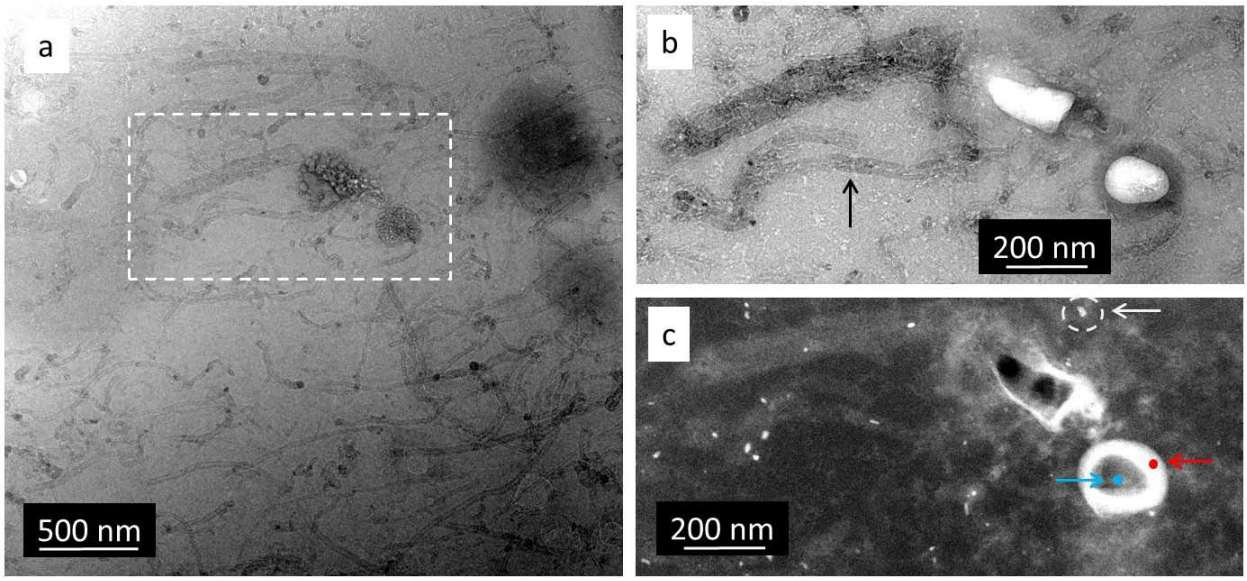

Figure 24: (a) TEM image showing MWCNTs distributed throughout the polymer matrix of the [redacted] material. Higher resolution matched (b) TEM-BF and (c) STEM-HAADF electron images of the rectangular inset shown in (a). The arrows in (c) indicate some of the regions interrogated by STEM-EDS.

Figure 24b and Figure 24c show a matched set of TEM-BF and STEM-HAADF (high angle annular dark field) electron images from the rectangular region marked in Figure 24a. The dominant

contrast mechanism in the STEM-HAADF image is Z-contrast, making the images similar to SEM backscatter electron images, i.e. lighter regions indicate higher Z. The arrows in Figure 24c indicate three locations in the sample that were interrogated by STEM-EDS. The EDS spectra for these three regions are provided below in Figure 25. STEM-EDS of the polymer matrix indicated the presence of carbon (C), chlorine (Cl), and oxygen (O) (spectrum not shown). The Cu signal found in all of the spectra may be due to the copper Omniprobe grid that the lift-out specimen was mounted to. Platinum (Pt) and gallium (Ga) signals in the EDS spectra are likely artifacts introduced by the FIB-based sample preparation process. Nanoparticles of the type indicated by the grey dashed circle / grey arrow are rich in nickel (Ni) (Figure 24c & Figure 25a). The Ni-rich particles are found throughout the material and may have been the catalyst particles for the MWCNTs. The larger particle indicated by the blue arrow (analysis performed at the blue dot) was found to contain zinc (Zn) (Figure 24c & Figure 25b). While the region immediately surrounding this particle, (indicated by the red arrow, analysis at performed at the red dot), was found to contain potassium (K) (Figure 24c & Figure 25c).

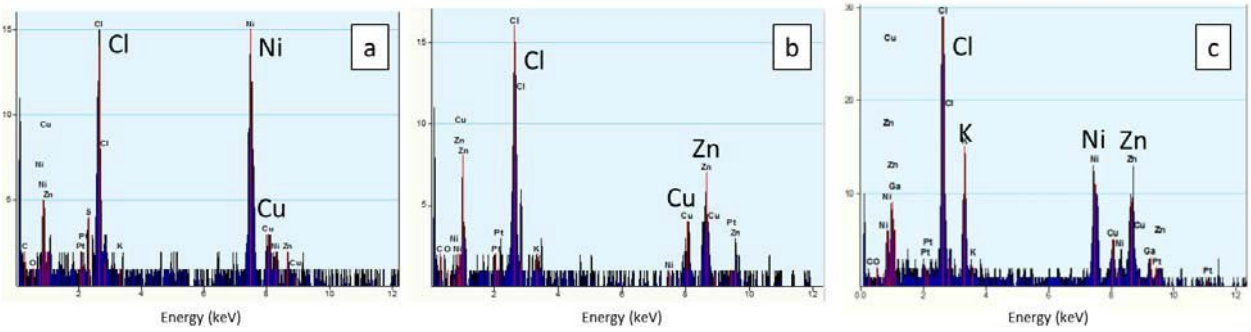

Figure 25: STEM-EDS spectra for the [redacted] material. (a) Ni-rich nanoparticle (gray arrow in Figure 24c). (b) Zn-rich nanoparticle (blue arrow in Figure 24c). (c) Region surrounding the Zn-rich nanoparticle (red arrow in Figure 24c).

[redacted]

Two TEM-BF images of the [redacted] material are shown in Figure 26. Unlike the [redacted] material, the [redacted] material lacked a matrix material to embed the MWCNTs. Rather, the [redacted] material appeared to be made up of entangled filaments and, as a result, was not fully dense. As shown earlier in the SEM images of the delaminated [redacted] structures, the filaments can split apart with smaller filaments branching off from larger filaments. It is very difficult to interpret the TEM images shown in Figure 26, but we believe the filaments to be comprised of bundles of MWCNTs. The red arrow in Figure 26b points to an example of the contrast striations that may indicate a bundle of MWCNTs. Figure 27 shows two additional higher resolution TEM-BF images of the [redacted] filaments confirming that the filaments are comprised of bundles of MWCNTs, although the number of MWCNTs and close packed structure of the MWCNT sheet make it difficult to determine the

number of the walls or the inner and the outer diameters of each MWCNT. In addition to the MWCNTs, there are also other inclusions present in the material. Raman spectroscopy indicated the presence of MWCNTs in the material and lattice fringes having a spacing consistent with graphite (0001) were observed in high magnification TEM images of the filaments (not shown here).

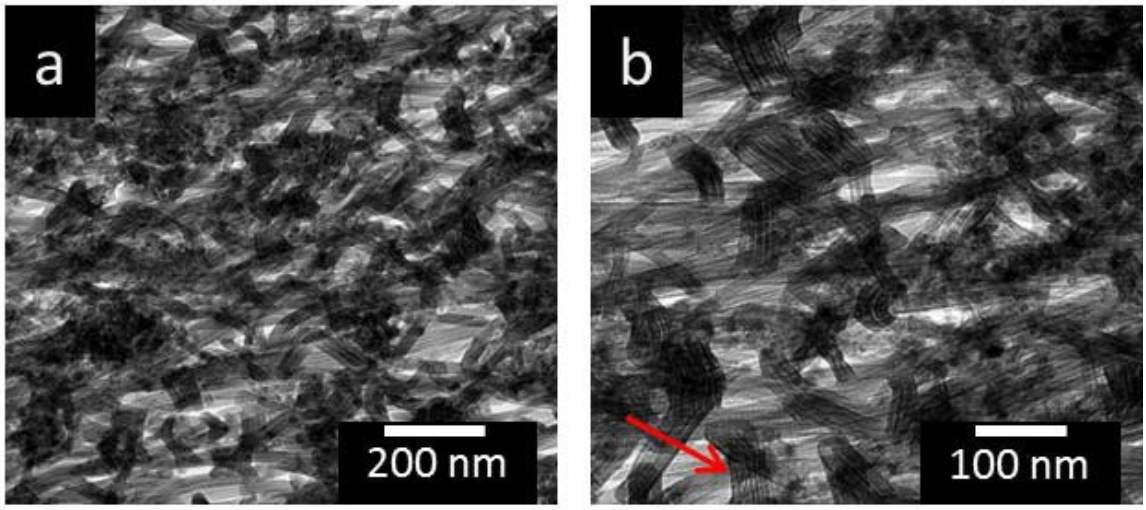

Figure 26: Two BF-TEM images showing the entangled filaments that make up the [redacted] material. The red arrow in (b) points to an example of contrast striations that could be indicative of MWCNT bundles.

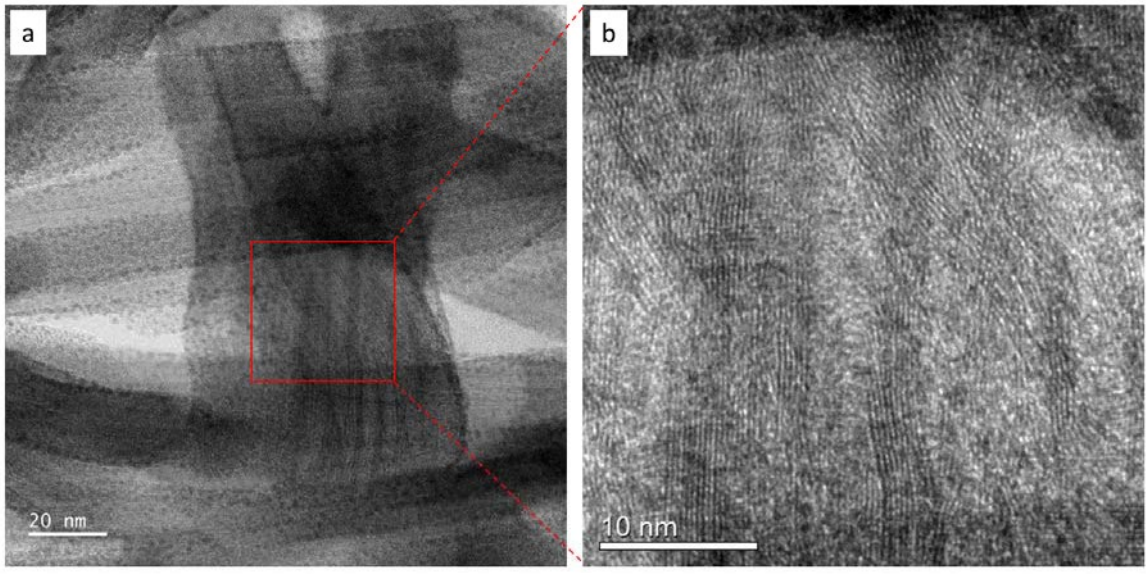

Figure 27: BF-TEM images showing the underlying structure of the [redacted] filaments. High resolution image of the inset (b) clearly shows the multi-walled structure of the MWCNTs but the overlapping tubes make it difficult to determine the MWCNT diameter or the number of walls in each tube.

Examples of the STEM-EDS spectra acquired from the [redacted] material are provided in Figure 28. Again, the Cu signal found in the spectra may be due to the copper Omniprobe grid

that the lift-out specimen was mounted to. The Pt and Ga signals in the EDS spectra are likely artifacts introduced by the FIB-based sample preparation process. The open structure of the [redacted] material makes it easy for re-deposited material to collect on the interior surfaces of the material during FIB milling. The EDS spectra for the filaments (suspected MWCNT bundles), as indicated by the red arrow in Figure 28a, only show C and the artifact signals associated with FIB sample prep (Figure 28b). Nanoparticles of the type indicated by the blue arrow in Figure 28a appear bright in the STEM-HAADF image, indicating the particle is of higher Z than the surrounding filaments. These particles are rich in Fe (Figure 28c). The Fe-rich particles are found throughout the material and may be the catalyst particles that were used for the growth of the MWCNTs.

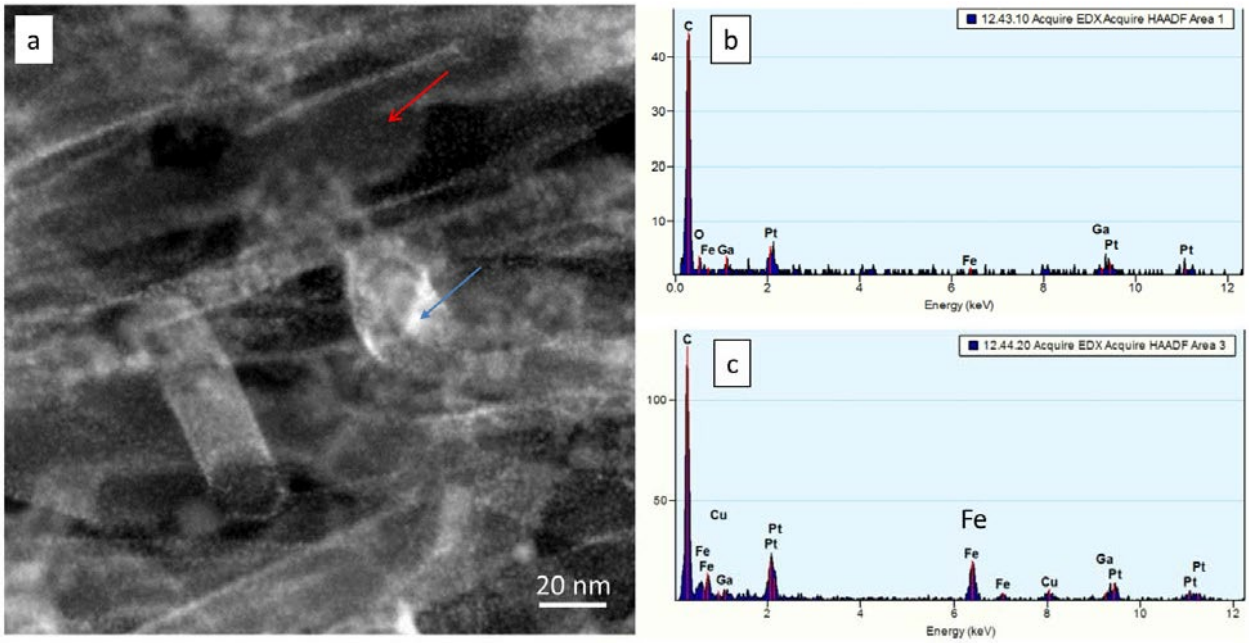

Figure 28: (a) STEM-HAADF image showing two locations probed by EDS in the [redacted] material. STEM- EDS spectra for (b) a filament (MWCNT bundle), as indicated by the red arrow in (a) and (c) an Fe-rich nanoparticle, as indicated by the blue arrow in (a).

[redacted]

Two TEM-BF images of the [redacted] material are shown in Figure 29. Similar to the [redacted] material, the [redacted] material appeared to be made of a tight but porous network of filaments. As shown earlier in the SEM images of the delaminated [redacted] structures, the filaments can split apart with smaller filaments branching off from larger filaments. TEM images of the [redacted] samples do not clearly show individual MWCNTs but the TEM images are very similar to those of [redacted] samples (Figure 26) and the contrast striations seen in Figure 29b may indicate bundles of MWCNTs. Raman spectroscopy indicated the presence of MWCNTs in the material and lattice fringes having a spacing

consistent with graphite (0001) were observed in high magnification TEM images of the filaments (not shown here). In addition to the MWCNTs, there are also other inclusions present in the material. Just below the red arrow, in Figure 29b, clusters of these particles can be seen.

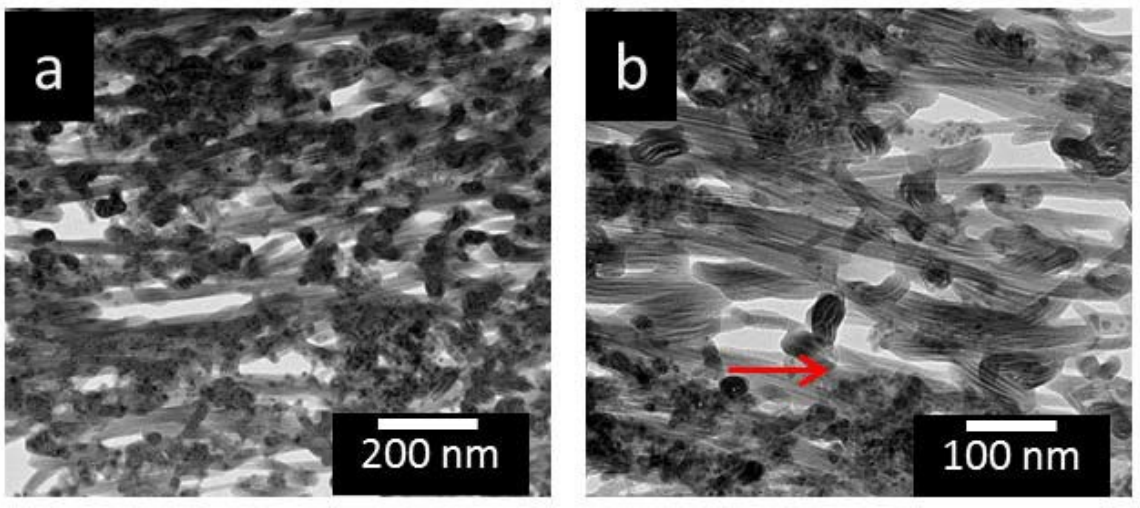

Figure 29: Two BF TEM images showing the entangled filaments that make up the [redacted] material. The grey arrow in (b) points to an example of the contrast striations that may be indicative of MWCNT bundles. A cluster of nanoparticle inclusions is visible just below the grey arrow.

Examples of the STEM-EDS spectra acquired from the [redacted] material are provided in Figure 30. The Cu signal found in the spectra may be due to the copper Omniprobe grid that the lift-out specimen was mounted to. The Pt and Ga signals in the EDS spectra are likely artifacts introduced by the FIB-based sample preparation process. The open structure of the [redacted] material makes it easy for re-deposited material to collect on the interior surfaces of the material during FIB milling. The EDS spectra for the filaments (suspected MWCNT bundles), as indicated by the red arrow in Figure 30a, only contain C and the artifact signals associated with FIB sample prep (Figure 30b). Nanoparticles of the type indicated by the blue arrow in Figure 30a appear bright in the STEM-HAADF image, indicating the particle is of higher Z than the surrounding filaments. These particles are rich in Fe (Figure 30c). The Fe-rich particles are found throughout the material and may be the catalyst particles that were used for the growth of the MWCNTs.

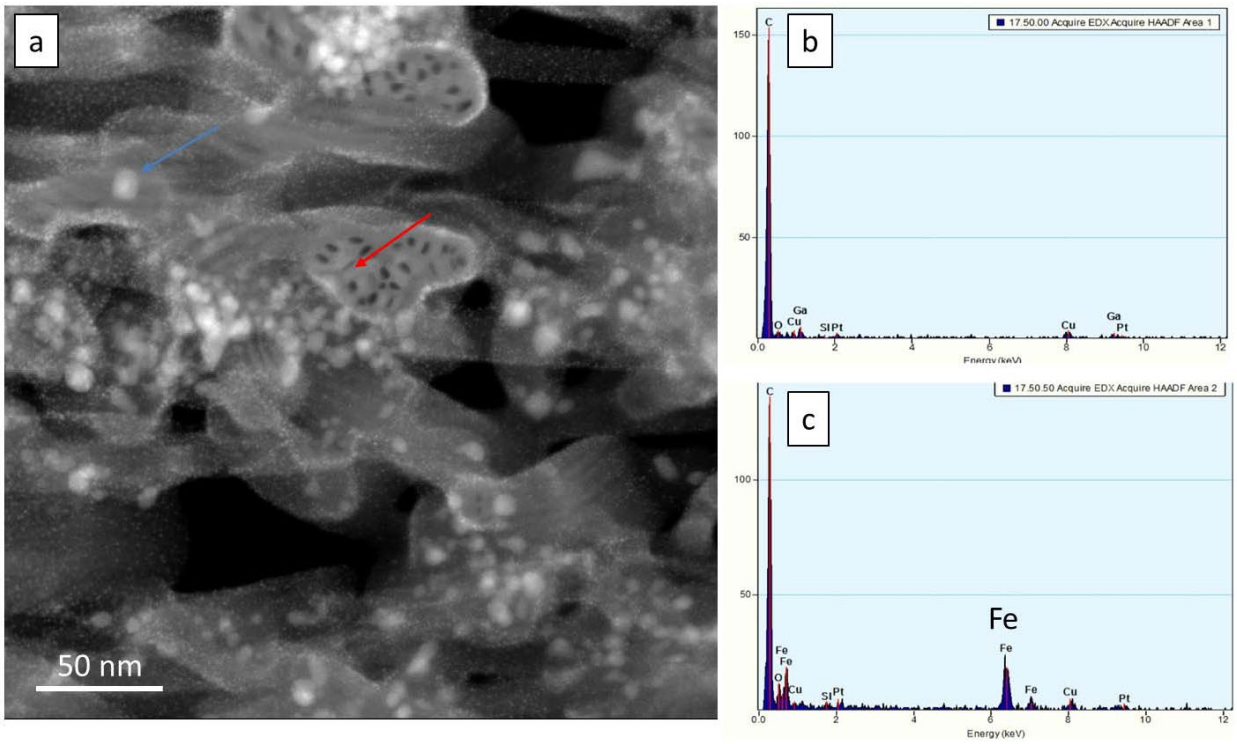

Figure 30: (a) STEM-HAADF image showing two locations probed by EDS in the [redacted] material. STEM-EDS spectra for (b) a filament (MWCNT bundle), as indicated by the red arrow in (a) and (c) an Fe-rich nanoparticle, as indicated by the blue arrow in (a).

5.2 Release Testing

5.2.1 Sample Preparation

Several product use cases were considered to determine the effective sample preparation approaches. Product care instructions for the ballistics panels recommended that the panels should be "wiped clean with a damp cloth and should not be machine washed, machine dried, bleached, dry cleaned or ironed". We suspect that it is unlikely that any nanomaterial that is contained within the sealed sleeve will be released as long as the recommended care instructions are adhered to since the outer sleeve edges are heat sealed rather than stitched and the sleeve material is supposed to be moisture resistant. Light microscopy and ATR-IR (attenuated total reflection - infrared spectroscopy) measurements (not shown here) confirmed that the outer sleeves are coated for moisture resistance and are made of nylon (for the [redacted] panels) and polyester (for the [redacted] and the [redacted] panels).

However, if the outer sleeve is compromised due to prolonged use, accidental tear, or misuse of the product, the MWCNT containing ballistic sheets could be exposed to the environment and the release of MWCNT is possible during direct mechanical stressing of the MWCNT containing components of the ballistic panels.

To test the likelihood that the outer sleeve will wear through as a result of normal use, a small piece of the nylon fabric was subjected to a repeated rubbing using a crockmeter attachment for the linear abrader. See Section 5.2.2 on Linear Abrader for more details about this test method. Figure 31a is the photo of the original nylon sleeve material taken from the [redacted] product. The water-resistant inner coating (shiny surface) and the dense weave characteristic of the nylon are both clearly visible. Figures 31b-d show the outer surface of the [redacted] nylon fabric and the [redacted] and [redacted] polyester fabrics after they have been subjected to 9000 cycles of crocking with an 800 g applied load. The load for the crocking was chosen based on the recommended load for the chemical coated fabric abrasion testing method adapted from the American Society for Testing and Materials (ASTM) test method D4157-10 [4]. Although the test area is clearly identifiable (marked with dashed rectangular regions in Figures 31b-d), the integrity of the material seemed to be unaffected by the crocking.

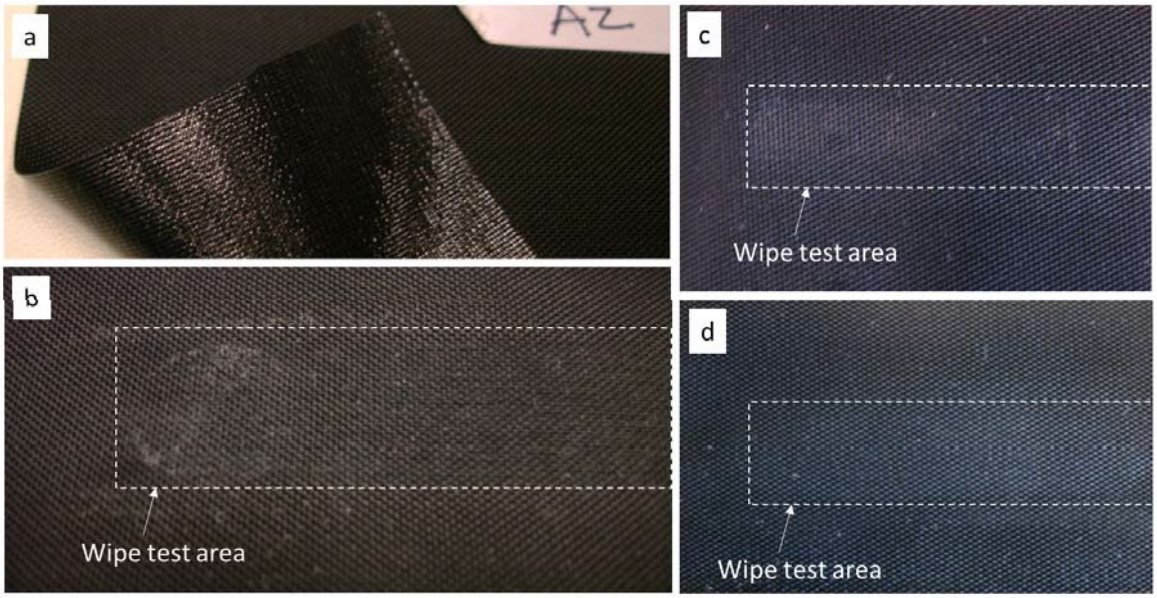

Figure 31: Photo of the [redacted] nylon sleeve material a) showing the water resistance coating (shiny side) on the inner surface and the b) outer surface after 9000 cycles with an 800 g loading. (c) [redacted] and (d) [redacted] polyester sleeve materials after 9000 cycles with an 800g loading.

The results of the crock test indicated that the outer sleeve of the ballistic panel is unlikely to wear out during the normal use of the product. However, if the outer sleeve of the ballistic panel is compromised accidentally (e.g., puncturing or tearing) or through misuse (e.g., cutting), containment of any nanoparticles cannot be expected. The situation in which the release of MWCNTs/nanoparticles is considered to be most likely is when the MWCNT containing component of the ballistic panel is subjected to direct mechanical stressing such as abrasion. Based on this premise, the direct mechanical abrasion testing of the MWCNT containing component of the armor insert was considered to be the worst-case scenario for MWCNT and

nanoparticle release. Therefore, the research efforts were focused on trying to develop analytical methods to detect and analyze release materials for this scenario.

As described above, MWCNTs were found to be present in the black coating that was applied to the [redacted] sheets in the [redacted] insert. MWCNTs containing sheets were also found sandwiched between two UHMWPE sheets in the [redacted] and the [redacted] inserts. For the abrasion experiments, 2" x 2" test coupons of these CNT containing materials were used. Multiple MWCNT containing sheets were stacked on top of each other to ensure that the abrasion head would not wear through the material during the test. From here on in, the coated [redacted] sheet from the [redacted] sample and the MWCNT sheets from the [redacted] and the [redacted] samples will be referred to as MWCNT sheets.

5.2.2 Linear Abrader

A Taber Linear Abraser Model 5750 abrader with T-slot universal table (Figure 32) was used for the wipe testing and the abrasion process. Abrasion stroke length, speed, applied force, and the number of cycles can be adjusted, and different tip configurations can be used to simulate a wide range of abrasive conditions such as low impact wiping or highly abrasive sanding or scratching.

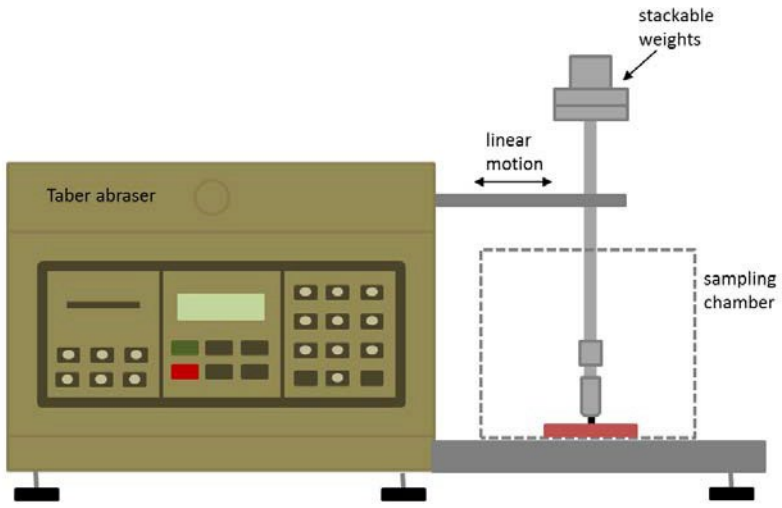

Figure 32: Schematic of Taber Abraser with universal stage and custom sampling chamber.

For the wipe testing, a crockmeter tip attachment was used (Figure 33). Crocking refers to a process where excess dye rubs off of one dry fabric onto another dry fabric. A crockmeter performs a repeated rubbing motion over a test sample using a weighted tip covered with a 'crocking' cloth that is designed to collect the dye (or release material in our case) from the test

samples. An AATCC[2] crockmeter test square was used to collect the material released from the MWCNT containing ballistic coupons during crocking.

Figure 33: Photo of the Taber crockmeter tip attachment covered with a crocking test cloth.

For the abrasion testing, an oval shaped double cut carbide burr was used as an abrading tip instead of the more commonly used abradant tip to minimize spurious particle generation. For the aerosol sampling of the released particles, a fully enclosed sampling chamber was designed around the sample stage and the abrader (Figure 34). The sample chamber was designed to include as little of the abrader mechanism as possible so as to: (1) minimize extraneous contributions such as particles from the abrader motor and other friction induced particles; and
(2) facilitate cleaning of the chambers and to prevent cross contamination between different sample runs.

[2] American Association of Textile Chemists and Colorists. The AATCC is a not-for-profit association that provides test method development, quality control materials, and professional networking for textile professionals

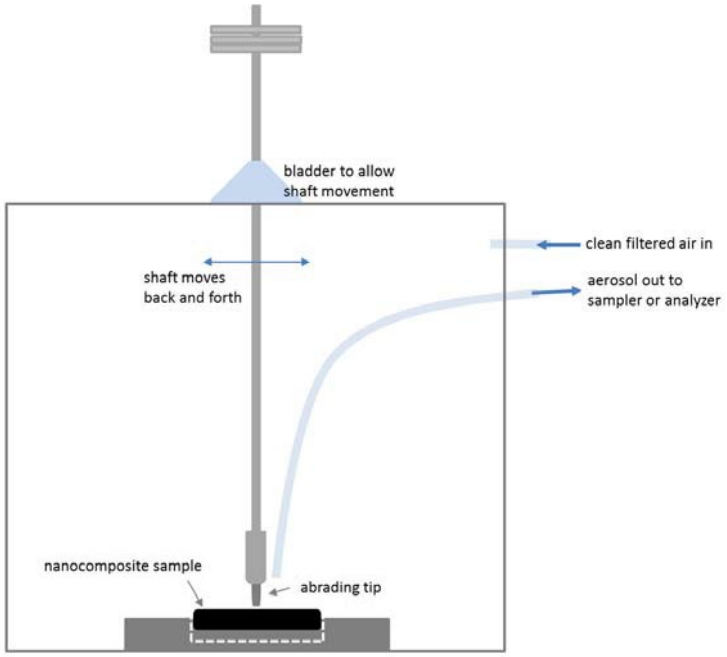

Figure 34: Schematic diagram of the sampling chamber.

Several different aerosol sampling intake port (aerosol inlet near the abrading tip) configurations were tested. It was found that sampling very close to the abrading surface was necessary to collect a sufficient number of particles, given both the low speed and low force used (60 cycles per min with 0.5 in stroke length and 600 g to 1100 g of load). A small intake nozzle diameter (1/8") was also necessary to generate a sufficient pressure drop for effective sampling. To further minimize contamination, clean HEPA filtered air was fed into the chamber at a flow rate near the sampling flow rate. Between each sampling run, the inside of the chamber is vacuumed using a HEPA filtered vacuum and allowed to stabilize for at least 30 minutes.

A modified version of Taber's Flexible Material Abrasion Kit specimen mount was used to hold the MWCNT sheets in place. Figure 35 shows the basic structure of the specimen mount. The test coupon (about 2" x 2") is placed over a cylinder and pinned in place by a rigid cover. The cover has a rectangular opening that exposes a section of the flexible textile specimen that has been stretched over the cylinder.

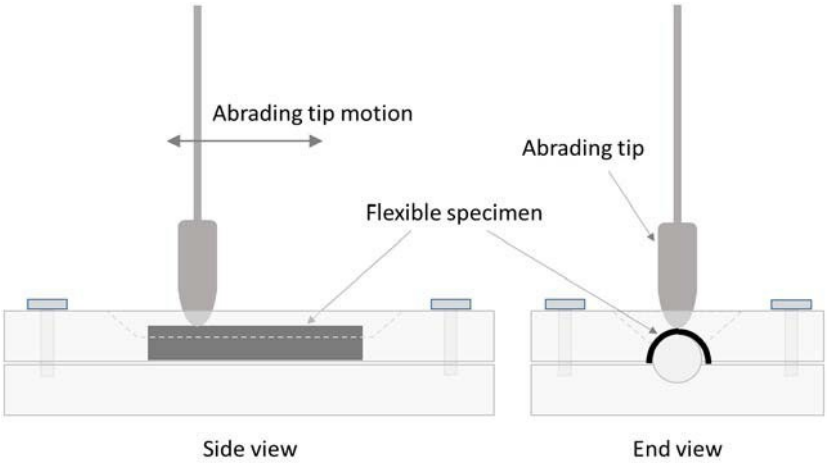

Figure 35: Schematic diagram of the custom flexible specimen mount used for the abrasion testing.

5.2.3 Wipe Testing

Wipe testing was performed on all three types of MWCNT sheets. Each test specimen was wrapped around a rectangular base piece and held in place using a small custom-made vise. The linear abrader settings used for the wipe tests were:

- 2" stroke length
- 60 cycles per minute
- 20 cycles or 500 cycles per test
- 500 g of weight (total weight 800 g including the shaft and the crockmeter tip)

Figure 36 shows the conditions of the wipe cloths and the MWCNT sheets after the wipe test. Figures 36a and 36b are the images of the test cloth taken from the [redacted] coupon after 500 wipe cycles. For the [redacted] coupon, there was no noticeable particle collection on the wipe cloth after twenty (20) wipe cycles. However, twenty (20) wipe cycles were sufficient to produce clear dark smudges on the wipe cloths taken from the [redacted] (Figures 36d-f) and the [redacted] (Figures 36g-i) coupons.

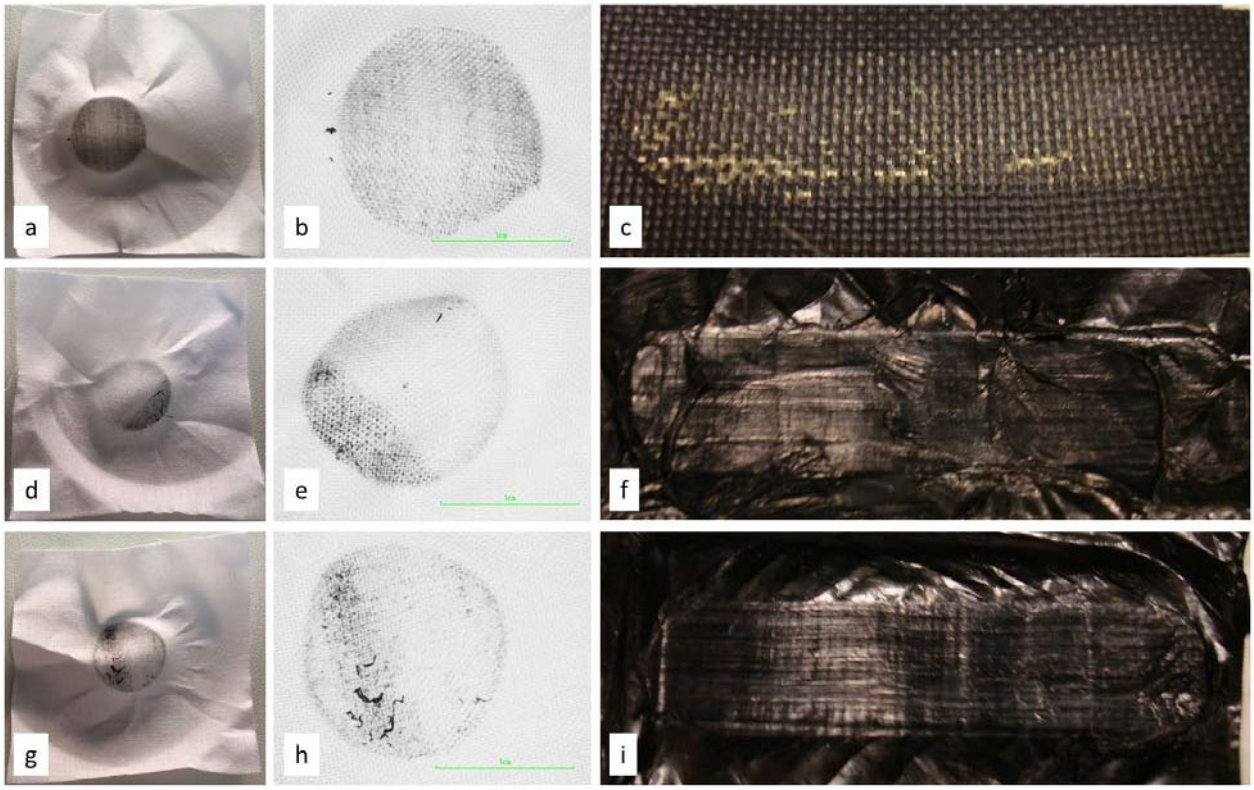

Figure 36: Images of the wipe cloths (columns 1 and 2) and the MWCNT sheets (column 3) after the wipe testing. (a-c) are from the [redacted] specimen after 500 wipe cycles, (d-f) are from the [redacted] specimen after 20 wipe cycles, and (g-i) are from the [redacted] specimen after 20 wipe cycles.

Two different methods were used to transfer the wear particles from the wipe cloths to SEM compatible substrates. For the first method, the particles were collected on ultra-smooth double-sided carbon tabs that were adhered to 12 mm Aluminum SEM stubs (Figure 37a) and then lightly pressed against the wear surfaces of the wipe cloths. These samples are will be referred to as SEM stub samples from here on in. A control sample was also made from a clean, unused wipe cloth. The SEM stub samples were lightly carbon coated to mitigate charging artifacts (<10 nm coating thickness) in the SEM during imaging.

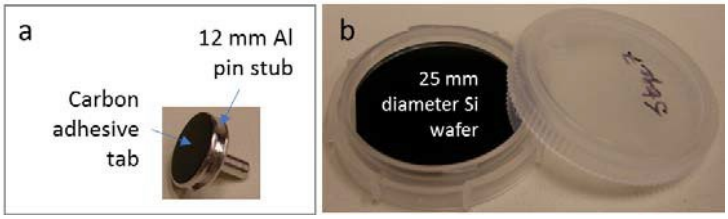

Figure 37: Photos of (a) an aluminum SEM stub with a double-sided carbon tab and (b) a 25 mm Si wafer used to collect wipe dust samples.

In the second method, loose particles from the wipe cloths were collected by dusting them onto 25 mm Si wafers (Figure 37b). These samples will be referred to as Si wafer dust samples

from here on in. To dust the particles onto a Si wafer, the Si wafer was first placed, polished side up, in a standard wafer container. The particle laden portion of the wipe cloth was then placed over the Si wafer, and the container lid was tightened down on the wipe cloth to keep the wipe cloth taut over the wafer. The cover of the container was then lightly tapped to loosen the particles from the wipe cloth. Figure 38 shows the schematic diagram illustrating the dusting procedure described here. The Si wafer dust samples were carbon coated prior to SEM analysis to minimize charging artifacts.

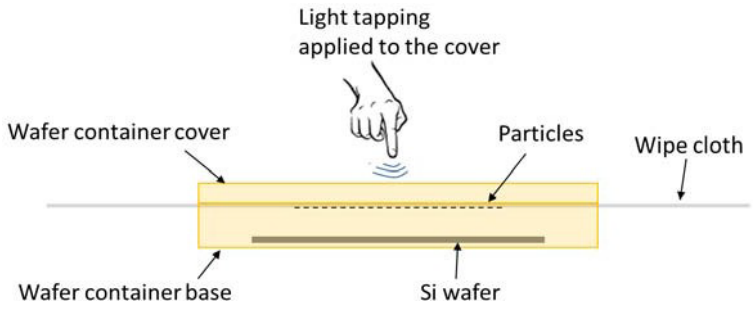

Figure 38: Diagram illustrating the dust collection approach

5.2.4 MOUDI Setup

Our earlier study had shown that the particle sampling efficiency can be a challenging problem for MWCNT nanocomposite abrasion experiments. It is not clear whether the poor sampling efficiency is due to the lack of aerosols generated during the abrasion process or if the loss of particles occurs through various other mechanisms, e.g. electrostatic loss. Particle loss by unintentional deposition at the sampling inlet or during transport could also be important factors in determining the overall sampling efficiency [5].

We used a micro-orifice uniform deposit impactor (MOUDI) to collect size selected samples at high flow rates to mitigate the low sampling efficiency problem due to transport loss. While the flow rates used for the earlier electrostatic precipitator and filter sampling devices ranged from 1.5 LPM to 3 LPM, the flow rate required for MOUDI sampling was much higher at 30 LPM. Additionally, since MOUDI produces size selected particle samples, some of the charging issues associated with highly polydisperse samples were eliminated. For example, higher stage samples (i.e. small particle diameter) collected on Si wafers can be imaged without additional charge mitigation measures, such as a conductive coating, thus preventing additional loss of imaging resolution through coating artifacts. Figure 39 shows the schematic of the MOUDI based abrasion particle sampling setup.

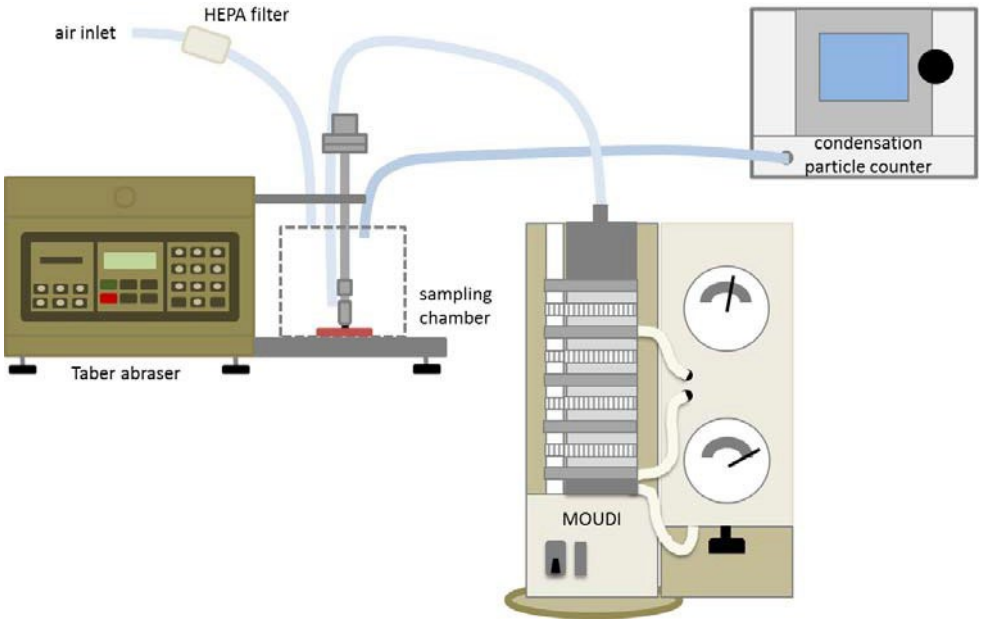

Figure 39: Schematic of the abrasion particle sampling station, MOUDI-CPC setup.

The MSP model 100 MOUDI, an inertial cascade impactor with multiple nozzles, was used. Detailed discussions of aerosol sampling using a cascade impactor can be found elsewhere [6, 7]. The MOUDI consists of a series of impaction plates where particles of specific size ranges can be collected based on the nozzle sizes. See Appendix 4 for the list of different impaction stages and the corresponding nozzle sizes. The MOUDI can be used in a rotating or non- rotating mode. If used in a rotating mode, the collected particles are distributed more evenly on the sampling substrate. The condensation particle counter (CPC) was mainly used to monitor the particle count in the abrading chamber to ensure that a proper steady state condition was reached prior to the start of each abrasion test.

Initial tests of MOUDI sampling using traditional Al foil substrates showed very poor collection efficiency. Track-etched polycarbonate membrane filters, although more effective in collecting particles than Al foils, were difficult to handle without disturbing the collection surface and also required application of a conductive coating to mitigate charging. To avoid these problems, the MOUDI impaction plates were customized, as shown in Figure 40, to accommodate 1” Si wafers sampling substrates in place of the traditional Al foil or membrane filter substrates.

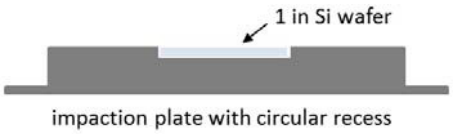

Figure 40: Custom modified impaction plate with 1” circular recess to accommodate a Si wafer.

Figure 41 shows the stage dependent particle distribution patterns observed on the MOUDI sample substrates. These particles were collected in a non-rotating configuration. In a non-rotating sampling configuration, each stage produces differently sized honeycomb-like particle distribution patterns where the size of the cells depend on the number of nozzles on the stage. As the stage number increases, the typical 'cell' size decreases. For a given MOUDI stage sample, an area larger than a typical cell should be analyzed to ensure that a representative population of particles is examined. In a rotating mode, the particles on the MOUDI substrate form a concentric ring pattern and are more uniformly distributed throughout the sample substrate.

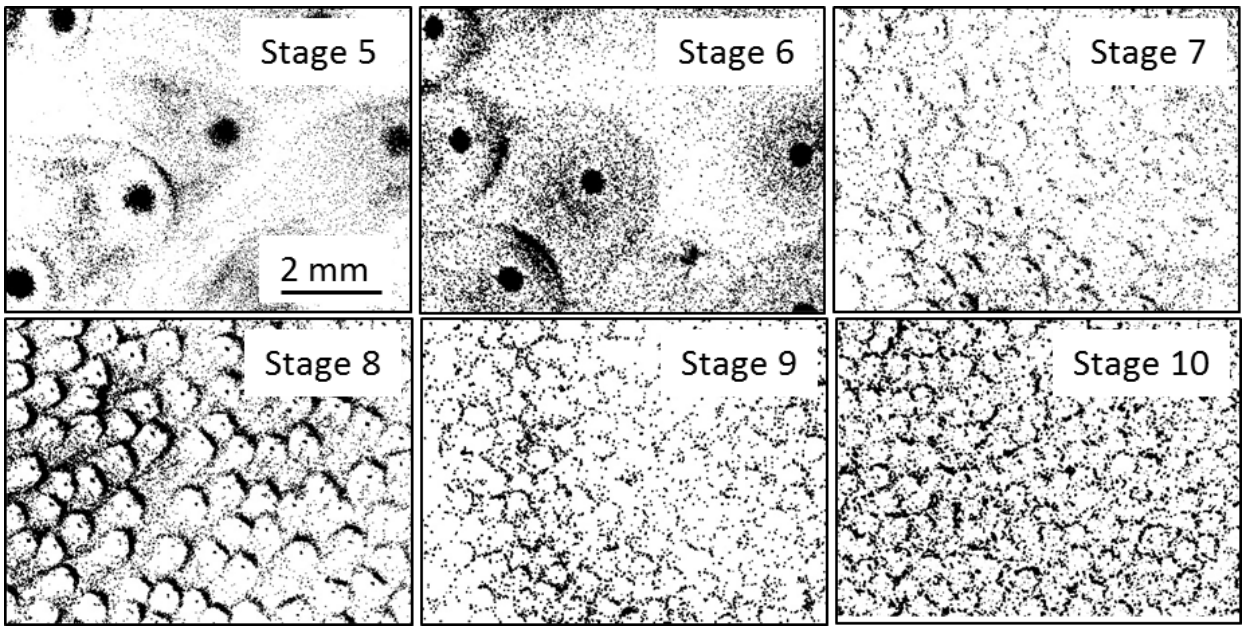

Figure 41: Particle distribution patterns on MOUDI sample substrates at different stages. The patterns were collected in a non-rotating configuration to show the sizes of typical 'cells' on each stage. All images are at the same scale.

Abrasion testing was performed on all three types of MWCNT sheets. Each test coupon was mounted on the flexible sample mount that was described in the Section 5.2.2. To ensure that the MWCNT sheet specimen was not completely abraded through during a given run, several layers of the MWCNT sheets were stacked together for each abrasion test. The linear abrader settings used for the abrasion tests were:

- 0.5" stroke length
- 60 cycles per minute
- 1500 cycles to 5000 cycles per test
- 250 g of weight (total weight 600 g including the shaft and the abrading tip)

Multiple abrasion tests were performed on each type of MWCNT sheet. Control sampling runs were also performed during which the MWCNT sheets were placed in the specimen mount but no abrasion was carried out. In addition to the active sampling of airborne particles by the Si wafer substrates in the MOUDI, passive sampling was also performed by placing Si wafers and TEM grids near the abrading area as shown in Figure 42.

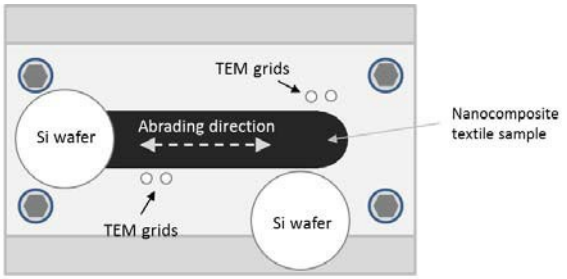

Figure 42: Diagram of the flexible specimen mount showing the locations of the Si wafers and the TEM grids used for passive sampling during the abrasion process.

5.3 SEM & TEM Imaging

SEM analysis of the release particles was performed using a FEI Helios NanoLab 650 and a FEI Helios NanoLab 600 FIB/SEM instruments. All SEM images were acquired with SEs, unless otherwise noted, or the instrument was operating in transmission mode. TEM analysis was performed using a FEI Titan 80-300 S/TEM instrument.

5.3.1 Automated SEM Imaging and Particle Analysis

FEI's custom large area imaging application, MAPS, was used to investigate large regions on each SEM stub sample and Si wafer sample. A typical MAPS imaging session on a Si wafer sample (including the samples from the MOUDI stages) consisted of a low resolution survey scan with a 30 x 30 frame image array at 124 μm horizontal field of view per frame and 40 nm pixel dimension (total coverage of approx. 3 mm x 2 mm) and a high resolution scan with a 20 x 20 frame image array with 12.4 μm horizontal field of view per frame and 4 nm pixel dimension (total coverage of approx. 224 μm x 149 μm). Figure 43 shows a typical MAPS imaging run overlaid on a Si wafer. The low-resolution survey image array provides the overall particle distribution pattern for the sample. However, many of the nanometer sized particles are not detected at this resolution. The higher resolution image array can provide information about the nanoparticles present. However, because the analysis area at this resolution is quite small, image arrays should be collected from multiple locations to ensure an accurate representative analysis of the fine particles is obtained. Unfortunately, each of these MAPS runs can take 4 to 6 hours and generate 12 GB to 16 GB of data, making a thorough analysis of each MOUDI substrate sample not practical in terms of instrument time, analysis effort, and data handling capacity. For our study, we performed one survey run and one high resolution run on each

MOUDI substrate to assess the overall particle size distribution and abundance at each MOUDI stage.

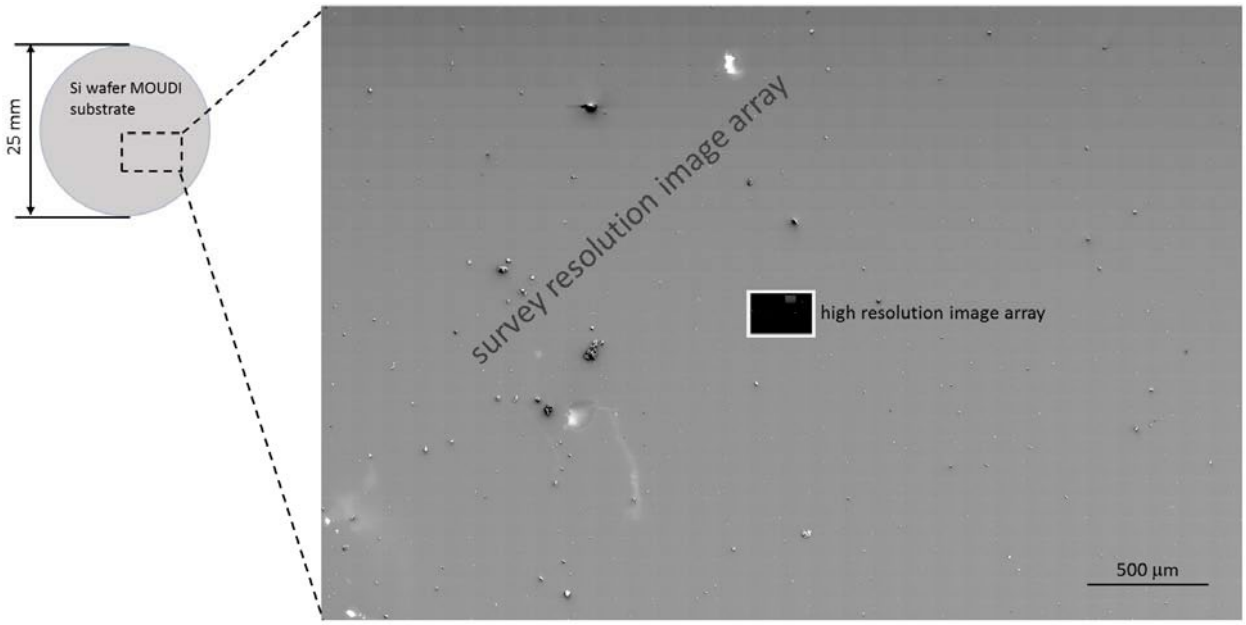

Figure 43: Typical MAPS run overview and relative analysis area overlaid on a 1" Si wafer.

A similar approach was employed for analyzing the SEM stub samples from the wipe testing. A typical MAPS imaging session of a SEM stub sample consisted of a low resolution survey scan with a 10 x 10 frame image array with 426 µm horizontal field of view per frame and 140 nm pixel dimension (total coverage of approx. 3.8 mm x 2.5 mm) and a high resolution scan with a 20 x 20 frame image array with 12.4 µm horizontal field of view per frame and 4 nm pixel dimension (total coverage of approx. 224 µm x 149 µm).

Typical MAPS run parameters were:

- 2 keV beam energy and 100 pA beam current
- Everhardt Thornley detector (ETD) for low resolution survey scans and Through-the-Lens detector (TLD) in immersion mode for high resolution scans
- 10 % frame overlap
- 3072 x 2048-pixel resolution
- 1 µs pixel dwell and single scan per frame
- Three-point interpolation for image focus

Image stacks from each MAPS run were quickly scanned for the locations of interesting particles or for regions of the sample that should be examined more carefully. Additional imaging on regions outside of the original MAPS run area was also performed as needed.

The image stacks from the Si wafers were processed using FIJI [8] to determine the particle size distributions. The basic image processing steps performed for each image stack were:

1. Smoothing operation
2. Edge detection
3. Thresholding to generate binary masks for particles
4. Close path and fill holes
5. Dilate
6. Close path and fill holes
7. Analyze particles, limiting to particles that are larger than 10 pixels.

5.3.2 Wipe Sample Imaging

As described in Section 5.2.3, two different methods were used prepare the wipe dust samples for SEM imaging: (1) SEM stub sampling, which used double sided carbon tabs to collect particles from the wipe cloths; and (2) Si wafer dust sampling in which the loose particles from the wipe cloth are transferred to 25 mm Si wafers.

5.3.2.1 SEM Stub Samples

Figure 44 shows the overview images from the survey scan and high-resolution scan of the [redacted] wipe test SEM stub sample. The larger image is a montage of the low-resolution survey scan images, and the smaller image is the montage of the high-resolution scan images from the region marked with a light rectangle. The prominent irregular line patterns are features of the carbon tab surface. Although difficult to see in the overview images shown in Figure 44, numerous micrometer-sized and nanometer-sized particles were found in the survey scan and the high-resolution images.

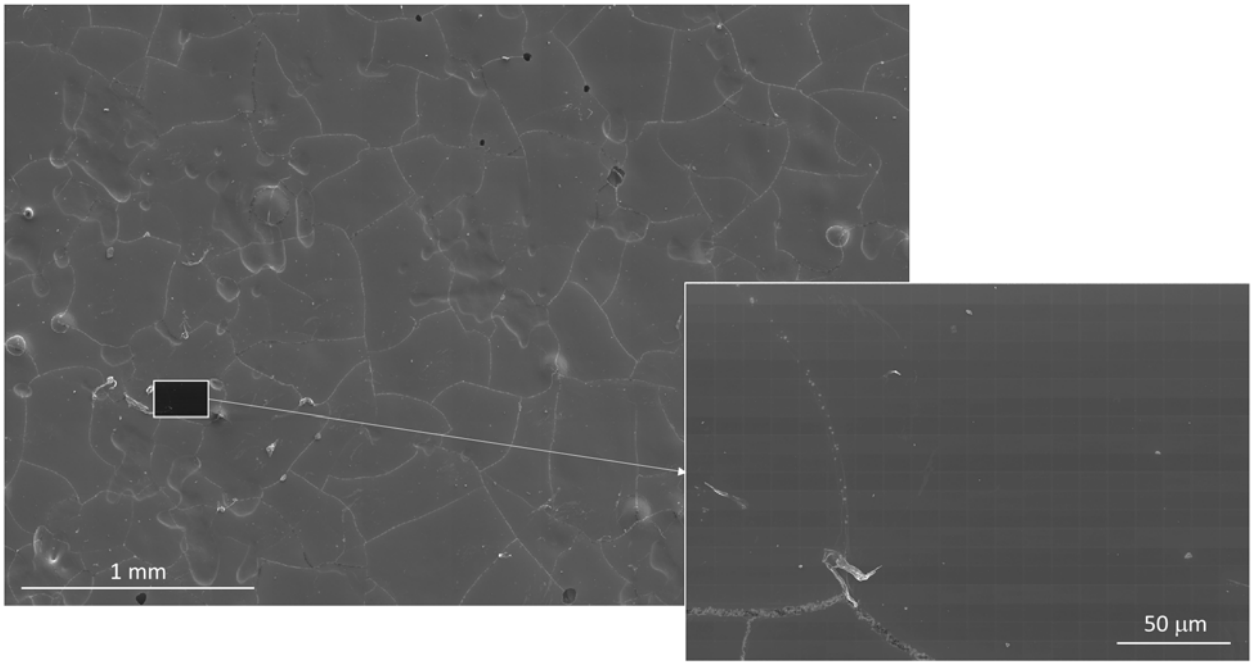

Figure 44: Overview images of the MAPS scans of the [redacted] wipe SEM stub sample.

Figure 45 is an example of a typical particle distribution found on the survey scan images. Here, one image from the survey scan image stack is paired with its corresponding processed image that contains the outlines of the particles that were found on the original image. The image shows the presence of numerous fine particles.

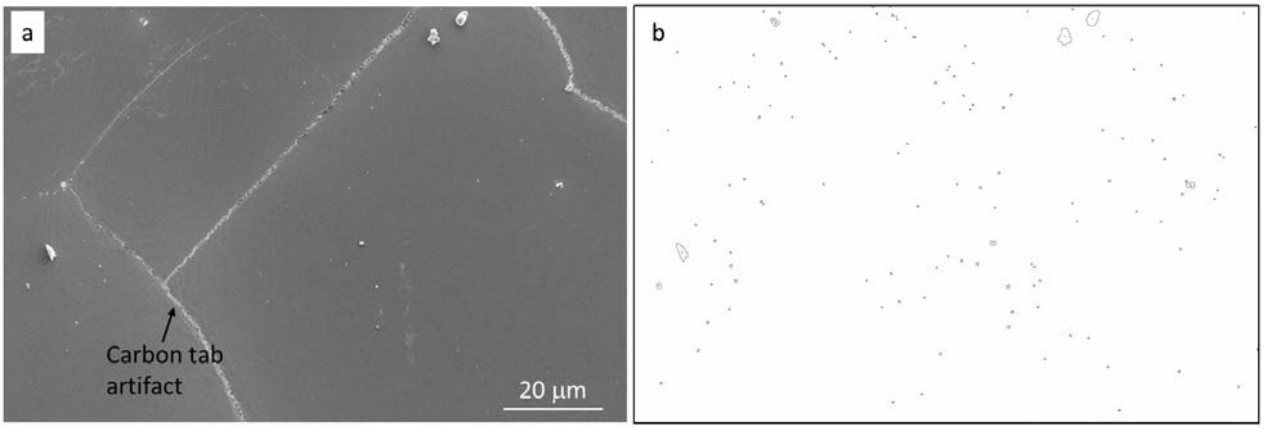

Figure 45: An image from a survey scan (a) and the outlines of the particles found on the image (b).

Figure 46 shows some of the particles found in the sample. The shapes and sizes of the particles vary greatly. However, none of the particle morphologies were consistent with bare MWCNTs or agglomerates of MWCNTs with one exception. Figure 46e shows a partially buried particle that show bright punctate features that are consistent with exposed ends of fibers.
Several similarly buried particles were found.

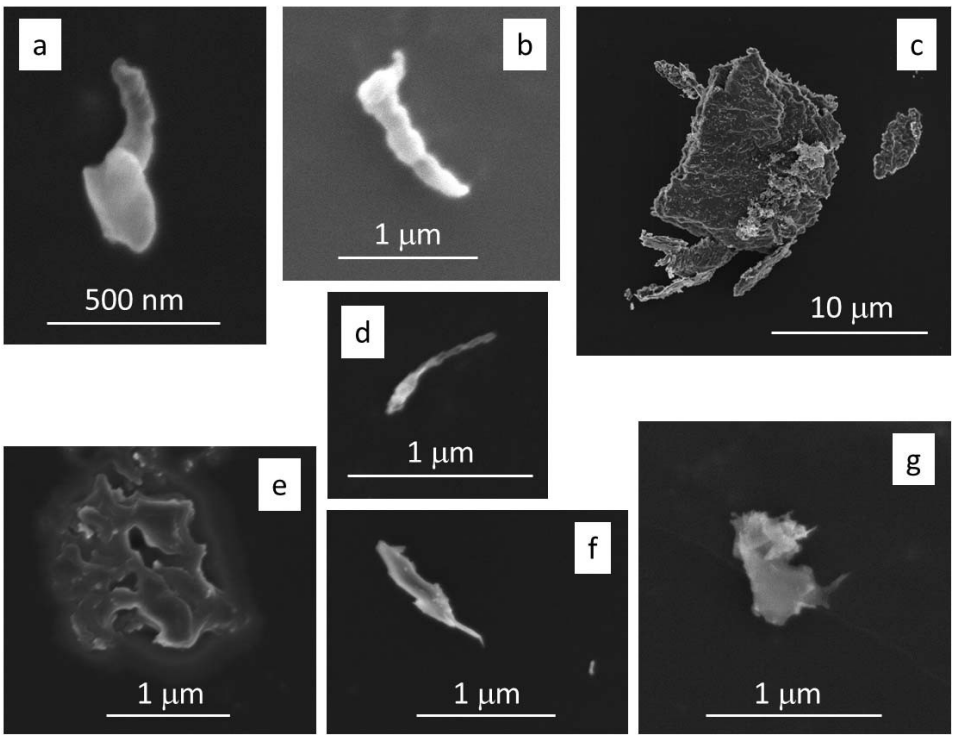

Figure 46: Example particles found on the SEM stub samples from the [redacted] II wipe test.

Figure 47 shows the overview images from the MAPS scans performed on the SEM stub sample from the [redacted] wipe test. Compared to the [redacted], there were many more large particles and many of these particles seemed to be fibrous in nature. The high-resolution overview image (inset of Figure 47) also shows many more particles when compared to the high-resolution scan images from the [redacted] sample (Figure 44).

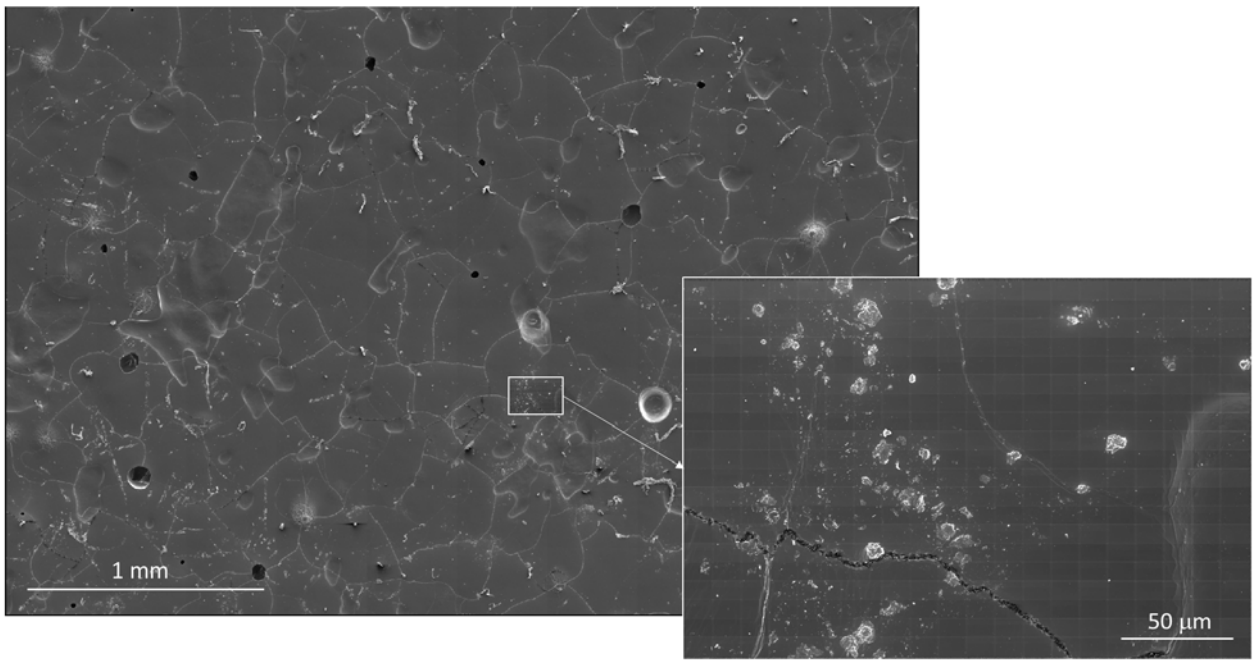

Figure 47: Overview images of the MAPS scans of the [redacted] wipe sample.

A closer examination of the particles found on the [redacted] wipe test samples shows the presence of many nanoscale fibers (Figure 48). These fibers were found in clusters or were attached to larger particles. Some fibers seem to be protruding from a larger particle that is embedded in the adhesive materials of the carbon tab (Figure 48c, e). Some of these embedded particles showed similar morphology as the buried particle shown in Figure 46e.
Based on the fact that the [redacted] and the [redacted] MWCNT sheets have very similar structures, we expected to find similar results for both products. The MAPS scans of the [redacted] samples showed comparable levels of particle abundance and a similar particle morphology. Many nanoscale fibers, some exposed and some embedded in the adhesive material, similar to those found in the [redacted] and the [redacted] samples, were also found in the [redacted] wipe samples (Figure 49). We also found several larger fiber fragments (Figure 49a) in the [redacted] wipe samples that looked similar to the loose filaments analyzed from the [redacted] and [redacted] MWCNT sheets (e.g. Figure 17 to Figure 20).

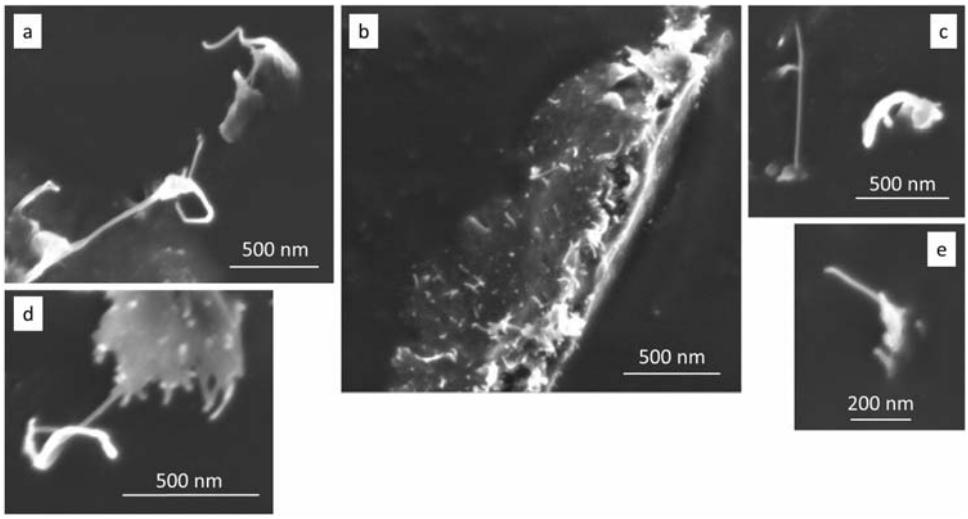

Figure 48: High magnification images of the nanoscale fibers found on the [redacted] wipe sample.

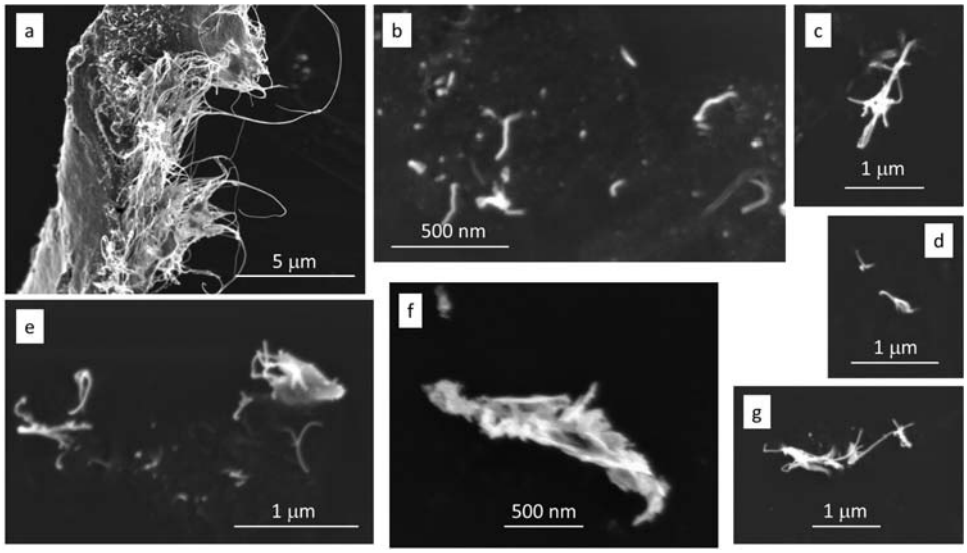

Figure 49: High magnification images of the nanoscale fibers found on the [redacted] wipe sample.

Figure 50 shows images of the nanoscale fibers and particles found on the control wipe sample. The control wipe sample was made by sampling the surface of a clean, unused wipe cloth with a double-sided carbon adhesive tab mounted on an SEM stub. The nanoscale fibers found on the control sample were very similar to those found on the [redacted] and the [redacted] samples, although the areas imaged on [redacted] and the [redacted] samples had a larger number of small fibrous particles than the control sample. If we accept that the nanoscale fibers found on the control wipe sample were from the wipe cloth itself, then it was possible that the small fibrous particles on the [redacted] and [redacted] SEM stub samples were also due to the wipe cloth material. The repeated rubbing of the wipe cloth material during the wipe test may have generated wear particles from the wipe test cloth that

were subsequently collected on the SEM stub sample. Alternatively, the variation in the number for particles observed for the different specimens could be due to a non-uniform distribution of the particles on the surface of the specimen, i.e. the images were collected from regions that were more or less sparsely populated with particles.

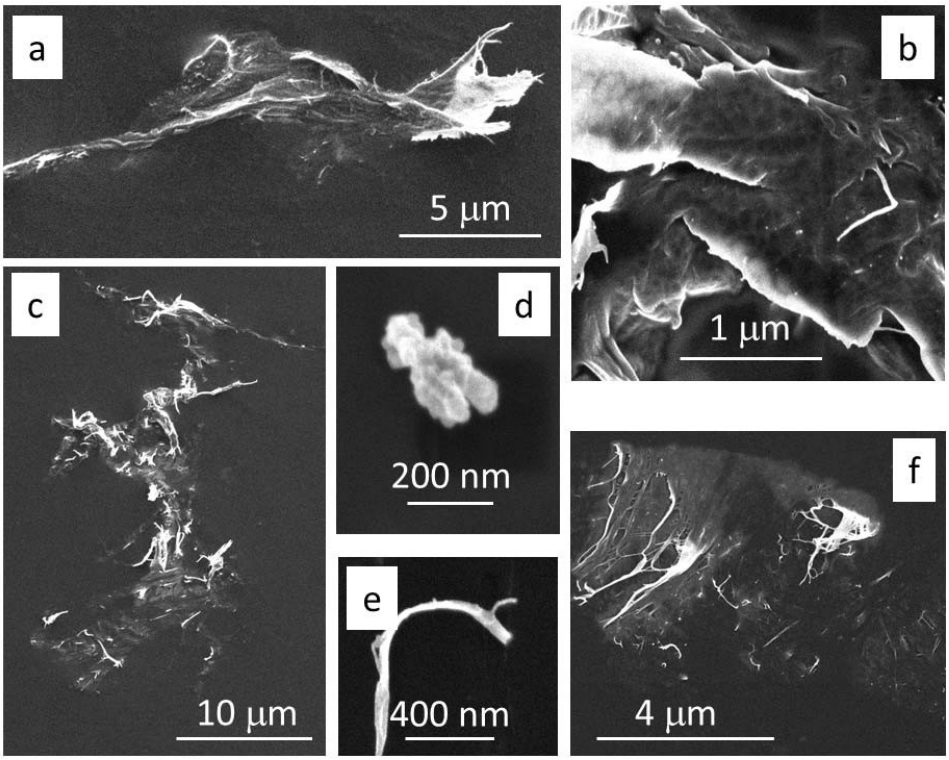

Figure 50: High magnification images of the nanoscale fibers and particles found on the control wipe sample.

Based on the control sample images, we concluded that most of the nanoscale fibers detected on the SEM stub samples were probably from the wipe cloths themselves. However, we suspect that some of the fiber fragments found on the wipe samples are from the MWCNT sheets. Fibers from the wipe cloth and the [redacted] MWCNT sheets are compared in Figure 51. From Figure 51, it is clear that the both types of fibers are made up of bundles of nanoscale fibers. Nanoscale fibrous components of the wipe cloth and the MWCNT sheets are roughly the same size, further complicating the analysis. The only difference between the two types of fiber seems to be the alignment of the nanofibers. In the cloth fiber sample, nanofibers are relatively well aligned while the nanofibers in the MWCNT sheet appear to be tangled.

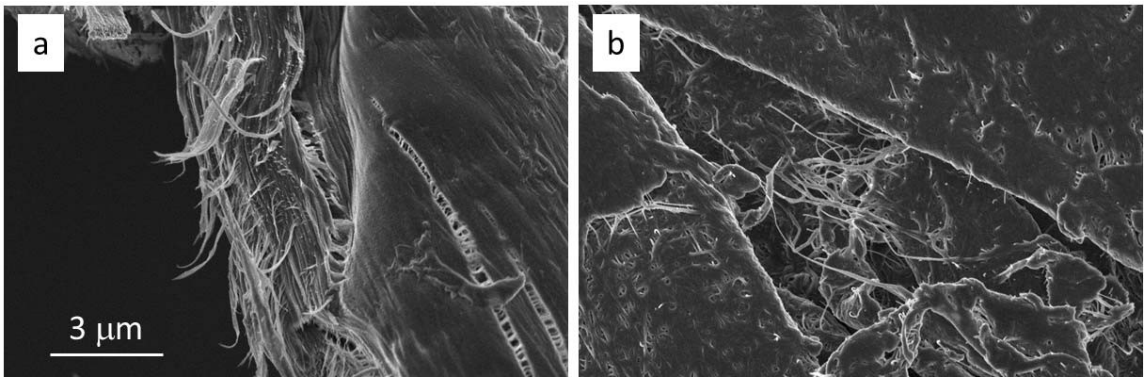

Figure 51: Comparison of a) a wipe cloth fiber and b) a loose filament from the [redacted] MWCNT sheet. Both images are at the same scale.

5.3.2.2 Si Wafer Dust Samples

MAPS automated SEM imaging was performed on the Si wafer dust samples that were collected from all three ballistic materials. As described earlier, a set of low-resolution survey scan images were collected to evaluate the overall particle distribution, particle size ranges, and particle abundance. A high-resolution scan was then performed, on a much smaller region, to facilitate the detection of nanoscale particles. Figures 52 and 53 summarize the particle data generated from these low resolution (total of 900 images per sample) and high resolution (total of 400 images per sample) MAPS scans.

Although it is difficult to compare particle size distribution data between the samples, the particle size distribution plots generated from the low-resolution images (Figure 52) all follow a similar trend and indicate that most of the particles found in these wipe test samples were less than 700 nm in area equivalent diameter. On average, the particles from the [redacted] sample were smaller than the particles from the [redacted] and the [redacted] samples. In all cases, less than 10 % of the particles detected were greater than 1 µm in area equivalent diameter (data not shown).

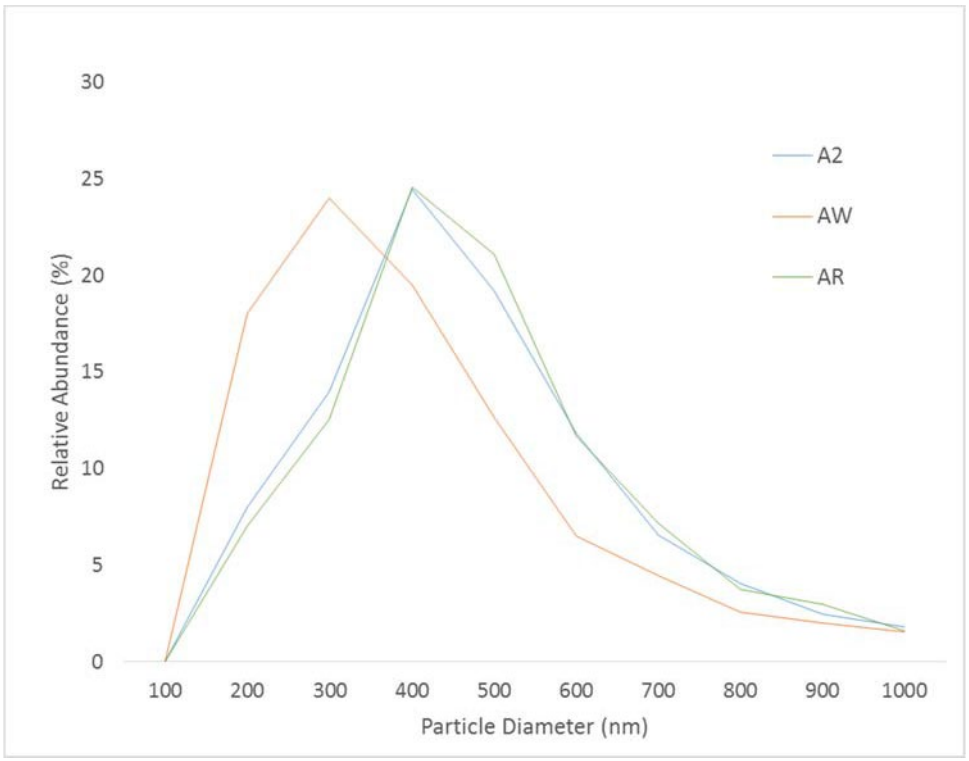

Figure 52: Comparison of the particle size distributions from the [redacted] (A2), [redacted] (AW), and [redacted] (AR) wipe tests. The particle data was generated from the survey scan (low resolution) images of the Si wafer dust samples. The particle diameter is the area equivalent diameter. Particles having a size <10 pixels were rejected during imaging processing, which corresponded to a particle diameter of approx. 100 nm.

Figure 53 shows the particle size distribution data from the high-resolution MAPS scan images of the three samples. At this magnification, the same general trend is found for all three samples, i.e. the relative abundance of the particles increases as the size of the particles decreases. While the relative abundance of particles within a given size range is similar between samples, the [redacted] images had a significantly fewer number of particles than either the [redacted] or the [redacted] images. One explanation for this could be that the particle distribution over the Si wafer was not uniform and the [redacted] high resolution data set was collected over a sparsely populated region of the sample.

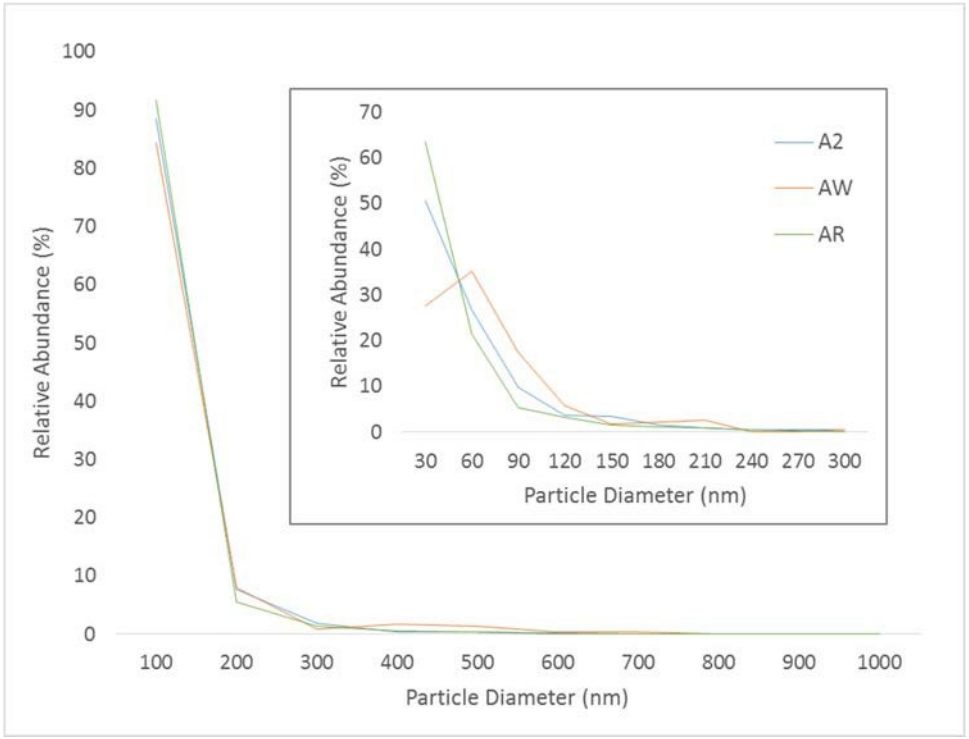

Figure 53: Comparison of the particle size distributions from the [redacted] (A2), [redacted] (AW), and [redacted] (AR) wipe tests. The particle data was generated from the high-resolution scan images of the Si wafer dust samples. The particle diameter is the area equivalent diameter, and the data has been binned at a 100 nm increment (inset shows same data binned at a 30 nm increment). Particles having a size <10 pixels were rejected during imaging processing, which corresponded to a particle diameter of approx. 10 nm.

One of the parameters calculated during the image processing-based particle analysis was the aspect ratio of the particles. In general, the majority of the particles had an aspect ratio of 5 or less, although a few particles had an aspect ratio greater than 10. Many of the high aspect ratio particles found during the survey scan were relatively large micrometer-sized particles. Several high aspect ratio particles from the high-resolution scans showed MWCNT like features. Figure 54 shows particles that are typical of the types found in the [redacted] wipe dust samples. The particle sizes ranged from <200 nm to several micrometers, and most particles seem to be an agglomerate of multiple particles. However, of the particles that were inspected, none were found to contain exposed MWCNTs.

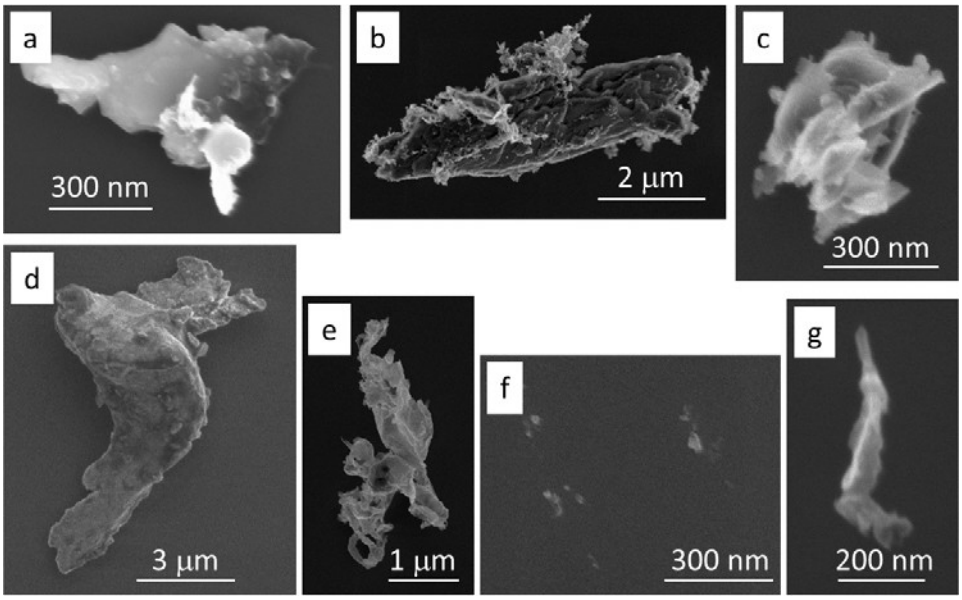

Figure 54: Examples of particles found in the [redacted] I wipe dust sample.

Figures 55 and 56 show particles representative of those found on the [redacted] and the [redacted] dust samples, respectively. In both samples, there were areas with a locally high density of particles (Figures 55a & 56f). In many cases, nanoscale rod shaped particles were found in these clusters of particles. However, these rod-shaped particles were very difficult to image and were usually not detected by the automated image analysis routine.

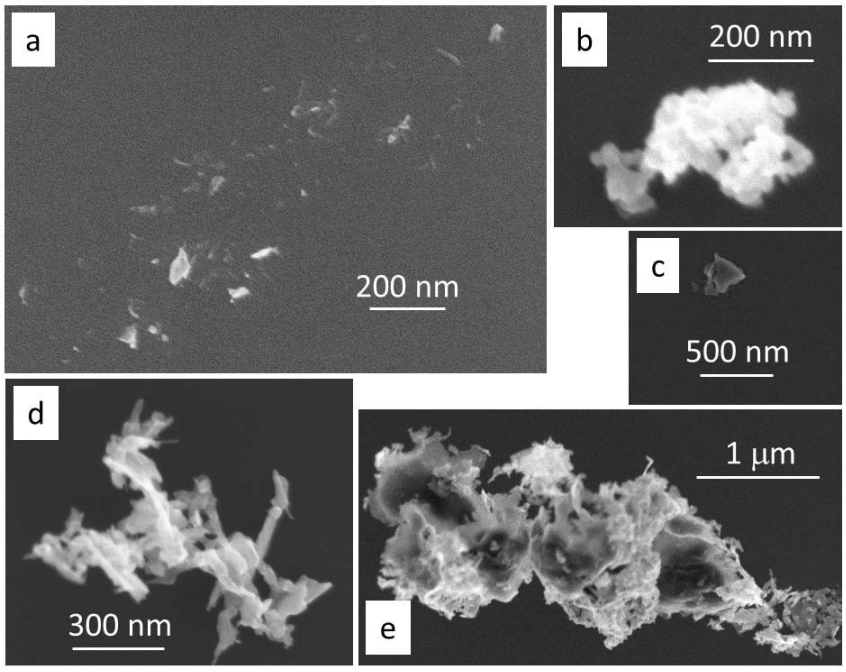

Figure 55: Examples of particles found in the [redacted] wipe dust sample.

Manual high-resolution scanning (hunt-and-peck approach) of the wipe dust samples was also performed. During these manual imaging sessions, several MWCNT-like particles were found in the [redacted] sample. Figure 56d shows an approx. 300 nm long tube-like structure. Based on our prior experience in imaging MWCNTs, the contrast level and the behavior of the particle under the beam was consistent with a MWCNT. See Appendix 5 for the images of several MWCNTs from an earlier project. Figure 56g shows what appears to be an agglomerate of MWCNTs and small polymer flakes. A high magnification image of one of the rod like particles found in Figure 56f (& inset) shows what may be a dense particle in a short tube.

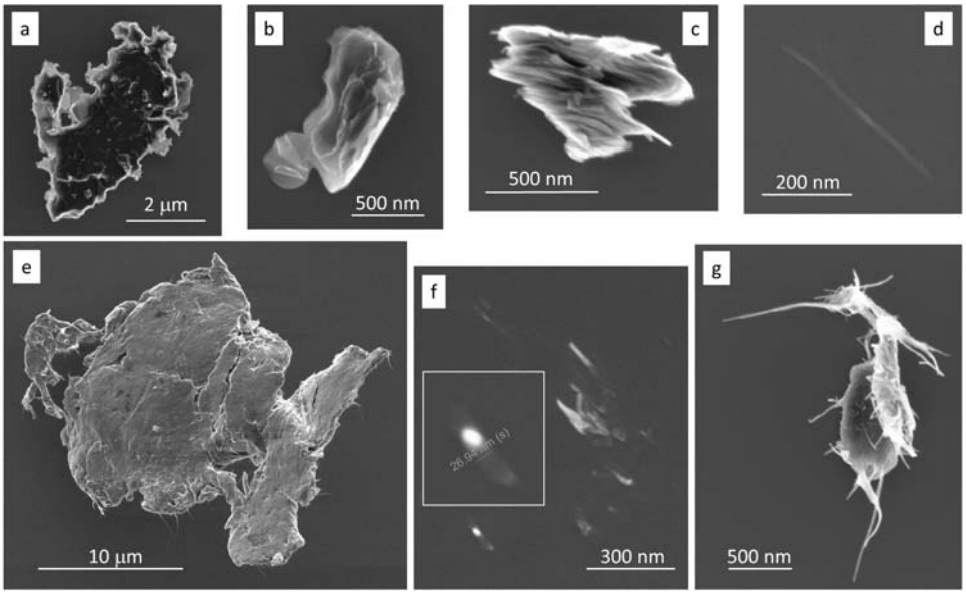

Figure 56: Examples of particles found in the [redacted] wipe dust sample.

It should be noted that the wipe dust samples did not have any fibrous particles frequently seen in the SEM stub samples (e.g. Figure 49a). We suspect that this is due to the fact that the large fibrous wear particles from the wipe test cloth remained partially entangled in the wipe cloth fabric and were less likely to be released during the dust sampling process compared to the adhesive sampling method used for the SEM stub samples.

Although it was possible to find few individual MWCNTs and small agglomerates of MWCNTs through manual high-resolution scans of the sample, the automated imaging and processing routine was not very effective in finding and identifying the MWCNTs. As shown in Figures 52 and 53, the particle size distributions reported for all three MWCNT sheet materials were quite similar. Given the similar construction of the [redacted] and [redacted] products, we expected these two products to perform similarly under testing. However, there was a significant difference in the MWCNT incorporation methods used in the [redacted] product versus the [redacted] products. Since we had no reason to expect that all three MWCNT sheet materials would yield similar particle size distribution results, this may

indicate that the test or sampling method is influencing the size distribution measured for the released wear particles. Further, for the size distributions that were determined from the high-resolution images, the sharp increase observed in the relative abundance of particles as the size of the particles decreases (Figure 53) may indicate that the true distribution has been masked by an overwhelming number of artifact counts in these bins from image processing.

5.3.3 MOUDI Sample and Passive Collection Sample Imaging

Release particle samples were collected onto Si wafers, with the MOUDI and without (passive collection), and then analyzed using the automated MAPS imaging routine that was described earlier. The manual hunt-and-peck approach was also employed to look for additional particles and to search the analysis area at resolutions greater than what was used for the automated imaging runs.

Figures 57 and 58 show the particle size distributions generated from the low resolution (total of 900 images per sample) and high resolution (total of 400 images per sample) MAPS scans of the MOUDI stage samples acquired from an [redacted] abrasion test. Table 1 lists the nominal particle cut size for the MOUDI stages used for the abrasion test. Each MOUDI stage is supposed to collect particles only within a specific size range, although there always will be a distribution of particle sizes in each stage.

Stage Number	Particle Cut Size (μm)
5	1.0
6	0.56
7	0.32
8	0.18
9	0.10
10	0.05

Table 1: Nominal particle cut size of the MOUDI stages.

Based on the nominal particle cut size of the MOUDI stages, we expected to see particle size distribution plots to show one major peak per stage with gradual shift of the peak position from 1 μm to ~50 nm as we go from stage 5 to stage 10 samples. However, the low-resolution MAPS scan results from the different MOUDI stages did not show the expected particle size distribution pattern. The particle size distribution plots from the stages 5, 6, 8, and 9 exhibited bi-modal distributions with a strong peak at 200 nm, representing particles with area equivalent diameter in the range of 100 nm and 200 nm, and a weaker peak around 400 nm to 500 nm region, representing particles with area equivalent diameter in the range of 300 nm and 500 nm. Stages 7 and 10 only show one large peak at 200 nm. The particle size distribution plot of the passive collection sample showed one broad peak centering around 400 nm with a small shoulder at 200 nm.

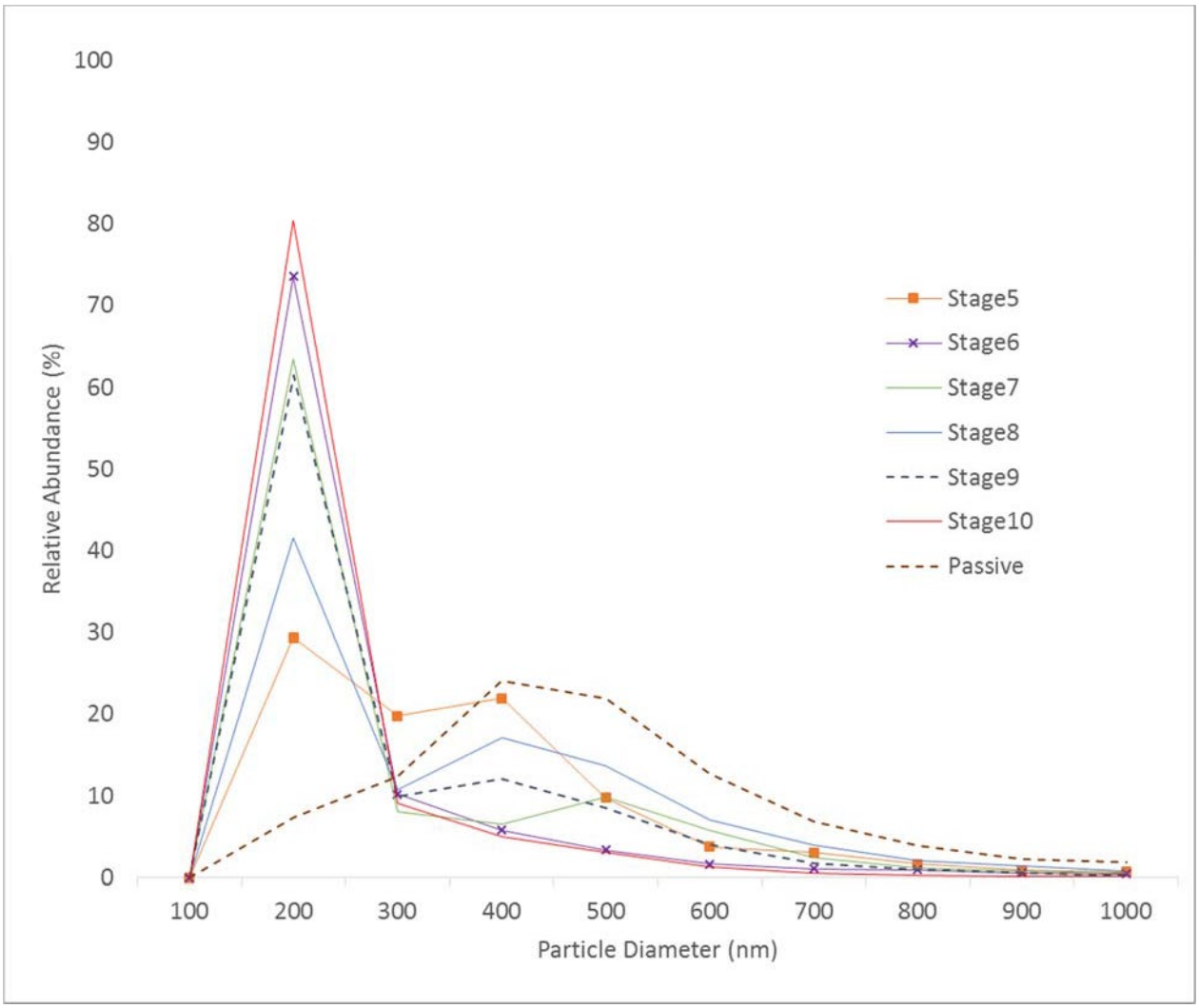

Figure 57: Comparison of particle size distributions collected at different MOUDI stages during an [redacted] abrasion test. The particle data was generated from the survey scan (low resolution) images of the MOUDI samples. The particle diameter is the area equivalent diameter, and the data has been binned at a 100 nm. Particles having a size <10 pixels were rejected during imaging processing, which corresponds to a particle diameter of approx. 100 nm.

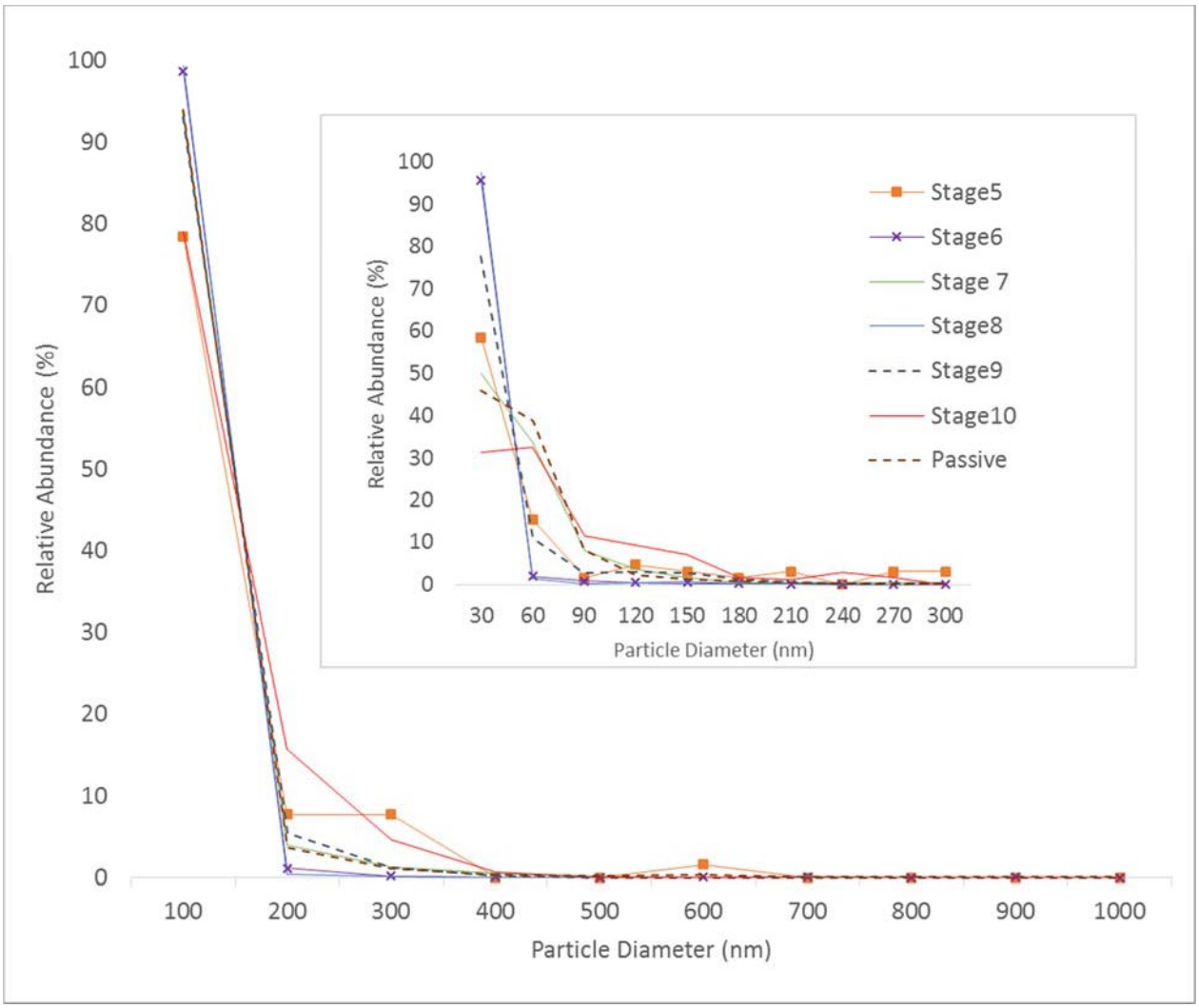

Figure 58: Comparison of particle size distribution collected at different MOUDI stages during an [redacted] abrasion test. The particle data was generated from the high-resolution scan images of the MOUDI samples. The particle diameter is the area equivalent diameter, and the data has been binned at a 100 nm increment (inset shows same data binned at a 30 nm increment). Particles having a size <10 pixels were rejected during imaging processing, which corresponds to a particle diameter of approx. 10 nm.

The particle size distribution plots from the high-resolution scan images of the MOUDI stage samples did not follow the expected trend either. Similar to the high-resolution wipe dust particle size distribution results (Figure 53), the relative abundance of particles increased sharply as the size of the particle decreased, with most of the particles having area equivalent diameter less the 300 nm, for all stages and the passive collection samples.

In general, most particles on the MOUDI samples were a few hundred nanometers or less in area equivalent diameter while the passive collection sample had a number of particles that were micrometers and larger. The MOUDI samples were imaged without any additional coating. However, the passive collection samples were lightly carbon coated to mitigate heavy

charging effects in larger particles. Blank Si wafers were carbon coated and examined to make sure that the carbon coating process did not introduce spurious carbon nanotubes to the surface.

Figures 59 - 61 show examples of particles from various MOUDI stages for each MWCNT sheet sample. As shown in Figure 59, most of the particles from the [redacted] samples had rounded shape. We did not find any individual MWCNTS or agglomerates of MWCNTs in these samples.

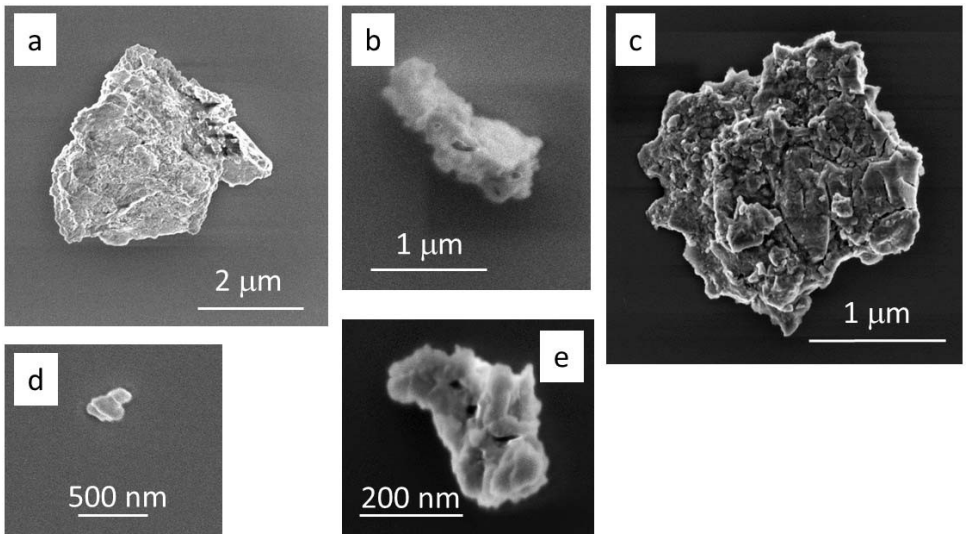

Figure 59: Examples of particles from the [redacted] MOUDI samples. (a, b & d) are particles found on the stage 8 sample and (c & e) are from the stage 9 sample.

Figure 60 shows several particles that were found on the [redacted] stage 5 sample. One of the more common types of particles observed were fractal-like particles for which small primary particles (20 nm to 50 nm) agglomerated to form a chain or sponge-like particle. Figure 60c shows an example of one of these particles. Also present, were large particles with numerous protruding nanofibers. Figures 60a and 60e are examples of this type of particle.
Figure 60d is a high magnification image of one of the protruding fibers. In this example, the fiber extending from the primary particle was over 10 μm long.

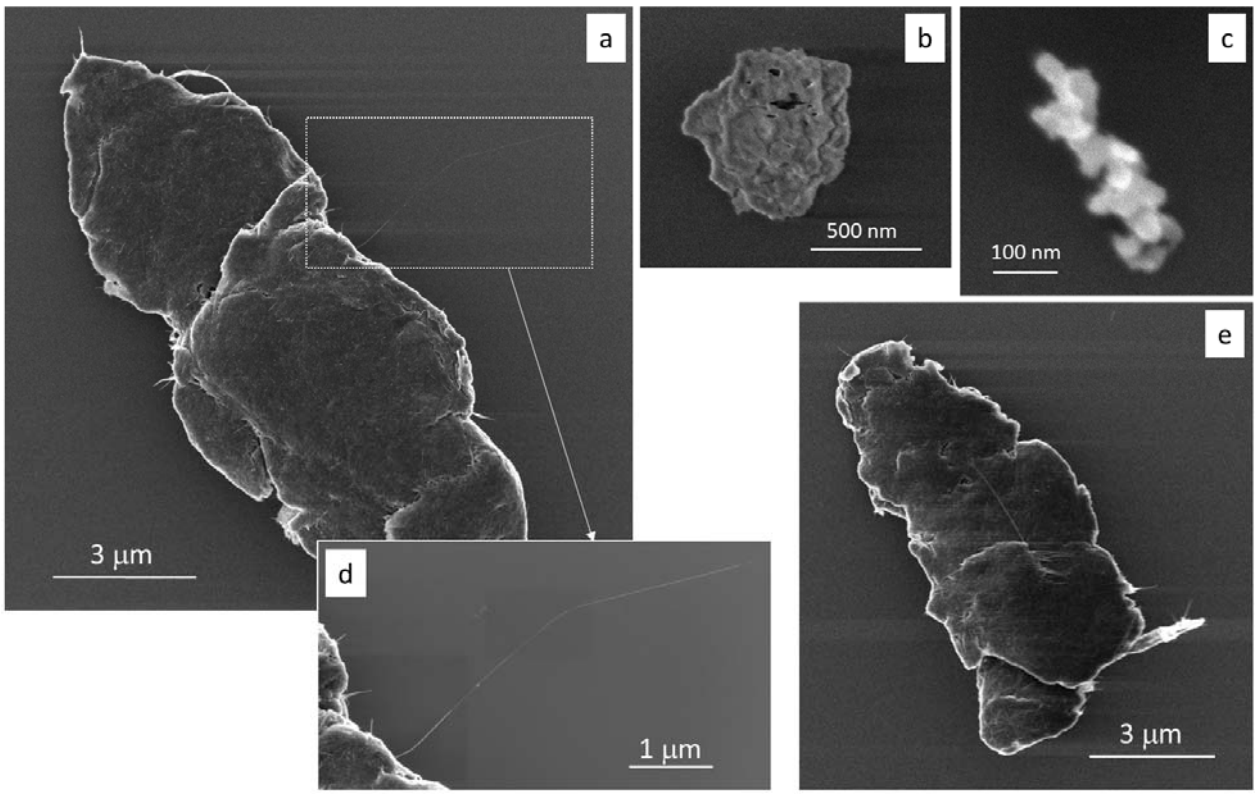

Figure 60: Example particles from the [redacted] stage 5 MOUDI sample.

Figure 61 shows several particles found on the [redacted] stage 6 sample. The particles found on the [redacted] samples were very similar to those found on the [redacted] samples. Again, one of the more common types of particle was the fractal-like particles in which small primary particles (20 nm to 50 nm) agglomerate to form a chain or sponge like particle [9]. Figures 61b & 61g show examples of these particles. There were also many nanorods that were similar to the one shown in Figure 61c. These rod-like particles are too thick to be MWCNTs but have been previously observed in nanocomposite abrasion particle samples. Also present, were large particles with numerous protruding nanofibers. Figures 61a, 61d, and 61e are examples of these particles.

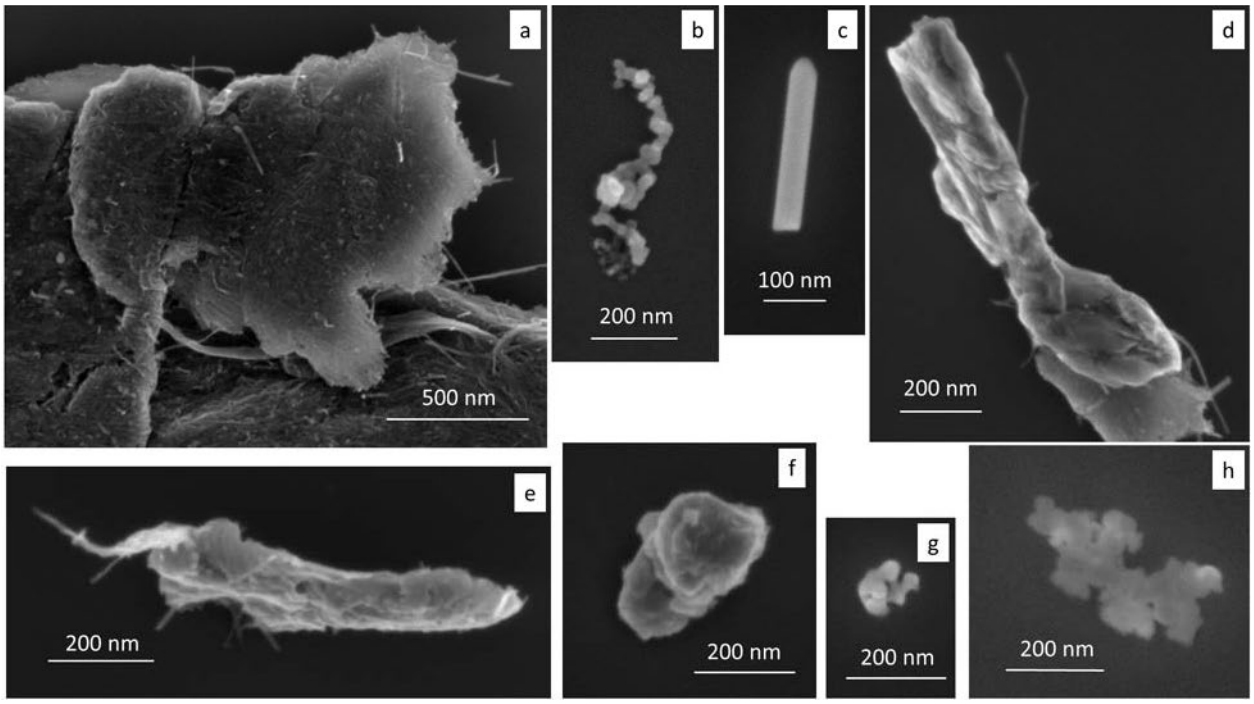

Figure 61: Example particles from the [redacted] stage 6 MOUDI sample.

Si wafers and TEM grids were placed near the abrader tip to collect release particles through passive sampling, as shown in Figure 42. Figure 62 shows some of the particles that were found on the passive sampled Si wafer after an [redacted] abrasion test. There were many agglomerates, fractal-like particles, and rod-like particles. Some of the rod-like particles were probably bare or thinly coated MWCNTs (Figures 62c, 62e, & 62g) while others could be pieces of polymeric coating used to bundle the MWCNTs together (Figures 62b and 62h). There were also areas of the specimen that had a locally high number of particles, or clusters of particles, meaning the distribution of particles on the specimen surface was not uniform.

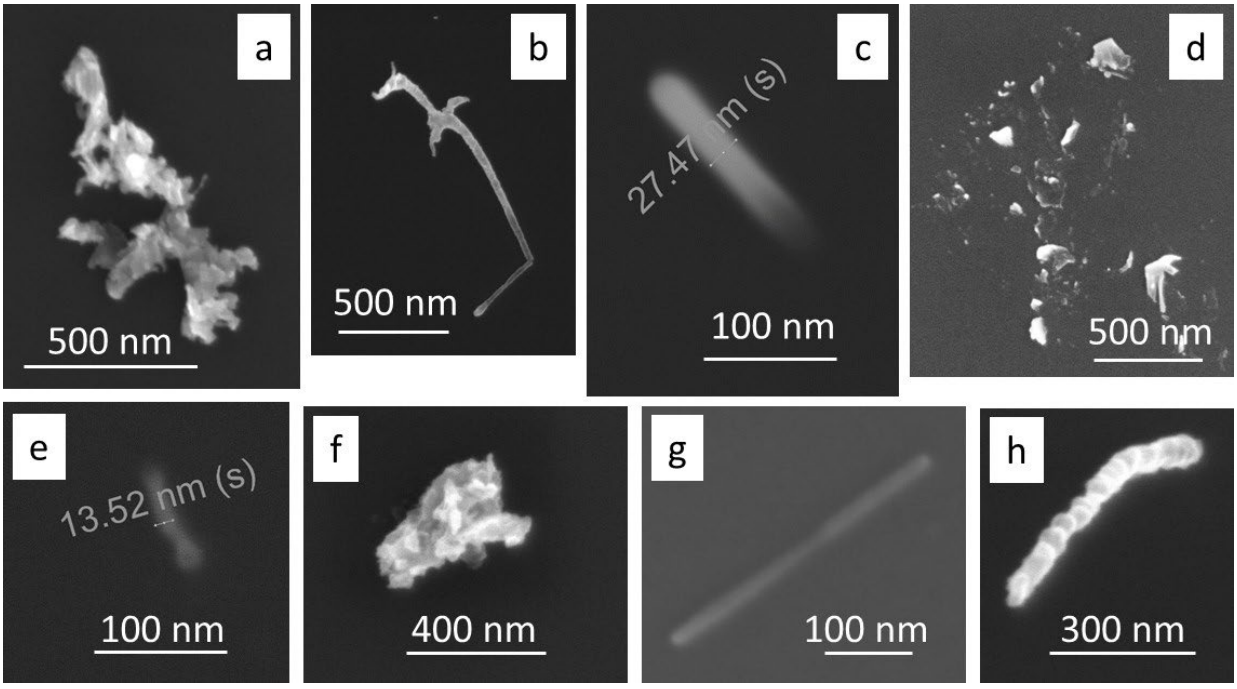

Figure 62: Example particles from passive sampling (Si wafer) during an [redacted] abrasion test.

The TEM grids from the passive sampling experiments were also analyzed using the SEM-STEM and TEM. STEM in SEM was used to quickly survey the grid for particle presence and to also identify the grid squares and particles that should be analyzed in detail using the TEM. Figure 63 shows a TEM grid and some of the particles that collected on the grid during an [redacted] abrasion test. Similar to the Si wafer samples, there were many fractal-like particles. However, many of these fractal-like agglomerates formed long chains (Figures 63b and 63h). Also observed were tube-like structures with uneven outer surfaces, as shown in Figures 63d and 63i.

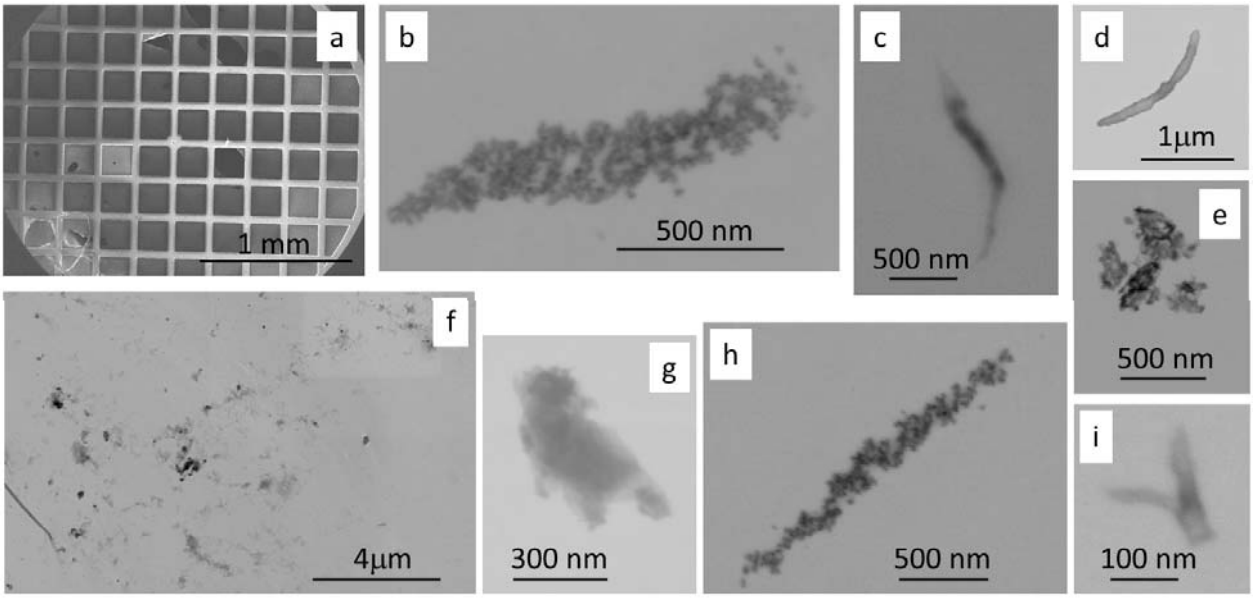

Figure 63: SEM-STEM images of the particles collected on a TEM grid during an [redacted] abrasion test.

TEM imaging of the fractal-like particles did not show any kind of ordered internal structure. The EDS analyses of these particles showed evidence for the presence of some Ca and S. Figure 64 shows the TEM images of a flake-like particle that was collected during an [redacted] abrasion test. The overall shape of the particle (Figure 64a) did not suggest the presence of any multi-walled structure. However, high magnification TEM images from sections of the outer flaky layers revealed layered MWCNT-like structures throughout the particle. In Figure 64b, the MWCNT-like structure appears to be covered with some kind of amorphous coating. Also, bundles of MWCNTs can be seen along the particle edge (Figure 64c).

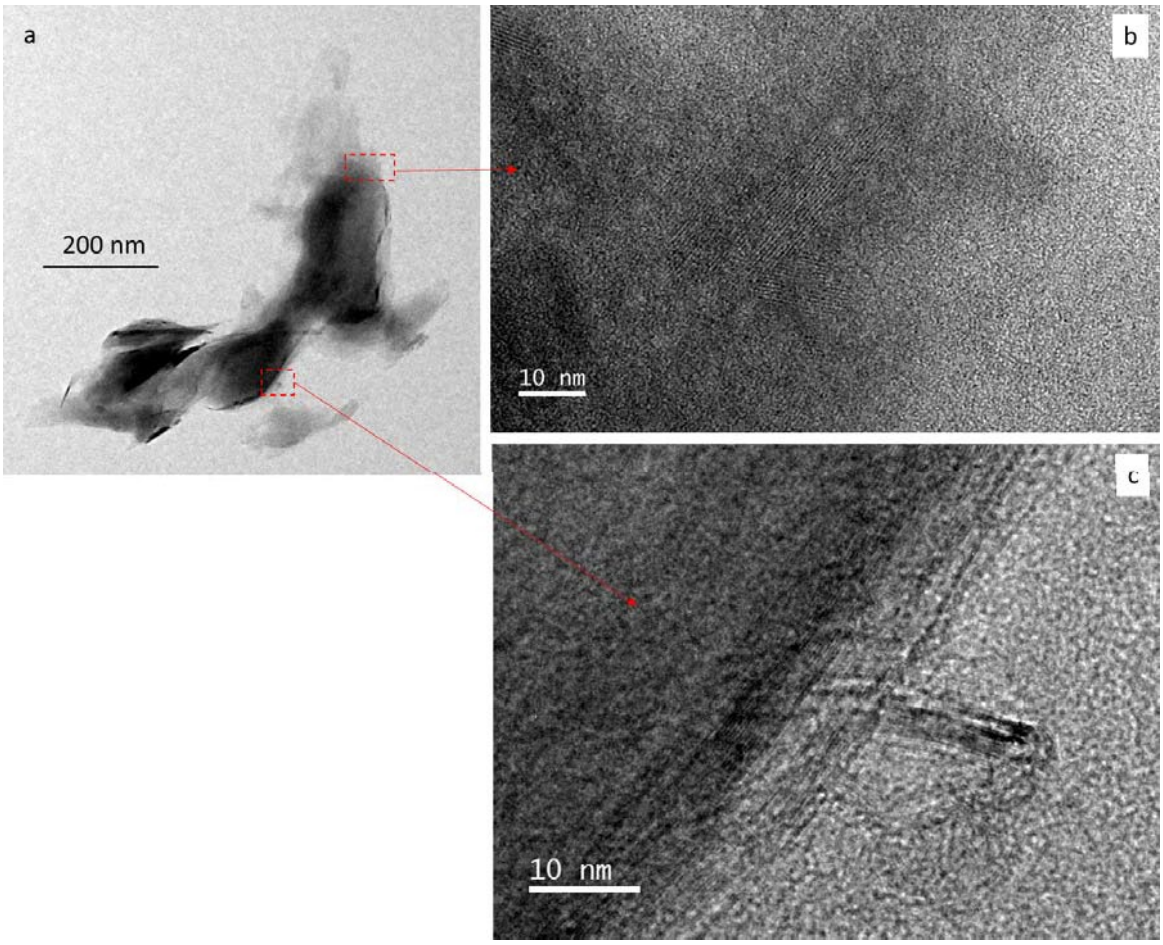

Figure 64: TEM images of a small flake-like abrasion particle that was passively collected on a TEM grid, during an [redacted] abrasion test.

6 DISCUSSIONS & CONCLUSIONS

Three commercially available, multi-walled carbon nanotube (MWCNT) containing ballistic inserts were used as test systems for developing analytical methods for detecting MWCNTs in consumer products. We were able to confirm the presence of MWCNTs in all three of the products that were examined. All three types of inserts had a similar construction, in which a stack of ballistic textile sheets, such as [redacted] and UHMWPE (including one or more MWCNT reinforced sheets), were encased in sealed water-resistant outer sleeve. However, the manufacturers employed two different strategies for incorporating MWCNTs into the ballistic insert materials. One company chose to use a MWCNT impregnated coating on the constituent woven [redacted] sheets. The other two insert products each contained a single matted sheet of coated MWCNT bundles.

In all three ballistic products, the initial confirmation of the presence of MWCNTs was made using Raman spectroscopy. The amount of sample preparation needed for determining the presence or absence of MWCNTs in bulk material was minimal and we were able to quickly determine which components of the ballistic panels contained MWCNTs. However, our prior work involving abrasion induced release of MWCNTs from epoxy nanocomposites indicated that the use of Raman spectroscopy for the detection of individual MWCNTs or nanoscale agglomerates of MWCNTs in the release debris is currently not practical and requires further development.

[redacted] and [redacted] both used a similar MWCNT matted sheet material in their inserts. SEM imaging on FIB generated cross sections of these material showed that each MWCNT sheet had a polymer film capping layer on the exterior surface that was nominally 1 μm in thickness. The interior of these MWCNT sheet materials were not fully dense and consisted of an entanglement of filaments. The filaments appeared to be polymer coated bundles of MWCNTs, as evidenced by the Raman spectroscopy and TEM analyses of the materials. Further, smaller filaments were often observed to split off from the larger filaments and branch out into the surrounding structure. The MWCNT sheets used by both companies contained iron rich nanoparticles, as indicated by S/TEM-EDS, which may have served as the catalyst material during the growth of the MWCNTs.

The [redacted] soft insert employed a MWCNT impregnated coating on the outer surfaces of the [redacted] sheets that were contained within the layered structure of their ballistic inserts, as evidenced by SEM imaging and Raman spectroscopy. Since the MWCNTs were embedded in a polymer matrix, the [redacted] MWCNT containing material was nearly fully dense, unlike the MWCNT sheet materials used by the other two manufacturers. S/TEM-EDS revealed that the [redacted] coating contained a variety of particle inclusions. The smallest nanoparticles identified were Ni-rich. The Ni-rich particles may have served as the catalyst material for the growth of the MWCNTs. However, there were also larger Zn-rich nanoparticles that seemed to be correlated with a potassium (K) signal.

Once we were able to confirm the presence and determine the location of the MWCNTs in each product, several use-case scenarios were evaluated for MWCNT release. Since the MWCNT containing materials were encased in a sealed water-resistant sleeve, the most likely release scenario was deemed to be that in which the outer sleeve is compromised accidentally (e.g., puncturing or tearing) or through misuse (e.g., cutting).

We subjected outer nylon sleeve from the [redacted] product to simulated friction induced wear tests (9000 cycles of rubbing under 800 g of load). The integrity of the material seemed to be unaffected by the rubbing test. Therefore, the rubbing test indicated that the outer nylon sleeve of the [redacted] product is unlikely to wear out during the normal use of the product (Note: The polyester sleeves were not subjected to the rubbing test at this time.
Additional testing would be required to determine if the polyester sleeves, when subjected to the rubbing test, will respond in a manner similar to the nylon.). However, if the outer sleeve of the ballistic panel is compromised accidentally (e.g., puncturing or tearing) or through misuse (e.g., cutting), containment of any nanoparticles cannot be expected. The situation in which the release of MWCNTs/nanoparticles is considered to be most likely is when the MWCNT sheets in the ballistic panel are subjected to direct mechanical stressing, such as abrasion.
Based on this premise, the direct mechanical abrasion testing of the MWCNT containing components of the armor inserts was considered to be the worst-case scenario for MWCNT and nanoparticle release. Therefore, wipe and abrasion tests were performed on the MWCNT containing layers of the ballistic panels, i.e. coated [redacted] layers from the [redacted] ballistic inserts and the matted MWCNT sheets from the [redacted] and the [redacted] ballistic panels. As was mentioned earlier in this report, the coated [redacted] sheet from the [redacted] sample and the MWCNT sheets from the [redacted] and the [redacted] samples will be referred to as MWCNT sheets.

A qualitative measure of the amount of material released (not necessarily MWCNTs) from a MWCNT sheet sample during a wipe test is the level of soiling observed on the wipe test cloth after a given number of wipe cycles. After 20 wipe cycles, there was almost no visible soiling on the wipe cloth from the [redacted] coating material. However, the wipe cloths from the [redacted] and the [redacted] tests were noticeably soiled after the same number of cycles. The SEM analyses of the wear particles that were collected wipe cloths demonstrated that the fibrous contaminants produced from the wipe cloth itself will present a serious analytical challenge for the [redacted] and the [redacted] samples. The fibrous nano- fragments generated from the test cloth were very similar in appearance to the wear particles generated from the MWCNT sheets.

In addition to the aforementioned difficulty in discerning the wear particles generated by the wipe cloth fabric from those generated by the MWCNT sheets, there were a number of other challenging factors associated with analyzing the wipe test wear particles that were collected on the SEM stub samples (i.e. carbon tabs). For example, many of the particles were either embedded in the adhesive compound or obscured by the wicking of the adhesive material over the particle. Also, the adhesive substrate deformed (softened) readily under the influence of the electron beam, making the high-resolution imaging of the nanoparticles challenging. The combined effects of the sample substrate induced imaging artifacts and the presence of the

contaminants from the wipe cloths made the detection and analysis of release particles using the SEM stub method impractical.

The Si wafer dust samples of the wipe particles posed fewer imaging challenges than the SEM stub samples, though suffered from the same contamination problem caused by the wear particles generated from the wipe cloth itself. As described in Section 5.3.1, automated large area MAPS scans were performed on the Si wafer dust samples and the images from these scans were subjected to an image processing routine to determine the size distribution of the particles found in each sample. Although it is difficult to compare particle size distribution data between the samples, the particle size distribution plots generated from the low-resolution images all followed a similar trend and indicated that most of the particles found in these wipe test samples were less than 700 nm in area equivalent diameter. On average, the particles found on the [redacted] sample were smaller than the particles from the [redacted] and the [redacted] samples. In all cases, less than 10% of the particles detected were greater than 1 μm in area equivalent diameter (data not shown). In the high-resolution scans, all three samples followed a common trend, i.e. the relative abundance of the particles increased as the size of the particles decreased. While the relative abundance of particles within a given size range is similar between samples, the [redacted] images had a significantly fewer number of particles than either the [redacted] or the [redacted] images. One explanation for this could be that the particle distribution over the Si wafer was not uniform and the [redacted] high resolution data set was collected over a sparsely populated region of the sample.

The particle size distributions recorded for all three MWCNT sheet materials were quite similar as determined by both the low resolution and the high-resolution images. Given the similar construction of the [redacted] and [redacted] products, we expected these two products to perform similarly under testing. However, there was a significant difference in the MWCNT incorporation methods used in the [redacted] product versus the [redacted] products. Since we had no reason to expect that all three MWCNT sheet materials would yield similar particle size distribution results, this may indicate that the test or sampling method is influencing the size distribution measured for the released wear particles. Further, for the size distributions that were determined from the high-resolution images, the sharp increase observed in the relative abundance of particles as the size of the particles decreases may indicate that the true distribution has been obscured by an overwhelming number of artifact counts in these bins from image processing.

The particle size distribution data from the abrasion tests did not behave as expected either. Although the different MOUDI stages were designed to capture specific size range of particles, the highest number of particles found on all six MOUDI stages (stages 5 through 10) were below 300 nm in area equivalent diameter. Based on our particle size distribution analysis results, we suspect that there are additional factors that are influencing the aerosol collection process and further examination is needed to better understand the MOUDI sampling process of MWCNT nanocomposite wear particles. We also found that the passive sampling method is an effective alternative for MOUDI sampling.

Although many different types of nanoscale particles were found in the [redacted] wipe test and abrasion test samples, none of them were isolated MWCNTs or agglomerates of MWCNTs. Based on our knowledge of the [redacted] coating material, we expect that some of the released nanoparticles contain MWCNTs, but we did not find any particles with exposed MWCNTs in these samples. On the other hand, we found many micrometer sized particles on the [redacted] and the [redacted] wear test particle samples that exhibited protruding MWCNT-like nanoscale fibers. We also found a number of individual MWCNTs and small agglomerates of MWCNTs along with the other release particles from the [redacted] and the [redacted] samples. However, most of these individual MWCNTs and the MWCNT agglomerates were identified through a manual hunt-and-peck search of the sample surface, rather than by the automated particle analysis routine that was applied to the image sets that were acquired by MAPS. Therefore, additional research is required to assess the usefulness of the automated imaging and particle analysis routines that were employed here for the detection and measurement of nanoparticles of interest. Some discussion of the known limitations of these automated methods will follow.

The image processing routine used for particle counting and particle size measurement can contribute to the errors and uncertainties in these measurements. The variations in the imaging conditions such as environmental conditions, instrument status, and local sample conditions resulted in slight variations in the overall image quality from one set of images to the next. This meant that the threshold value used to create the binary masks for particle identification had to be manually adjusted for each image data set. Such manual adjustments introduce inevitable subjectivity in the image processing routine. Additionally, each MAPS run was performed using a 10 % horizontal and vertical frame overlap. Therefore, approx. 20 % of each frame is imaged twice, and so the particles contained therein are counted twice during the particle analysis step, thereby contributing to a significant level of overestimation. Similarly, the duplicate counting of the particles on the image frame edges was another source of error. However, we were able to discount the contribution from this as negligible by comparing the total particle counts from particle analysis sessions with and without the edge exclusion option turned “on” in the analysis software. The use of image processing steps such as dilation can also affect the

resulting particle sizes. However, these operations were applied to all images in a consistent manner and should not impact the relative size distributions between the different samples.

Imaging artifacts can also limit the effectiveness of the automatic imaging routines. One challenge was in trying to optimize the image brightness and contrast levels for an automated imaging session. Note that the long nanofiber protruding from the primary particle in Figure 59d shows several different contrast levels. Closer to the primary particle, the fiber is bright and shows up clearly against the Si substrate. However, where the fiber is in contact with the Si substrate, the contrast is weaker, and the fiber is harder to detect. This variation in the contrast is due mainly to the enhanced secondary electron emission that is produced along a free edge of a specimen [10]. This effect also explains why it is relatively easy to find and image a MWCNT protruding from a larger parent particle while detecting the same MWCNT lying flat on a surface is difficult. Therefore, optimizing the automatic imaging conditions on a nanoparticle that exhibits strong contrast will make it difficult to image particles that exhibit weak contrast, and vice versa. The limited depth of focus that accompanies high magnification imaging is a challenge that can only be overcome by robust autofocusing routines or frequent manual intervention. Achieving the right balance between the effective signal to noise ratio and the incident beam conditions necessary to detect nanoscale surface features can be another source of imaging artifacts.

Carbon contamination of the specimen surface, under the influence of the incident electron beam (e.g. during SEM imaging), can also be a problem. In Figure 59d, there is a rectangular region of weak contrast surrounding the fiber. The area represents a thin carbon deposit that was generated by the electron beam as it was repeatedly scanned over the area to optimize the imaging conditions. This is a common SEM imaging artifact, especially when imaging carbonaceous materials. Although this kind of contamination does not impact most imaging applications, it can be detrimental to the imaging of a nano-scale features, such as a single MWCNT. The before-and-after images shown in Figure 65 illustrates this problem very clearly. Figure 65a contains an approx. 30 nm diameter nanofiber on a Si substrate. Figure 65b is shows the same nanofiber after it has been repeatedly scanned with the electron beam for a few seconds. The accumulated carbon contamination on the original nanofiber has obscured some of the finer features in the image and has significantly increased the apparent diameter of the fiber.

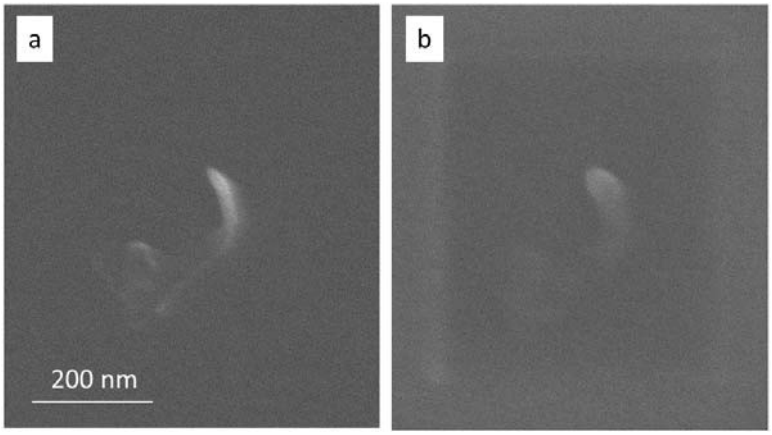

Figure 65: Before-and-after images of a nanofiber that has been repeatedly scanned by the electron beam. Carbon contamination can cause serious artifacts in the image.

We were able to confirm that all three types of ballistic products used in this study contained MWCNTs, as advertised. Under accidental or intentional misuse conditions, the MWCNT containing components of the ballistic products could be exposed to direct mechanical stressing thereby increasing the possibility for the release of MWCNTs or MWCNT containing particles.
No individual MWCNTs, or agglomerates with exposed MWCNTs, were found in the particles that were collected from the wipe test or abrasion test of the [redacted] MWCNT sheet. However, a number of individual MWCNTs and small agglomerates with protruding nanofibers (possibly MWCNTs) were found in the particles collected from the wipe tests and abrasion tests of the [redacted] and [redacted] MWCNT sheet. There were also many micro-scale particles with protruding nanofibers (some fibers were over 10 μm long) in the release materials from the [redacted] and the [redacted] MWCNT sheets. Qualitatively, the [redacted] MWCNT sheet produced fewer particles during the wipe tests and the abrasion tests.

Automated image acquisition and image processing routines were found to be very effective at collecting images, in a consistent manner, on large areas of the sample surface. The images from these surveyed regions were used to provide some guidance as to where the particles were locally concentrated on the sample surface. However, locating individual particles of interest required that the analyst perform a manual survey of the collected images to identify regions for subsequent analysis. A brute-force approach, such as this, is prohibitive in terms of both the instrument time and the personnel effort needed to review the data. The automated image acquisition and analysis routines used in this study therefore lack the ability to effectively analyze a sufficiently representative area of the sample at the resolution necessary to detect individual MWCNTs.

In summary, we found that the construction method of the MWCNT ballistic material has an impact on the rate of release of nanoscale wear particles. Fully embedded MWCNTs in a

flexible matrix, as seen in the [redacted] product, are less likely to be released as individual MWCNTs or as nanoscale agglomerates of MWCNTs, when compared to the network of coated MWCNT bundles that were used in the construction of the [redacted] and [redacted] products. Existing imaging technology can provide extremely high-resolution images that can detect and confirm the presence MWCNTs, but performing these analyses over a large sample area in a quantitative manner is still a challenge. We have made some progress in designing a robust wear particle sampling process and automated imaging pipeline. However, the current approach still requires significant manual intervention by the analyst, making the analysis of a statistically relevant amount data impractical. The improved sampling of aerosol wear particles, especially at the scale of 10 nm to 20 nm MWCNTs, will require a better controlled aerosol transport layout and different aerosol conditioning steps. Additional study will also be needed to gain better insight into how a given test/sampling method can impact the distribution of wear particles that are collected from the test. Also, a more complete understanding of the factors that influence the detection and measurement of nanoparticles in the automated image acquisition/analysis routines is necessary for the improvement of these routines and to ensure that accurate size distributions can be determined for the nanoparticles that are collected from the different wear tests.

ACKNOWLEDGEMENT

We would like to acknowledge Robert Fletcher, Julie Bitter and Matthew Staymates for their help with MOUDI stage modification, aerosol sampling setup, and IR spectroscopy measurements; Ryan Beams for Raman imaging; and Alline Myers for TEM imaging of the MWCNT nanocomposite textile samples.

ABBREVIATIONS & TERMS

AATCC: American Association of Textile Chemists and Colorists ATR-IR:

attenuated total reflectance - infrared

BF: bright field

CPC: condensation particle counter EBID:

electron beam induced deposition

EDS: energy dispersive x-ray spectrometry ETD:

Everhart-Thornley detector

FIB: focused ion beam

HAADF: high angle annular dark field

MOUDI: micro-orifice uniform deposit impactor

MWCNT: multi-walled carbon nanotube

SE: secondary electron

SEM: scanning electron microscope

S/TEM: scanning transmission electron microscope/transmission electron microscope TEM:

transmission electron microscope

TLD: through-the-lens detector

REFERENCES

1. The National Nanotechnology Initiative Report "Environmental, Health, and Safety Research Needs for Engineered Nanoscale Materials", September 2006.
2. http://www.nanowerk.com/spotlight/spotid=23118.php (last accessed on July 29, 2015)
3. Bokobza, L. & Zhang, J. (2012) "Raman spectroscopic characterization of multiwall carbon nanotubes and of composites" *eXPRESS Polymer Lett.* **6 (7)**, 601-608.
4. ASTM D4157-10 - Standard Test Method for Abrasion Resistance of Textile Fabrics (Oscillatory Cylinder Method)
5. Brockmann, J.E. (2001) "Sampling and Transport of Aerosols", in Baron, P.A. & Willeke, K. (Eds.), Aerosol Measurement: Principles, Techniques, and Applications (2nd Ed.) (143-195). Toronto, John Wiley and Sons.
6. Kuhlmey, G.A., Liu, B.Y.H., Marple, V.A. (1981) "A Micro-Orifice Impactor for Submicron Aerosol Size Classification", *Am. Ind. Hyg. Assoc. J.* **42**, 790-795.
7. Marple, V.A., Rubow, K.L., Ananth, G.P. & Fissan, H.J. (1986) "Micro-orifice Uniform Deposit Impactor" *J. Aerosol Sci.* **17**, 489-494.
8. Schindelin, J.; Arganda-Carreras, I. & Frise, E. et al. (2012), "Fiji: an open-source platform for biological-image analysis", *Nature methods* **9(7)**: 676-682.
9. Baron, P.A. & Willeke, K. (2001) "Aerosol Fundamentals", in Baron, P.A. & Willeke, K. (Eds.), Aerosol Measurement: Principles, Techniques, and Applications (2nd Ed.) (55-56). Toronto, John Wiley and Sons.
10. Goldstein, J., Newbury, D., Joy, D., Lyman, C., Echlin, P., Lifshin, E., Sawyer, L. & Michael, J. "Scanning Electron Microscopy and X-Ray Microanalysis", 3rd Ed. (2003) Springer, N.Y. p 199.

APPENDIX 1: [redacted]OUTH BALLISTIC BACKPACK

[redacted]

[redacted]

my account | contact us | blog | t

ABOUT US | SHOP | CART | CUSTOM SOLU

Home › Ballistic Backpacks and Backpack Inserts › Youth Ballistic Backpack

YOUTH BALLISTIC BACKPACK

$300

Scroll down to order...

Our ballistic backpack provides built-in ballistic protection in a backpack that weighs just ounces more than a non-armored backpack. [redacted]carbon nanotube armor is lined in the back panel of the backpack. Sewn into the rear of the pack, you can always be confident that the armor hasn't been accidentally left at home and that you or your child are protected in case of the unthinkable. The backpack can be quickly brought to the front as a shield or can serve as center of mass protection while fleeing the scene of the shooting.

- 600 denier polyester, 420 denier honeycomb polyester contrast
- Interior organizer panel
- Comfortable ergonomic padded straps and padded back
- Web top handle
- Water bottle holder
- Exterior pocket with hook and loop closure
- Convenient headphone exit port
- Dimensions: 17.25"h x 13.25"w x 5.5"d; Approx. 1,257 cubic inches

Previous styles of ballistic backpacks that were displayed online are no longer available. You can now choose from one of 3 colors or you may send us your backpack to retrofit with [redacted]rmor. The backpacks are available in Black/Red, Black/Blue, Black/Silver, Pink, and Purple colors, and Level II (.357 Magnum, .45, .40, 9 mm) or Level IIIA (.44 Magnum, .357 SIG and below) protection.

[redacted]

my account | contact us | blog | buy online | call [redacted]

ABOUT US | SHOP | CART | CUSTOM SOLUTIONS | FAQS | NEWS

[redacted] WITH CARBON NANOTUBES

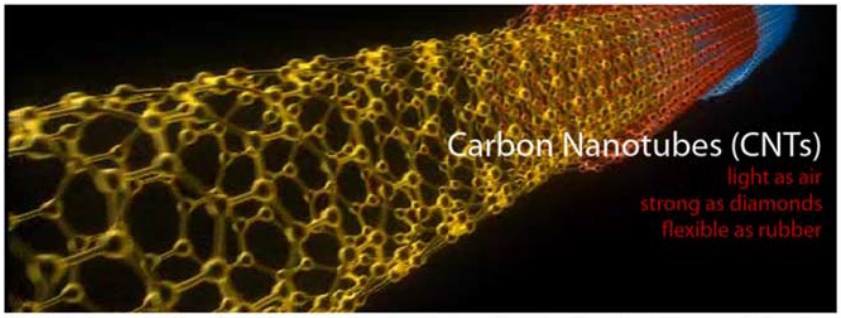

Since their discovery in the early 1990's scientists have been fascinated by Carbon Nanotubes. They are as light as air, stronger than diamonds and can be as flexible as rubber. This makes them perfect for enhancing the performance of body armor such as: vests, helmets, gloves and pants. Carbon nanotubes (CNTs) are five times less dense than steel and approximately 30 times stronger this makes them the ultimate mechanical filler for reinforcing polymers like aramid fibers such as Kevlar without adding extra weight.

The problem with using these tiny miracles of unimaginable strength has been the enormous cost to produce them, the fact they can only be made in relatively small quantities at a time, and are complicated, expensive, time-demanding processing techniques needed to properly integrate them into ballistic materials. The result is that NO other body armor companies offer CNT re-inforced armor. Instead they produce armor that weighs more, is much thicker, isn't as strong, or as light and flexible. Until now.

Once you've learned why CNTs are so important for your body armor, take a look at Amendment II's Carbon Nanotube products.

Purchase

Am[redacted]tists and engineers are extremely excited to be the first to discover, perfect and use a process of mass manufacturing of affordable CNT based armor. Until now, all existing methods of fabricating CNT-polymer composites involve quite complicated, expensive, time-demanding processing techniques such as solution casting, melting, molding, extrusion, and in situ polymerization. In all of these techniques, nanotubes must either be incorporated into a polymer solution, molten polymer or mixed with the initial monomer before the formation of the final product (e.g. yarn, ribbon or film). In addition, these methods cannot be applied in the case of insoluble or temperature sensitive polymers, which decompose without melting.

Ar[redacted]armor, Ry[redacted] world's first commercially available cost effective Carbon Nanotube armor and is much: lighter, stronger, more flexible, thinner and has less much less back-face deformation (how far the bullet pushes into you), which means it hurts less when shot.

What does all this mean to you? If you are ever going to buy body armor make sure it has been made using Carbon Nanotubes. Your life could depend on it.

Privacy Policy | Refund Policy

Switch to our mobile site

APPENDIX 2: [redacted] PANEL

[redacted]

Cart 0 items

HOME ABOUT US ACCESSORIES HARD PLATES SOFT PANELS CARRIERS BACKPACKS
WHOLESALE BULLETPROOF UNDERWEAR PROMOS

Soft Panels / Soft Panels 11X14 Carbon Nanotube Ballistic Backpack Soft Panel

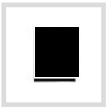

11X14 Carbon Nanotube Ballistic Backpack Soft Panel

$119.95

11X14 Carbon Nanotube Ballistic Backpack Soft Panel
Reference#: [redacted]

Specs

THREAT LEVEL: Level IIIA
WEIGHT/THICKNESS: 1.4 lbs; .25 inches
AVAILABLE SIZES: 11 inches x 14 inches
SHAPE/CURVE: Rectangle
COMPOSITE: Polyethelene, Kevlar, CNT, and EIP Foam
THREATS: .380, 40 S&W, .45 ACP, 357 Sig, 44 Magnum
Ships within 7 days.

Quantity: 1 BUY

Offer - Free Shipping

When You order more than $400

Tweet Share
Google+ Pinterest

Earn **11 loyalty points**.

give.it
Add to my wishlist

Details Reviews

11X14 Carbon Nanotube Ballistic Backpack Soft Panel
Reference #: [redacted]

Specs

THREAT LEVEL: Level IIIA
WEIGHT/THICKNESS: 1.4 lbs; .25 inches
AVAILABLE SIZES: 11 inches x 14 inches
SHAPE/CURVE: Rectangle
COMPOSITE: Polyethelene, Kevlar, CNT, and EIP Foam
THREATS: .380, 40 S&W, .45 ACP, 357 Sig, 44 Magnum
Ships within 7 days.

APPENDIX 3: [redacted] ARMOR

[redacted]

View larger image

[redacted] Carbon Nanotube Soft Armor IIIA - Backpack Armor

★★★★★ CODE: AR500-CNT-PAK

Price: $140.00

Out-of-stock

Production Lead Time: up to 2 weeks

☐ Notify me when this product is back in stock

Add to wish list

Description | Send to friend | Reviews | Regulations | Tags

[redacted]arbon Nanotube (CNT) IIIA 11" x 14" Backpack Soft Body Armor

[redacted]Carbon Nanotube Soft Body Armor is Ultra-Light, Ultra-Thin, and extremely Flexible. Carbon Nanotube Soft Body Armor is the pinnacle of soft armor technology. Utilizing the latest Carbon Nanotube technology and proprietary Non-Newtonian back-face foam, [redacted]CNT body armor is the most robust, light-weight, flexible, and affordable level IIIA soft body armor in the industry!

Measuring in at 11" x 14" our new Carbon Nanotube soft IIIA backpack armor is concealable to the point of virtually disappearing in backpacks, book bags, laptop cases, luggage, and plate carriers. Being flexible increases ergonomics and comfort as the armor forms to its surroundings, flexing and bending while providing IIIA threat protection anywhere you need.

Carbon Nanotubes have finally found their way into body armor applications [redacted] is proud to lead the way with this new technology. Carbon Nanotubes are tiny strands with incredible strength, described as being as harder than diamonds. The addition of Carbon Nanotubes increases effectiveness in multi-hit capabilities and allows creation of a lighter weight, thinner profile, more reliable, and robust armor solutions than body armor that use only [redacted]oft armor consisting of only [redacted]often costs more, weighs more, and requires more layers making them thicker, less flexible, and less ergonomic.

Back face deformation is also a concern with soft body armor as it directly translates to what you feel in the event of taking a round. Existing soft armor on the market uses high density foam to increase comfort and decrease back face deformation. Our CNT soft body armor uses a Non-Newtonian foam, a material that instantaneously hardens under pressure which improves performance by decreasing back face deformation and more efficiently spreads energy throughout a larger surface area of the body armor. This results in less energy transfer through the soft armor, and less back face deformation compared to traditional, thicker, high density foams.

Size: 11" x 14", Backpack Style Armor (designed for backpack insertion)

Weight: 1.0 lb.

Rating: Rated to level IIIA Threats. Pistol calibers such as 22LR, 9mm, .40 s&w, .45, 10mm, .357 magnum, *up to* .44 magnum and .357 sig

Maintenance: [redacted]arbon Nanotube body armor is sealed in a durable rip-stop nylon sleeve. Anti-Microbial properties protect against odor, fungi, and bacteria. Simply wipe with warm damp cloth to clean.

[redacted]ew Carbon Nanotube layers and Non-Newtonian back face are the absolute latest advancements in soft body armor technology. [redacted]***will always stay true to our philosophy of offering the most reliable, and affordable body armor in the industry.***

APPENDIX 4: IMPACTION STAGE PARAMETER

Nominal cut size and number of nozzles of MOUDI stage is given below.

Stage Number	Nominal Cut Size, μm	Number of Nozzles
inlet	15	1
1	10	3
2	5.6	10
3	3.2	10
4	1.8	20
5	1.0	40
6	0.56	80
7	0.32	900
8	0.18	900
9	0.10	2000
10	0.05	2000

APPENDIX 5: MWCNTS COLLECTED FROM BAT FRAGMENTS

Three different types of MWCNTs collected from a MWCNT enhanced baseball bat (from the final report for the NIST-CPSC Interagency Agreement #CPSC-I-12-0009 "Exposure Assessment of Carbon Nanotubes in Sports Equipment, Phase II")

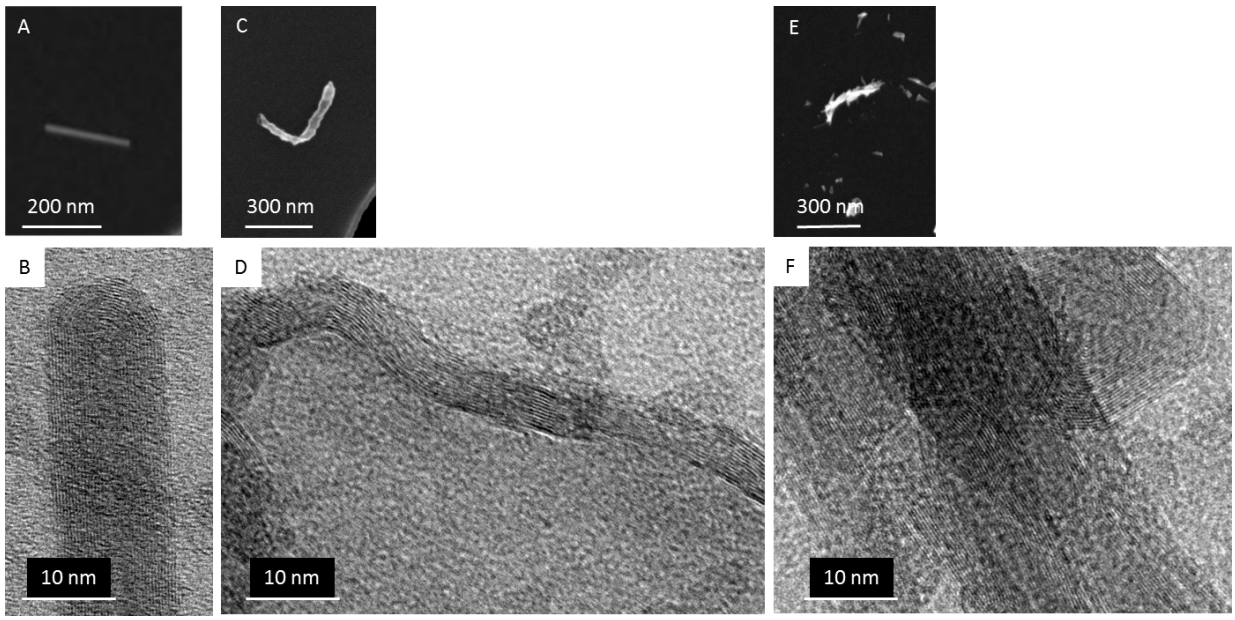

SEM images of three commonly occurring MWCNT particle types and corresponding TEM images showing the multiwalled structure of the particles.